Millimeter-Wave Radar for Low-Power Applications

Heunisch, Sebastian

2019

Document Version:
Publisher's PDF, also known as Version of record

Millimeter-Wave Radar for Low-Power Applications

Sebastian Heunisch

LUND UNIVERSITY

Doctoral Thesis
Electrical Engineering
Lund, September 2019

Academic thesis which, by due permission of the Faculty of Engineering at Lund University, will be publicly defended on Weekday, September 12, 2019, at 9^{15} a.m. in lecture hall E:1406, Department of Electrical and Information Technology, Ole Römers väg 3, 223 63 Lund, Sweden, for the degree of Doctor of Philosophy in Electrical Engineering. The academic thesis will be defended in English.

Faculty opponent is Prof. Edward Wasige, University of Glasgow, United Kingdom

Organization:
LUND UNIVERSITY
Department of Electrical and Information Technology
Ole Römers väg 3
223 63 Lund
Sweden

Document name:
DOCTORAL THESIS

Date of issue:
August 2019

Sponsoring organisation(s):
Swedish Foundation for Strategic Research (SSF)
Swedish Research Council (VR)
Knut and Alice Wallenberg Foundation

Author:
Sebastian Heunisch

Title and subtitle:
Millimeter-Wave Radar for Low-Power Applications

Abstract:
Radar technology has developed rapidly during the last century. Besides its initial use for military, it is nowadays also applied for many civil applications. Improvements in circuit technology make integrated radar sensors possible, allowing a significant reduction of the production cost. Integrated radio circuits in the low gigahertz range are widely available, not least driven by wireless communications. Even circuits at millimeter-wave frequencies are available, as they, for instance, are used for automotive radar. New semiconductor materials, devices, and circuit topologies offer interesting possibilities to increase the operation frequency and to reduce the power-consumption of radar circuits. With these developments, novel applications might open up, for instance the integration of radar in battery powered devices.

In this thesis, different aspects of developing low-power millimener-wave radar technology are investigated. An efficient, coherent radar pulse generator is implemented. The circuit is based on a resonant-tunneling diode implemented with III-V semiconductors. A fast metal-oxide-semiconductor field-effect transistor is used to shape short pulses. A novel modulation technique is presented, enabling the generation of a phase modulated radar waveform, without additional power loss. Various low-power radar applications of the circuit are investigated. The characterization of porcine-skin is demonstrated, which might open up biomedical applications. It is shown that the scattering of low-power pulses on different hand postures can be detected with a pulsed radar. A setup for the real time acquisition of hand gestures with a pulsed radar is implemented and the successful classification of 12 hand gestures is demonstrated. Using this technique low-power systems with low duty cycle waveforms might be implemented.

Keywords:
Gesture Recognition, Material Characterization, Radar, Reflectrometry, Resonant-Tunnelling Diode, Wavelet Generator, Wideband Millimeter-Wave Circuits

Classification system and/or index terms (if any):

Language:
English

Supplementary bibliographical information (if any):

ISBN (digital):
978-91-7895-248-9

Key title and ISSN:
Series of licentiate and doctoral theses, 1654-790X; No. 123

ISBN (printed):
978-91-7895-247-2

Recipient's notes:

Number of pages:
156

Price:

Security classification:
Unclassified

Millimeter-Wave Radar for Low-Power Applications

Sebastian Heunisch

LUND UNIVERSITY

Doctoral Thesis
Electrical Engineering
Lund, August 2019

Sebastian Heunisch
Department of Electrical and Information Technology
Lund University
Ole Römers väg 3, 223 63 Lund, Sweden

Series of licentiate and doctoral theses
ISSN 1654-790X; No. 123
ISBN 978-91-7895-247-2 (printed)
ISBN 978-91-7895-248-9 (digital)

Typeset in Palatino and Helvetica using LaTeX 2_ε.
Printed by Tryckeriet i E-huset, Lund University, Lund, Sweden.

Abstract

Radar technology has developed rapidly during the last century. Besides its initial use for military, it is nowadays also applied for many civil applications. Improvements in circuit technology make integrated radar sensors possible, allowing a significant reduction of the production cost. Integrated radio circuits in the low gigahertz range are widely available, not least driven by wireless communications. Even circuits at millimeter-wave (mm-wave) frequencies are available, as they, for instance, are used for automotive radar. New semiconductor materials, devices, and circuit topologies offer interesting possibilities to increase the operation frequency and to reduce the power-consumption of radar circuits. With these developments, novel applications might open up, for instance the integration of radar in battery powered devices.

In this thesis, different aspects of developing low-power mm-wave radar technology are investigated. An efficient, coherent radar pulse generator is implemented. The circuit is based on a resonant-tunneling diode (RTD) implemented with III-V semiconductors. A fast metal-oxide-semiconductor field-effect transistor (MOSFET) is used to shape short pulses. A novel modulation technique is presented, enabling the generation of a phase modulated radar waveform, without additional power loss. Various low-power radar applications of the circuit are investigated. The characterization of porcine-skin is demonstrated, which might open up biomedical applications. It is shown that the scattering of low-power pulses on different hand postures can be detected with a pulsed radar. A setup for the real time acquisition of hand gestures with a pulsed radar is implemented and the successful classification of 12 hand gestures is demonstrated. Using this technique low-power systems with low duty cycle waveforms might be implemented.

Popular Science Summary

The World with Radar Eyes

As humans, we are equipped with a set of different senses. We have ears to hear acoustic sounds, a nose to smell traces of chemical substances, and the tactile sense in our skin. With our eyes, we can even see our environment in different colors, since our Earth's surface is lit bright by the light of the Sun. What our eyes see as colors is in fact electromagnetic waves of certain frequencies. These electromagnetic waves also exist at frequencies we can't see. Radio waves, which are used for TV broadcast or mobile phones, are one example. Between the radio spectrum and visible light is a range of frequencies that not used that often today. A part of this frequency range is called the millimeter-wave spectrum. We can build instruments that use radio or millimeter waves to "see", similar as our eyes use light to see. This technique is called radar. Since it is quite dark in the millimeter wave spectrum, we need to generate the radio waves artificially to light the objects we want to examine. With radar, we get a new sense of the world with radio waves. Some objects we usually can't see through, might be transparent. Other objects which are hard to see might reflect radar "light".

In my work, I investigated a radar using millimeter-waves. I was working on methods to make the radar so efficient that it can be operated on battery, for example, in a mobile phone. I also investigated how skin "looks" like under radar "light". Since cancer has a different radar "color" than healthy skin, we might be able to diagnose skin cancer with radar in the future. I also looked at hand movements with radar. Compared to a simple camera, a radar can also measure how fast an object is moving and how far away it is. This can be used to recognize hand movements. Imagine you could control your mobile phone without touching it or even removing it from your pocket. Many new applications might be possible. What would you like to see with radar eyes? Maybe in a few years, you will have a sixth sense in your pocket.

Acknowledgments

All the efforts for this thesis would not have been possible without the people around me. First of all, I would like to express my gratitude to Lars-Erik, my PhD supervisor. You taught me that research is not always a straight path. There are many interesting things to explore and I think we found a few along the way.

My thanks also go to my co-supervisor Lars. You introduced me to the project and taught me the device fabrication in the lab. Your door was always open for discussions and your knowledge helped in many occasions.

It has been a pleasure being part of the nanoelectronics group. I learned a lot about transistor physics from Erik and about epitaxial crystal growth from Johannes and Mattias. I would like to thank my colleagues for their enjoyable company. We spent countless hours in the office together and became good friends. Thank you Olli-Pekka, for the distraction from work during the coffee breaks, Cezar for the philosophical discussions during lunch, and Elvedin for your help with cleaning my samples. To the remaining co-workers Fredrik, Markus, Lasse, Abinaya, Adam, Stefan, Karl-Magnus, Hera, Navia, Gautam, Sakeed, Robin, Patrik, Anil, Jong-Jong, Guntrade, Jun, Sophia, Martin, Kristofer and Aein. The group has been growing rapidly in the last years and writing all the memories would go beyond the scope of this text. It has been a pleasure to work with you.

Special thanks goes to my girlfriend Monica. I am lucky to have you in my life. Thank you for all your love and care, even in the most stressful moments.

Sebastian Heunisch
Lund, August 2019

Contents

Abbreviations

AFM atomic force microscope
ALD atomic layer deposition
Au gold

BCB benzocyclobutene

CNN convolutional neural network
CPW coplanar waveguide
CW continuous wave

DBH double barrier heterostructure

EBL electron beam lithography

FDTD finite difference time domain
FMCW frequency modulated continuous wave
FMiCW frequency modulated interrupted continuous wave
FWHM full width half maximum

GSG ground-signal-ground

HBT hetero-junction bipolar transistor
HEMT high electron-mobility transistor
HSQ hydrogen silsesquioxane

I in-phase
IF intermediate frequency

LDPE low-density polyethylene

LNA low noise amplifier
LO local oscillator

MBE molecular beam epitaxy
MIM metal-insulator-metal
MIMO multiple-input multiple-output
mm-wave millimeter-wave
MMIC monolithic microwave integrated circuit
MOCVD metal-organic vapour-phase epitaxy
MOSFET metal-oxide-semiconductor field-effect transistor
MRI magnetic resonance imaging
MUT material under test

NDC negative differential conductance
NDR negative differential resistance
NRZ non-return-to-zero

OOK on-off keying

PA power amplifier
Pd palladium
PLL phase-locked loop
PMMA poly(methyl methacrylate)
PRI pulse repetition interval
PSD power spectral density
PSL peak side lobe level

Q quadrature-phase

RCS radar cross section
RF radio frequency
RMS root mean square
RTD resonant-tunneling diode

SAR synthetic aperture radar
SEM scanning electron microscope
SNR signal-to-noise ratio

Ti titanium
TLM transmission line method
TMAH tetra-methyl ammonium hydroxide
UWB ultra-wideband

VNA vector network analyzer

WLAN wireless local area networking

Preface

In this thesis, I will summarize my five years of research with the Department of Electrical and Information Technology at Lund University. The aim is to give my perspective over the development of mm-wave radar, based on my research. The thesis covers several topics, including the fabrication of pulse generator circuits, radar waveform design, and radar measurements. The radar circuit can be used for material characterization, biomedical measurements and gesture recognition, which I demonstrated in my experiments. The scope of all those topics is aimed towards low-power radar. The thesis is divided in two parts. In the first part, I will give a more general overview over the research providing some background for the different topics and summarizing the main results. The second part contains a reproduction of the research articles that were published in the course of this thesis.

INCLUDED PAPERS

The following papers are included in this thesis. The respective published or draft versions are appended at the back of this thesis.

Paper I: Sebastian Heunisch, Lars Ohlsson Fhager, and Lars-Erik Wernersson, "A Phase-Correlated Duo-Binary Waveform Generation Technique for Millimeter-Wave Radar Pulses" *International Journal of Circuit Theory and Applications*, submitted: May 2019.

▶ *I am main author and contributor to this paper. I developed the waveform generation technique, and performed the simulations and measurements.*

Paper II: Sebastian Heunisch, Lars Ohlsson, and Lars-Erik Wernersson, "Clutter Analysis in a Time-Domain Millimeter-Wave Reflectometry Setup" *12th European Conference on Antennas and Propagation (EuCAP)*, London, 2018, pp. 1-4.

► *I am main author and contributor to this paper. I developed and programmed the measurement setup and analyzed the data.*

Paper III: Sebastian Heunisch, Lars Ohlsson, and Lars-Erik Wernersson, "Reflection of Coherent Millimeter-Wave Wavelets on Dispersive Materials: A Study on Porcine Skin" *IEEE Transactions on Microwave Theory and Techniques*, vol. 66, no. 4, pp. 0018-9480, 2018.

► *I am main author and contributor to this paper. I developed the measurement setup, performed the measurements and analyzed the data.*

Paper IV: Sebastian Heunisch, Lars Ohlsson, and Lars-Erik Wernersson, "Pulse-Distortion Analysis for Millimeter-Wave Time-Domain Material Identification" *48th European Microwave Conference (EuMC)*, Madrid, 2018, pp. 572-575.

► *I am main author and contributor to this paper. I performed the measurements, developed the simulations and analyzed the data.*

Paper V: Sebastian Heunisch, Lars Ohlsson Fhager, and Lars-Erik Wernersson, "Millimeter-Wave Pulse Radar Scattering Measurements on the Human Hand" *IEEE Antennas and Wireless Propagation Letters*, vol. 18, no. 7, pp. 1377-1380, 2019.

► *I am main author and contributor to this paper. I developed the measurement setup, performed the measurements and analyzed the data.*

Paper VI: Lars Ohlsson Fhager, Sebastian Heunisch, Anton Evertsson, Hannes Dahlberg, and Lars-Erik Wernersson, "Pulsed Millimeter Wave Radar for Hand Gesture Sensing and Classification" *IEEE Sensors Letters*, submitted: July 2019

► *I developed the measurement setup, and co-supervised the master students recording the gesture data-set and analyzing the data. I also helped during the writing progress.*

FUNDING ORGANISATIONS

This work was supported in part by the Swedish Foundation for Strategic Research (SSF), in part by the Swedish Research Council (VR), and in part by the Knut and Alice Wallenberg Foundation.

RESEARCH OVERVIEW

1

Motivation

The term radar (originally an acronym: radio detection and ranging) describes a technique to measure distance, angle, and speed of a remote target by the scattering of electromagnetic waves. Radar has developed very rapidly in the last century, not least driven by military technology. After the second world war, many strategical important applications like radar remote sensing and meteorological radar developed, which nowadays also find widespread use for civil purposes. While for radar applications in military and defense, high output power in the range of tens to hundreds of kilowatts is common, many modern radar systems operate at much lower power levels. Commonly, integrated radar systems are used. For monolithic microwave integrated circuits (MMICs) the required chip area decreases with frequency. At the same time, it gets increasingly difficult to design high performance circuits when moving closer to the maximum oscillation frequency, $f_{\max}$, of the technology used. Implementation of radar systems in technologies with a high $f_{\max}$, like III-V semiconductors or SiGe is, therefore, beneficial. With the further development of semiconductor technology, for instance with the integration of III-V semiconductors on silicon, higher operation frequencies and a further cost reduction of mm-wave MMICs can be expected. High performance semiconductor technology in combination with novel circuit topologies will enable radar sensors with ultra-low power consumption. Sensors can be battery powered, which makes radar available for completely new applications. One prominent example of this is Google's project Soli [1]. Radar based gesture recognition could be used as human machine interface to a smart-phone or wearable devices. Other applications might be sensors for material characterization and identification or mm-wave imaging, for instance in medical applications.

This thesis will investigate various aspects of the development of radar systems for novel applications. The goal is to develop technology for low power radar that can be integrated in battery powered devices. Chapter 2 will give an overview of the basic principles of radar and electromagnetic wave propagation. In Chapter 3 the implementation of an efficient mm-wave transmitter circuit will be discussed. Chapter 4 will describe radar waveforms that can be generated with the transmitter circuit. Chapter 5 will give a summary of measurement configurations that can be used to perform radar experiments with the circuit in the laboratory. One interesting application of the circuit might be medical measurements. An overview of the properties of biological tissues in relation with the interaction with mm-wave radiation will be given in Chapter 6. In Chapter 7 radar based hand gesture recognition will be discussed. Lastly, Chapter 8 sums up the main points of the thesis and give an outlook on subjects to future research.

2

Basic Principles

This chapter gives an introduction to the underlying principles that are important for the understanding of radar. The first part will describe the working principle of a radar system and basic radar measurements. The second part will cover the fundamentals of electromagnetic wave propagation and the interaction with materials more broadly. The focus will be on the phenomenology instead of strict mathematical derivations, which are extensively covered by literature.

2.1 THE RADAR PRINCIPLE

Radar is based on the scattering of an electromagnetic signal on a remote target [2]. The basic principle of radar operation is shown in Fig. 2.1 (a). A radar signal is transmitted and its echo, scattered on a target at distance, R, is recorded. For the implementation of a radar system, it is important that enough power from scattering on the target reaches the receiver. In free space, the power flux density, Φ, of the transmitted electromagnetic signal is given as

$$\Phi = \frac{P_\mathrm{t}}{4\pi R^2}, \tag{2.1}$$

where P_t is the transmitted power of the signal. Commonly, directive antennas are used to focus the transmitted power in a certain direction. Compared to emitting the power isotropically, the antenna has a certain gain, G_t. The target is usually characterized by the radar cross section (RCS), σ, describing an effective area for which the target interacts with the radar signal. The RCS is typically dependent on the direction of incidence and relates the scattered power to isotropic scattering on the target [3]. A fraction of the scattered power is finally captured by a receiving antenna with an effective aperture,

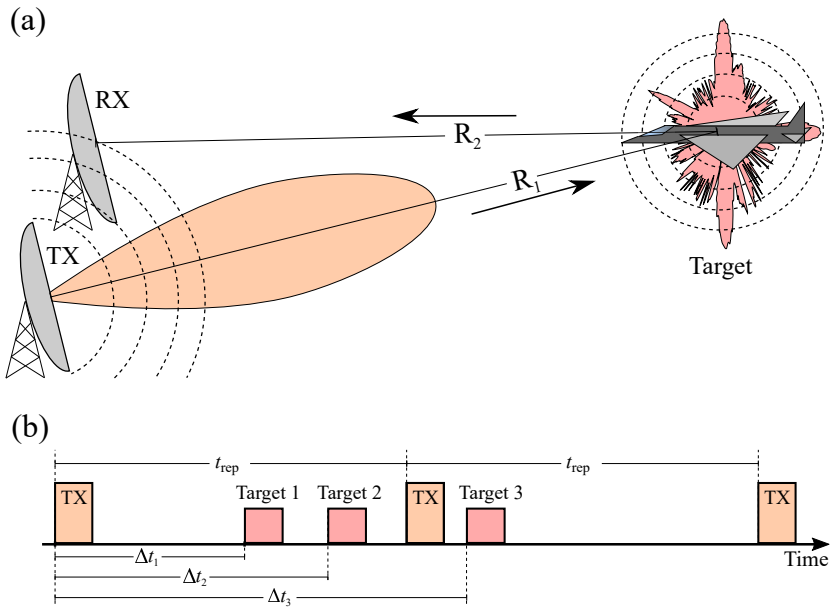

Figure 2.1: (a) Basic schematic of a radar system. A radar signal is transmitted by an antenna (TX). Energy is focused to a certain angle. Compared to isotropic radiation, a gain is achieved. The radar signal is scattered on a target, for instance, an airplane. Scattering on the target has some preferred directions, dependent on the geometry and material composition of the target. The scattered wave is recorded by a receiving antenna (RX). (b) Schematic of a radar distance measurement. The backscattered signal is received after a delay, Δt, dependent on the distance of the target. The radar signal is repeated with a fixed repetition interval, t_{Rep}. If a target has a larger delay than the repetition interval, the distance cannot be determined unambiguously (cf. Target 3).

A_e. A_e is related to the antenna gain by: $G_\mathrm{r} = \frac{4\pi A_\mathrm{e}}{\lambda^2}$. The power relation of a radar system, also known as radar equation, is given by

$$P_\mathrm{r} = \frac{P_\mathrm{t} G_\mathrm{t} G_\mathrm{r} \lambda^2 \sigma}{(4\pi)^3 R_1^2 R_2^2}. \tag{2.2}$$

It expresses the received power, P_r, in relation with the transmitted power, P_t [2]. In radar systems, the transmitter and the receiver often share the same antenna. These radar systems are referred to as mono-static. The distances, R_1 and R_2, are equal in this case and (2.2) simplifies accordingly. For the case that transmitter and receiver use different antennas, the system is called bi-static.

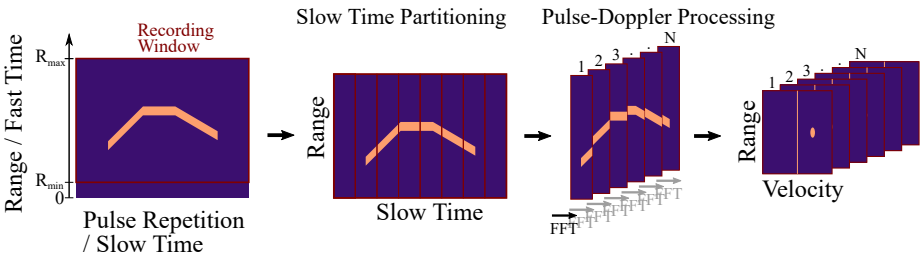

Figure 2.2: Schematic of pulse-Doppler radar signal processing. The data is organized in a fast time direction, corresponding to the samples of the reflected radar waveform, and a slow time direction, corresponding to the pulse repetitions. Taking a Fourier transform over several values in slow time direction of the remaining data allows to calculate the Doppler speed of the reflection.

The signal received by a radar is used to obtain information about possible targets in the beam path. The distance to a target can be obtained by measuring the time delay, Δt, at which an echo occurs with respect to the transmitted pulse. Electromagnetic waves in free space propagate with the speed of light, c_0. Therefore, the distance to the target can be calculated by

$$R = \frac{\Delta t \cdot c_0}{2}. \tag{2.3}$$

The factor of 2 is caused by the fact that the signal has to travel the distance to the target twice. That is, from the transmitter to the target and back to the receiving antenna. Typically, the signal is transmitted periodically, i.e., the signal is repeated after a repetition interval, t_{rep}. If the scattering from a target occurs at larger delays than t_{rep}, the distance to the target cannot be determined unambiguously. This principle is shown in Fig. 2.1 (b).

For moving targets, the scattering is affected by the Doppler effect. For pulsed systems, the Doppler effect can be explained very intuitively [4]. For a stationary target, pulses will arrive with the same rate as the pulses are transmitted ($1/t_{\text{rep}}$), but delayed. However, if the target is moving with the constant radial velocity, v_r, towards the transmitter pulses will arrive with higher rate. The relation of the time coordinate at the target, t_{target}, and the time coordinate at the source, t_{source}, can be expressed by

$$\Delta t_{target} = \Delta t_{Source} \left(1 + \frac{v_r}{c_0}\right). \tag{2.4}$$

Analogously, the carrier frequency of the pulses will also be compressed by

the same scaling factor

$$f_{target} = \frac{f_{source}}{(1 - \frac{v_r}{c_0})}. \tag{2.5}$$

To calculate the Doppler signal for pulsed radar, the data is commonly organized in matrix form as shown in Fig. 2.2 [2]. This technique is known as Pulse-Doppler processing. Each column of the matrix contains the samples of one pulse repetition interval (PRI). This time scale is commonly referred to as "fast time". The rows, on the other hand, correspond to signals that are sampled with the repetition rate, t_{rep}. This time scale is referred to accordingly as "slow time". Calculating a Fourier transform over the values in a row allows to determine the Doppler frequency of targets at this range. The PRI hereby determines the maximum Doppler speed that can be resolved unambiguously. The number of values for the Fourier transform determines the frequency resolution with which the Doppler speeds can be resolved. Therefore, a suitable processing interval needs to be selected. In this processing interval, the average velocity of a target is calculated, but the time resolution within this interval is lost. This is called the uncertainty relation of the short time Fourier transform [5]. Range and speed resolution need to be traded-off.

In the early days of radar, two basic waveforms were common: continuous wave (CW) and pulsed radar. In a CW radar, a narrow-band signal is transmitted. Systems that are sensitive to small Doppler shifts can be designed. However, resolving targets in range is not possible with CW radar. For the pulsed radar on the other hand, high range resolutions can be achieved by transmitting short pulses. However, the transmitted energy is decreasing with smaller pulse length. Pulses can, therefore, not be scaled arbitrarily short, without reducing the signal-to-noise ratio (SNR) for detecting a target. To be able to resolve Doppler shifts with pulsed radar, the signal needs to be coherent, i.e., the phase of the pulses needs to be well defined. This usually requires more complex transmitter systems to control the phase of the transmitted pulses. In modern radar systems the waveform is usually modulated in amplitude, phase or frequency to increase the bandwidth of the transmitted waveform [6]. In this case, the maximum achievable resolution, ΔR, is typically defined by the bandwidth, B, of the waveform by:

$$\Delta R = \frac{c_0}{2B}. \tag{2.6}$$

Frequency modulated continuous wave (FMCW) waveforms are widely used in modern radar systems. The classification to pulsed and CW systems is not as strict for modern radar waveforms. FMCW radar for instance, is often operated in a pulsed mode to avoid the direct wave signal from the transmitter to the receiver. This principle is known as frequency modulated interrupted continuous wave (FMiCW) radar [7].

For the detection of a radar signal, $s(t)$, in a real radar system, it is important to be able to differentiate the signal from the system noise. For this purpose matched filtering is used. The matched filter is designed to maximize the SNR in the receiver. If the system noise is white, i.e., the noise has a constant power spectral density (PSD) for all frequencies, the impulse response, $h(t)$, of the matched filter is given by the complex conjugate time inverse of the transmitted signal, $x^*(-t)$. The matched filter response, $y(\tau)$, is given by the convolution of the received signal with the impulse response by:

$$y(\tau) = \int s(t)h(\tau - t)\mathrm{d}t = \int s(t)x^*(t - \tau)\mathrm{d}t. \tag{2.7}$$

This is equivalent of calculating the cross-correlation of the received signal with the signal that has been transmitted. Ideally, the received signal is only a time shifted version of the transmitted signal, $s(t) = x(t - \Delta t)$. To evaluate radar waveforms, the delay, Δt, is often omitted and $s(t)$ is substituted by $x(t)$ directly. The width of the matched filter response gives the range resolution of a radar waveform. Radar waveforms are typically designed to have a narrow matched filter response with low side-lobes, i.e., small values at non-zero delays [6].

2.2 FUNDAMENTALS OF ELECTROMAGNETIC WAVES

Radar typically detects the backscattering of a transmitted electromagnetic wave of objects far away from the transmitter. Phenomenologically, radar signals can be described as electromagnetic waves. A derivation for electromagnetic wave propagation from Maxwell's equations can be found, for instance, in [8]. In this section, some important results will be summarized.

The coupling of electric and magnetic field, described by Maxwell's equations, allows the propagation as electromagnetic waves. Since targets are typically at a distance, the far field approximation is justified for most scenarios. In the far field, waves propagate as plane waves, which means that the electric and magnetic fields are perpendicular to the direction of propagation and no fields in propagation direction exist. The electrical field can then be expressed as:

$$E(z, t) = E_0 \exp(j2\pi ft - jkz)), \tag{2.8}$$

where f is the oscillation frequency of the wave and k is the wave number in direction of propagation. In time domain, plane wave propagation corresponds to a time delay of the original field, E_0. The magnetic field is coupled to the E field through Maxwell's equations. For plane waves the magnetic

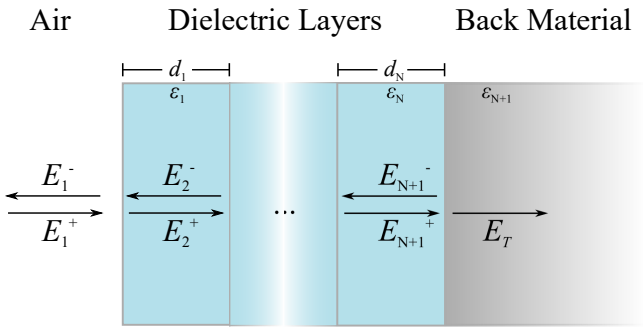

Figure 2.3: Schematic of a dielectric structure with multiple layers. At each interface, part of the electric field is transmitted while the other part is reflected. Between the interfaces, the wave propagates with the materials phase velocity. This leads to a delay of the reflection from each interface.

field is given by:

$$H(z,t) = \frac{1}{Z}\hat{\mathbf{z}} \times E_0 \exp(j2\pi ft - jkz)), \tag{2.9}$$

where Z is the wave impedance in free space. The cross product with the unit vector, $\hat{\mathbf{z}}$, causes H to be perpendicular to the E field and also perpendicular to the direction of propagation. The wavenumber is given by

$$k = \frac{2\pi f}{v_p} = 2\pi f\sqrt{\epsilon\mu}, \tag{2.10}$$

where v_p corresponds to the phase velocity in the medium. In free space the phase velocity is equal to the speed of light. The wave impedance is given by

$$Z = \sqrt{\frac{\epsilon}{\mu}}. \tag{2.11}$$

For absorbing materials, propagating waves are decaying exponentially. This effect can be taken into account by letting the permittivity take complex values. As a consequence, k and Z take complex values as well. The propagation of plane waves in a medium is, therefore, fully determined by the materials dielectric permittivity, ϵ, and magnetic permeability, μ. For radiation in the millimeter-wave (mm-wave) range, most materials are not magnetic. Their permeability usually corresponds to the vacuum permeability, μ_0.

At the transition from a medium with dielectric permittivity, ϵ_1, to a medium with the permittivity, ϵ_2, part of the wave is reflected, while the other part is transmitted. The fields can be expressed as a superposition of forward

propagating fields, E^+, and backward propagating fields, E^-. As boundary conditions at the interface, the electric and magnetic fields at the interface have to be continuous. This means $E^+ + E^- = E'^+ + E'^-$, where E' denotes the fields after the interface. From these boundary conditions, the reflection coefficient of the material interface can be derived. For normal incidence the reflection coefficient in dependence of the dielectric permittivity of the media is given by

$$r = \frac{E^-}{E^+} = \frac{\sqrt{\epsilon_2} - \sqrt{\epsilon_1}}{\sqrt{\epsilon_2} + \sqrt{\epsilon_1}}. \tag{2.12}$$

Similarly a term for the transmission, t, can be derived. The transmission is connected to the reflection by the relation: $t = 1 - r$.

For a multi-layered material, the fields are propagating between the interfaces and get reflected at all the interfaces. A schematic of a layered dielectric is shown in Fig. 2.3. The reflection coefficient at the multi-layer structure is given by the recursive relation:

$$\Gamma_i = \frac{E_i^-}{E_i^+} = \frac{r_i + \Gamma_{i+1} \exp(-2jk_i l_i)}{1 + r_i \Gamma_{i+1} \exp(-2jk_i l_i)}, \tag{2.13}$$

where r_i is the reflection coefficient at the interface according to (2.12).

For objects with a more complex geometry, the scattering often can't be solved analytically and numerical methods are used. Scattering is then usually expressed in the form of the RCS [3]. The RCS in relation to the incident and reflected field is defined as:

$$\sigma = \lim_{R \to \infty} 4\pi R^2 \frac{|E^-|^2}{|E^+|^2}. \tag{2.14}$$

3

Radar Pulse Generation

Efficient generation of millimeter-wave (mm-wave) signals is challenging. Passive structures can show high power loss due to mismatch, caused by fabrication uncertainties and increased material absorption at high frequencies. Additionally, the output power of active circuit elements is frequency limited. Therefore, a technology with high transition frequency, f_t, and high maximum oscillation frequency, f_{max}, is necessary. Commonly, III-V devices like hetero-junction bipolar transistors (HBTs) and high electron-mobility transistors (HEMTs) are used for high performance circuits, since technology with f_{max} close to terahertz frequencies is available. Alternatively, Resonant-tunneling diodes (RTDs) provide an efficient way of generating signals at high frequencies. Oscillators with f_{max} of 1.98 THz have been demonstrated [9].

Millimeter wave signal generation can be realized with different topologies. Commonly, a oscillation in the gigahertz range is converted to the target mm-wave frequency by harmonic frequency generation. For modulation, the signal is then mixed with a baseband signal, before it is amplified by a power amplifier (PA) and fed to the transmitting antenna. Harmonic frequency generation in multipliers and mixers is usually an inefficient process and, therefore, direct generation of the mm-wave signal would be beneficial. This chapter will discuss the implementation of an efficient pulse generator circuit, generating the pulses directly at the mm-wave frequency. The oscillator topology is based on a RTDs oscillation circuit, controlled by a III-V metal-oxide-semiconductor field-effect transistor (MOSFET). A control signal sets the duty cycle of the generated pulses, whereas current consumption in the off state is negligible. The circuit was designed in the scope of previous doctoral theses [10–12]. In this work, the previously developed fabrication process was applied and optimized.

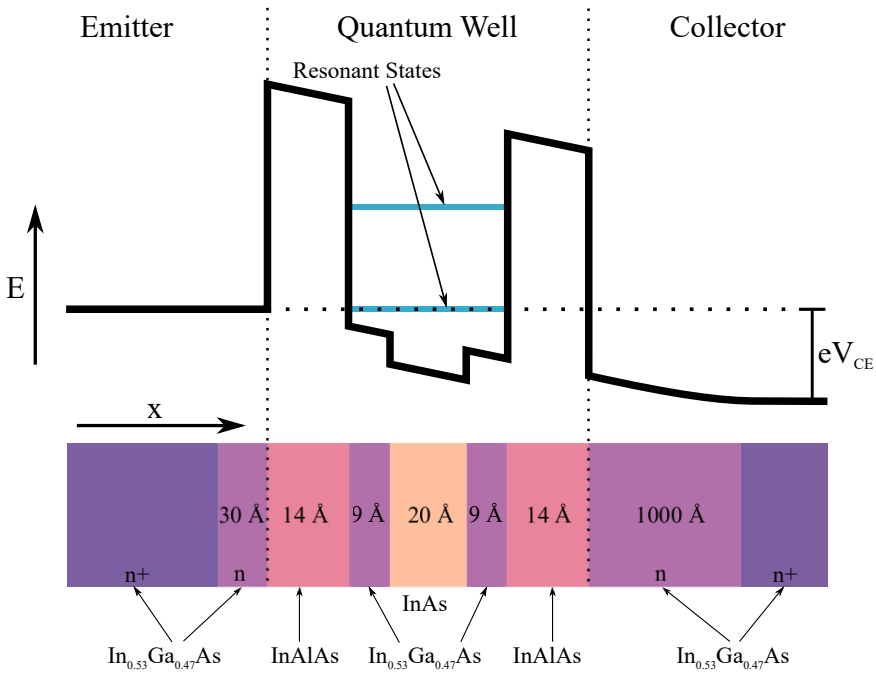

Figure 3.1: The band diagram of a RTD formed by a double barrier heterostructure (DBH). The different band gaps of the materials create a quantum well with discrete energy states. Tunneling through the barriers is only possible, if the energy of the electron is the same as the discrete energy state in the well. The used material system is InGaAs with InAlAs as barriers and InAs as quantum well.

3.1 THE RESONANT TUNNELING DIODE

The core of the circuit, used in this thesis, is a resonant-tunneling diode (RTD). In this section, the operation of the RTD will be summarized qualitatively. More detailed descriptions are available in literature [13].

The RTD consists of a quantum well structure, formed by a stack of semiconductors with different band gap. A schematic of the layer structure of the RTD and the according band structure is sketched in Fig. 3.1. The energy barriers of the quantum well prevent electrons from moving from the collector side to the emitter. In the quantum well discrete energy states exist. Electrons are only able to tunnel to the state in the quantum well, when their energy is to be equal to the state's energy. The distribution of the electrons in the conduction band on the emitter side is given by the product of the Fermi-Dirac distribution and the density of states. This means that most

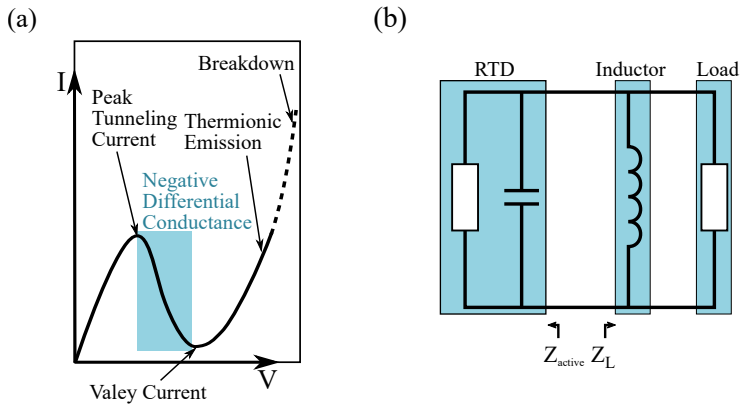

Figure 3.2: (a) The Current-Voltage characteristic of a RTD. The curve exhibits a negative differential conductance (NDC), i.e., the current drops after the peak tunneling current. (b) Simplified equivalent circuit of a RTD oscillator. Due to the NDC, the circuit will start oscillating if a inductance is connected to the output.

electrons are close to the conduction band edge and tunneling is unlikely in the equilibrium case. When a voltage is applied to the device, the potential of the collector is moved respectively to the emitter. Due to band bending, the energy level in the quantum well is lowered. Since the quantum well state moves closer to the conduction band edge, where more electrons are present, the tunneling probability is increased. The electrons in the quantum well are likely to tunnel to the collector side, since plenty of free states exist there and the electrons can relax to a lower energy state. With increasing bias voltage the tunneling probability increases. A maximum is reached when the energy level is aligned with the maximum of the electron distribution on the emitter side. Increasing the voltage further causes a drop in the tunneling current. Eventually, the current rises again when a second energy state in the quantum well is reached or when the device breaks down through thermionic emission. The resulting current-voltage characteristic of the RTD is shown in Fig. 3.2 (a). The tunneling current increases with increasing voltage, until a maximum is reached and the tunneling current decreases again. This region exhibits a negative differential conductance (NDC), as seen by the negative slope in the curve.

3.2 RTD OSCILLATORS

RTDs provide an efficient way of generating signals at high frequencies. An intuitive way to understand RTD oscillators is to use the design method for negative differential resistance (NDR) oscillators [14]. Hereby, the oscillation criterion is given by

$$Z_{\text{active}} + Z_{\text{L}} = 0, \tag{3.1}$$

where Z_{active} is the impedance of the active circuit part, i.e., the RTD, and Z_{L} the impedance of the output network. A simplified schematic of this configuration is depicted in Fig. 3.2 (b). The RTD can be represented with a small signal equivalent. In a simple model, the RTD can be modeled by a negative resistance in parallel with a capacitance [15]. If the RTD is biased in the NDC region, the real part of Z_{active} is negative and, therefore, able to compensate a positive load resistance in Z_{L}. Since the RTD is intrinsically capacitive, the circuit will start oscillating if Z_{L} is inductive. This fact makes characterization of RTDs in the NDC region difficult, since any inductance in the measurement setup will cause an oscillation. For characterization, the device needs to be stabilized [16]. On the other hand, this property can be used for the design of oscillator circuits. The size of the inductance determines the frequency where (3.1) is fulfilled. Therefore, an oscillator can be designed by connecting an inductor and a load impedance to the RTD.

Different topologies for RTD oscillators have been proposed [9,17–25]. Some of these approaches include means for modulating the circuit. For instance, gated tunneling diodes have been used to control the band structure of the RTD by the field effect [21, 22]. The most common approach is to control the bias point of the RTD by modulating the bias voltage. Switching the bias point between the resistive and the NDC operation allows the implementation of an on-off keying (OOK) modulated output [24, 25]. In this thesis, a MOSFET is used to control the bias point of the RTD [23]. If the gate signal of the MOSFET is above the switching threshold, the RTD operates in the NDC region. Below threshold, on the other hand, no current is flowing through the RTD and the oscillation criteria are not fulfilled. This can be used to generate short coherent pulses, oscillating at the designated frequency, when a suitable square wave signal is applied to the gate to the transistor.

3.3 RTD-MOSFET PULSE GENERATOR IMPLEMENTATION

The RTD oscillator, used in this thesis, is implemented and fabricated using in-house III-V semiconductor technology. The process was developed in previous work [23, 26] and adapted for the purpose of circuit fabrication.

An overview of the circuit topology is given in Fig. 3.3 (a). The core of

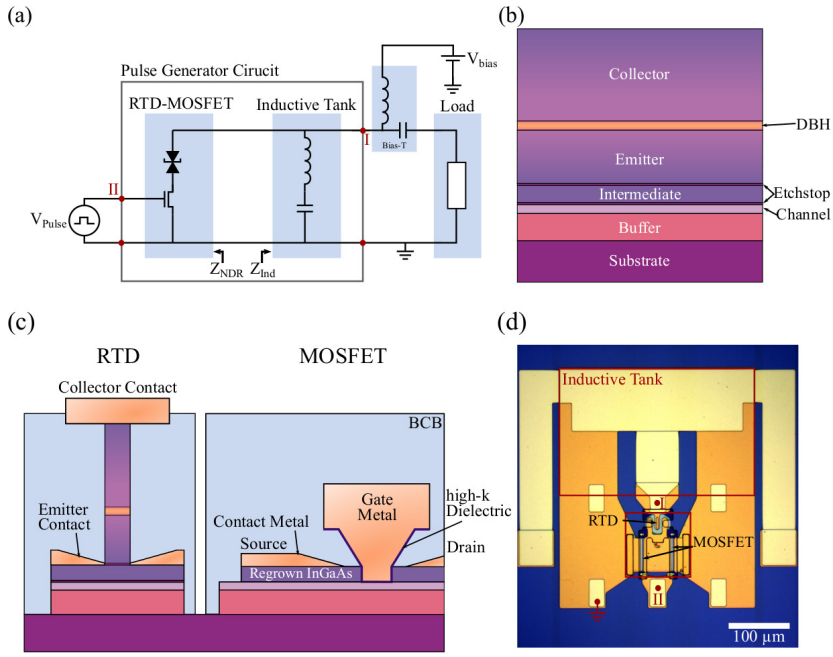

Figure 3.3: (a) The circuit diagram of the RTD-MOSFET pulse generator. A MOSFET is used to control the bias of a RTD. The gate signal is supplied by an external square pulse generator. A coplanar waveguide, terminated by a capacitor, acts as inductive tank. Bias is supplied in the output path through a bias tee. (b) Fabrication of the circuit starts with a layer structure grown by molecular beam epitaxy (MBE). The structure includes the DBH of the RTD and the channel layer of the MOSFET. (c) Structure of the RTD and the MOSFET after fabrication. (d) A chip photograph of the RTD-MOSFET pulse generator fabricated in-house.

the oscillator is an InGaAs/AlAs RTD and an InGaAs MOSFET. The base of the fabrication process is a wafer, coated with multiple semiconductor layers. This layer structure, grown by MBE, is shown in Fig. 3.3 (b). In the first step of circuit fabrication, the RTD mesa is defined. This is done by wet etching the layer structure down to the MOSFET channel layer, leaving the mesa only at the location of the RTD. The transistors are defined with electron beam lithography (EBL) by a dummy gate formed of the resist hydrogen silsesquioxane (HSQ). Subsequently, an InGaAs contact layer and a sacrificial InP layer are regrown by metal-organic vapour-phase epitaxy (MOCVD). After removing the dummy gate, the gate oxide (Al_2O_3/HfO_2) is deposited using atomic layer deposition (ALD) and thermal evaporation, respectively.

The sacrificial InP layer is removed by wet etching to form a T-shaped gate structure. A metal layer acting as collector contact of the RTD is deposited by thermal evaporation. In the following wet-etching step, the contact metal acts as etch mask for the definition of the RTD. The rest of the sample is protected by a resist layer to prevent etching of the transistor structure. In the next step, the emitter contact of the RTD and the source and drain contact of the MOSFET are deposited. The sample is tilted in this evaporation step to reduce access resistances, while the collector contact and the gate act as shadow mask. The low permittivity dielectric benzocyclobutene (BCB) is used to isolate the structure from the following interconnect layers. Subsequently, a metal layer is deposited to connect the circuit and form a coplanar waveguide stub acting as inductor for the oscillator circuit. The stub is terminated by a large metal-insulator-metal (MIM) capacitor acting as RF short circuit and bias stabilization [27]. The capacitor is formed by deposition of a HfO_2 layer by ALD and an additional metal layer. A schematic cross-section of the fabricated devices and a chip photograph is shown in Fig. 3.3 (c) and (d), respectively. A detailed list of the full fabrication process can be found in Appendix A.

3.4 FABRICATION PROCESS OPTIMIZATION

In the scope of this thesis, the contact resistance in the circuit fabrication process was optimized. Any additional series resistance of the RTD and MOSFET decreases the magnitude of the NDC. Consequently, the maximum oscillation frequency and the output power of the circuit are reduced. To be able to reliably design mm-wave circuits, good process control and a low contact resistance are critical.

At a metal-semiconductor interface, a Schottky barrier is formed due to the different work function of the materials. The doping level of the semiconductor determines if the Schottky barrier is dominant or an ohmic contact is achieved at the interface [28]. For the fabrication of good contacts to InGaAs in HEMTs and MOSFETs, often an additional InGaAs contact layer is regrown before metal contacts are evaporated in a second step [29–32]. The regrown InGaAs layer can have a very high doping and a higher indium content than the base layer, which has been shown to enable ohmic contacts with metals [33]. This two-step process is also used for the contacts at the drain and source of the MOSFET and the collector of the RTD in the fabrication process of the pulse generator.

For the fabrication of contacts in the circuit process, a 30 nm InGaAs layer is regrown by MOCVD, followed by a 110 nm layer of InP. The InP acts as support for the definition of a T-gate structure and is etched back from the contacts afterwards (cf. Section 3.3). After etching the sacrificial InP layer,

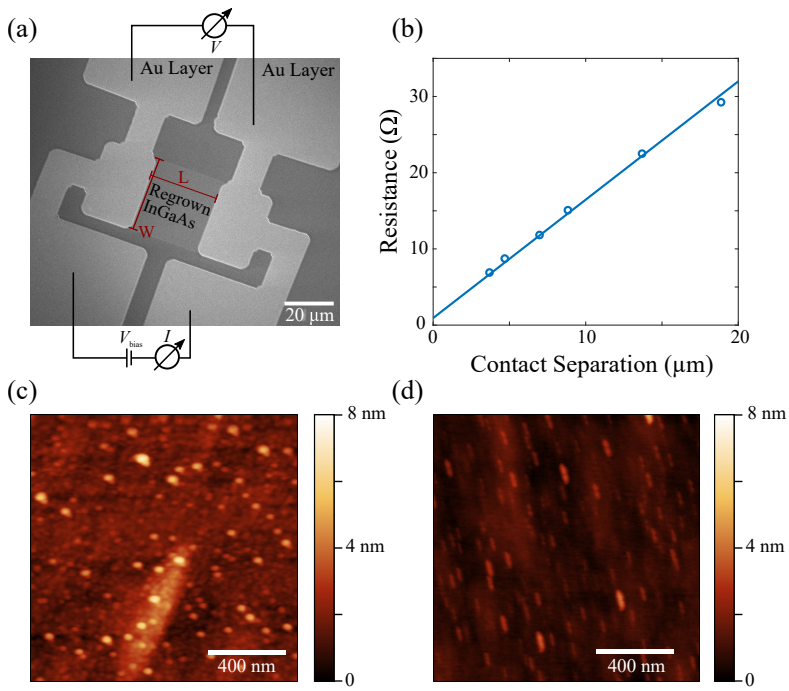

Figure 3.4: (a) scanning electron microscope (SEM) image of one of the fabricated TLM structures. Width and length of the structures are measured with the SEM for accurate modeling. (b) TLM measurement for one of the fabricated samples (TLM-2). (c) Semiconductor surface before contact regrowth for TLM-1. The surface is contaminated by particle residues, probably originating from the mesa etch with $H_3PO_2/H_2O_2/H_2O$. (d) Semiconductor surface before contact regrowth for TLM-2. Particle residues are smaller when the mesa is etched with $H_2SO_4/H_2O_2/H_2O$.

the contact metal stack consisting of 10 nm titanium (Ti), 25 nm palladium (Pd), and 300 nm gold (Au) is evaporated. Since the contact definition is a critical step during the fabrication process, the fabricated contacts were evaluated after the processing run using the transmission line method (TLM). In this method, contacts are fabricated at different distances. The resistances between the contacts can then be modeled with a distributed model, analogue to transmission lines. The resistance of the contacts can then be separated form the semiconductor [34].

For the first RTD-MOSFET pulse generator (PG-A), fabricated in the scope of this thesis, a new MBE grown wafer was used. No quantitative information on the values of contact resistance was available before fabrication. For circuits

fabricated priorly with other wafers, specific contact resistivities, ρ_c, in the range of 200-300 $\Omega/\mu m^2$ have been achieved. The first fabrication process on the new wafer (PG-A) gave a specific contact resistivity ρ_c of 1070 $\Omega/\mu m^2$. Compared to state of the art contacts to InGaAs with $\rho_c < 1\Omega/\mu m^2$ [35], all these contacts require improvement. A series of experiments was performed to systematically improve the contact resistance.

As starting point, dedicated samples with TLM structures were fabricated on the MBE grown wafer as substrate. The fabrication process included all necessary steps to fabricate the contacts in the same way as they occur in the circuit fabrication process. First, the RTD mesa was structured by wet etching, before InGaAs and InP was regrown. The dummy InP layer was removed, just like in the pulse generator process, to reveal the contact layer. In the next step, the semiconductor was etched back by another wet-etching step, to isolate the TLM structures. Lastly, the contact metal was deposited. The resistance of the fabricated TLM structures was then measured with a parameter analyzer. To take fabrication uncertainties into account, width and length of the fabricated TLM structures were measured with a SEM. Only controlled changes to the process were introduced to evaluate the influence of a single step and additional inspection steps were introduced. One of the fabricated TLM structures is shown in Fig. 3.4 (a).

The first experiment (TLM-1) was to change the material composition in the regrow of the contact layer. A layer with higher indium content, $In_{0.63}Ga_{0.37}As$ instead of $In_{0.53}Ga_{0.47}As$, was grown. Additionally, the doping was kept activated during half of the growth of the sacrificial InP layer, to increase the dopant concentration on top of the InGaAs. The contact resistivity in this case improved to $\rho_c = 310\Omega/\mu m^2$. An investigation of the semiconductor surface before regrowth with an atomic force microscope (AFM) revealed a reproducible contamination with unidentified particles, approximately 7 nm in size. The AFM image of the contaminated surface is displayed in Fig. 3.4 (c). To investigate the origin of these particles, differences in the mesa etch were investigated. A new mesa etch recipe was developed to investigate the influence of the mesa wet etch. A highly diluted solution of $H_2SO_4/H_2O_2/H_2O$ in the ratio 1:1:60 was prepared. The semiconductor surface after mesa etch with the new etchant and before regrowth is shown in Fig. 3.4 (c). Particles are still present with the new etching recipe, however, the particle size reduced to below 5 nm. TLM structures with the new recipe were fabricated (TLM-2). A very low contact resistance of $\rho_c = 4\ \Omega/\mu m^2$ was achieved. For this sample, the measured resistance of the TLM structures in dependence of the contact separation is plotted in Fig. 3.4 (b).

With the newly developed contact recipe, another run for circuit fabrication was performed. The specific contact resistivity achieved in this run was: $\rho_c = 150\ \Omega/\mu m^2$. A summary of the contact resistance evaluation is given

Table 3.1: Summary of Contact Characterization

Sample	Mesa Etch	Regrowth	$\rho_c(\Omega/\mu m^2)$
PG	Previous circuits on different wafer		~200
PG-A	$H_3PO_2/H_2O_2/H_2O$	$In_{0.53}Ga_{0.47}As/InP$	1070
TLM-1	$H_3PO_2/H_2O_2/H_2O$	$In_{0.63}Ga_{0.37}As/InP(n)/InP$	310
TLM-2	$H_2SO_4/H_2O_2/H_2O$	$In_{0.63}Ga_{0.37}As/InP(n)/InP$	4
PG-B	$H_2SO_4/H_2O_2/H_2O$	$In_{0.63}Ga_{0.37}As/InP(n)/InP$	150

in Table 3.1. The results demonstrate that the contact resistance in the full fabrication process still has room for improvement. However, the results are one order of magnitude better than the previous fabrication run (PG-A) and slightly better than the contact resistance achieved in previous circuits. The complete processing recipe of the improved pulse generator is summarized in Appendix A.

3.5 REVIEW OF RECEIVER CONCEPTS

The receiver presents an essential part of any radar system. Implementation and design of a receiver monolithic microwave integrated circuit (MMIC) was, however, outside of the scope of this thesis. Instead different laboratory setups were used to receive the pulses. This section provides an overview of coherent receiver concepts that may be implemented for the detection of the generated mm-wave pulses. A more broad overview, including non-coherent receivers, can be found in [11]. The laboratory setups used for reception of pulses in this thesis will be presented in Chapter 5.

Implementing receivers for mm-wave systems like radars or high-speed communication devices is subject to current research. An overview of some possible coherent detector topologies is shown in Fig. 3.5. Wide bandwidth, power consumption, and high-data rates put constrains on the design of those receivers. Coherent down-conversion is by far the most common way to implement coherent mm-wave receivers [36,37]. A schematic of this approach is given in Fig. 3.5 (a). By frequency mixing, the difference frequency of the received signal and a LO is generated. Using two mixer stages with phase shifted LOs, the phase of the received signal can be reconstructed. Another coherent receiver approach is direct reception using a six-port interferometer, as shown in Fig. 3.5 (b). A six-port interferometer architecture has been proposed as coherent receiver for micro- and mm-wave systems [38]. Using the

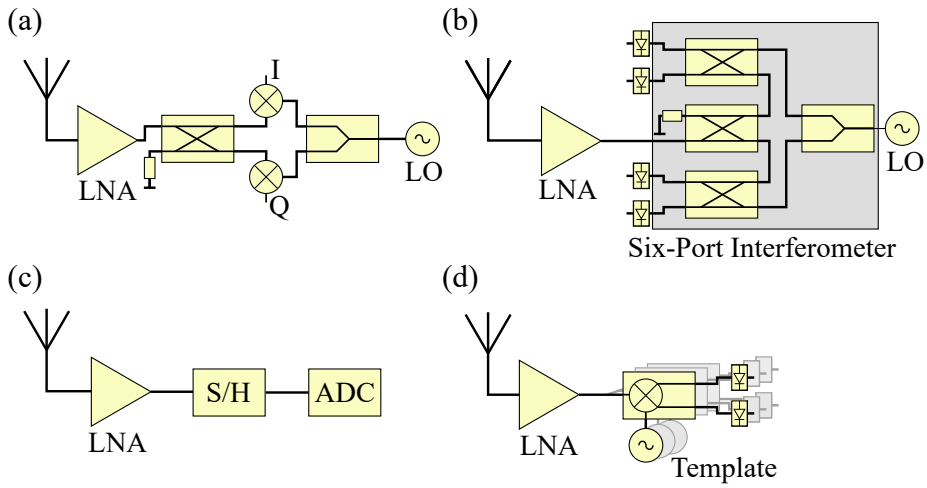

Figure 3.5: An overview of coherent receiver concepts. (a) Two phase shifted versions of the received signal are converted to an intermediate frequency (IF) by mixing with anlocal oscillator (LO), giving an in-phase (I) and quadrature-phase (Q) signal. (b) The received signal and a LO are feed in a six port interferometer. The outputs of the interferometer are down-converted by energy detectors and digitized. (c) The signal is sampled directly at the mm-wave frequency. If the signal is under-sampled, aliases are generated in baseband (d) In an analog template receiver, the signal is correlated with a local template signal, i.e. the transmitted waveform at a certain delay.

intrinsic phase shift of branch-line couplers, the interference between signal and LO can be generated at 4 different phase shifts. From these interference components the I and Q component of the signal can be generated. A good review of six-port based radar systems can be found in [39]. A third approach is to convert the RF signal directly to the digital domain with a sampling circuit. With the development of high speed analogue digital converters, this technique might become possible at mm-wave frequencies. By under-sampling a band limited RF signal, aliased signals at multiples of the sampling frequency are generated. This can be used to convert the signal directly to baseband [40–43]. The required sampling speed is, hereby, set by the signal bandwidth, while the sample and hold input stage needs to be able to cover the full analogue bandwidth. A schematic of this receiver approach is summarized in Fig. 3.5 (c). If this technology is suitable for wideband mm-wave pulses at 60 GHz and higher, needs to be demonstrated. Another promising approach is using an analog correlator as receiver [11, 44–47]. The basic schematic of this receiver architecture is shown in Fig. 3.5 (d). A mixer correlates the received signal with a local template, which is a delayed version

of the transmitted waveform. When received signal and template coincide, a baseband signal is generated. To generate range information, the delay of the template can be either varied iteratively, by sampling the range signal, or in parallel, by using multiple correlator banks. All of the presented receiver topologies have their advantages and disadvantages. Which approach is most practical for the implementation of a low-power mm-wave radar needs to be demonstrated in a system implementation.

4

Radar Waveforms

The waveform used as radar signal is an important aspect in radar system design. The range resolution is directly related to the waveform bandwidth. The energy of the waveform, setting the achievable signal-to-noise ratio (SNR) of a radar system, is related to the duration of the waveform and the peak transmitted power. Modern radar systems, therefore, transmit modulated pulses, to achieve a high bandwidth with as long waveforms as possible. Frequency modulated continuous wave (FMCW) radar is a popular technique, since high performance systems can be build with low system complexity [48]. In this thesis, radar waveforms generated by the RTD-MOSFET pulse generator were investigated. The architecture of the circuit allows to minimize power dissipation in the waveform generation, since the millimeter-wave (mm-wave) oscillator is only active during pulse generation. However, the simple transmitter architecture limits the waveforms which can be generated by the circuit. The circuit is designed to be controlled by the input signal of the metal-oxide-semiconductor field-effect transistor (MOSFET). If the control signal is above the switching threshold, the pulse generator is active. Below the threshold the oscillation is suppressed. Therefore, traditional radar modulation schemes like linear frequency modulation or Barker coded waveforms cannot be directly realized. This chapter contains an overview over radar waveforms that can be generated with the RTD-MOSFET pulse generator. First, the properties of single mm-wave pulses will be presented. Then the method for generating phase correlated duo-binary waveforms, as presented in Paper I, will be introduced. This method shows that high performance modulated waveforms can be directly generated with the RTD-MOSFET pulse generator without power loss.

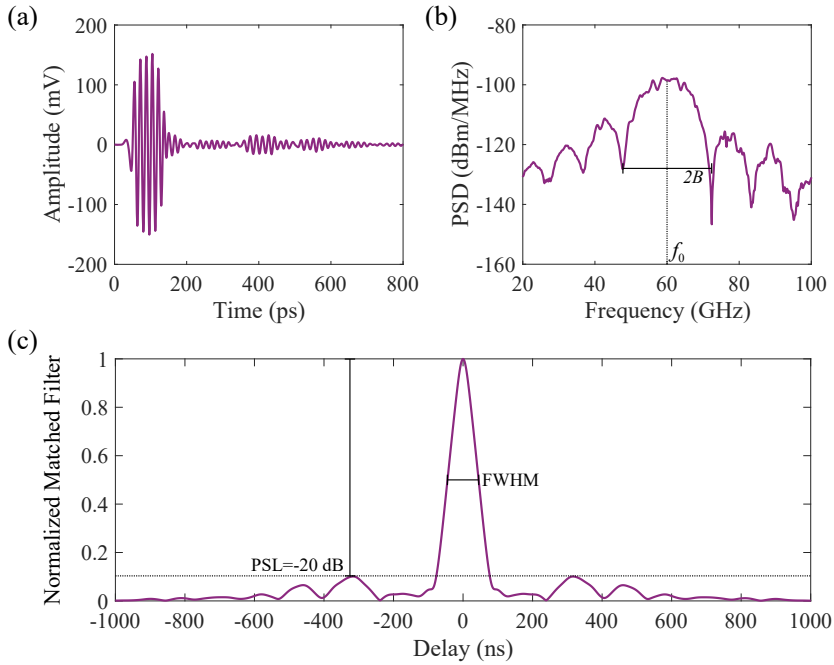

Figure 4.1: (a) A single mm-wave pulse, generated by a RTD-MOSFET circuit. (b) The power spectral density of the pulse for a pulse repetition interval of 10 ns. The pulse has a half sided bandwidth $B = 12.5\ GHz$. (c) The matched filter response. The full width half maximum (FWHM) is 90 ps, resulting in range resolution of $\Delta R = 1.35$ cm. Ringing after the pulse causes side lobes with a peak side lobe level (PSL) 20 dB below the center peak.

4.1 SINGLE PULSE PROPERTIES

The simplest waveform that can be generated with the described RTD-MOSFET circuit is a single mm-wave burst. This mm-wave pulse can be directly used as radar signal, comparable to traditional pulsed radar systems [2]. After transmitting the pulse, the receiver is active, waiting for the delayed echoes of the transmitted pulse. As discussed in Chapter 3, the pulse duration can be controlled externally by applying a signal above the switching threshold to the gate of the transistor. By applying a square wave signal, it is straight forward to generate pulses at any desired pulse repetition interval (PRI). Pulses with a length down to 25 ps have been demonstrated [26]. The generated pulses are coherent, i.e., the start-up phase of the pulses is identical for each pulse.

An example of a pulse with an oscillation frequency, $f_0 = 60$ GHz, and a pulse length of 80 ps is shown in Fig. 4.1 (a). In few oscillation cycles, the pulse starts oscillating with the frequency $f_0 = 60$ GHz. After switching off the control signal, the pulse decays rapidly. Some ringing appears after the pulse, which is caused by unwanted reflections in the measurement setup. The power spectrum of the pulse is given in Fig. 4.1 (b). The pulse is centered around $f_0 = 60$ GHz with a single sided bandwidth, $B = 12.5$ GHz. The peak power spectral density (PSD) is dependent on the pulse peak power and the PRI. Pulses with a peak power of approximately 7 dB have been demonstrated [23]. The example in Fig. 4.1 was measured with a generator with 0 dBm peak power and a cable with an additional insertion loss of approximately 6 dB. For the PRI of 10 ns, this results in a peak PSD of -97.7 dBm/MHz. For the application in radar, it is common to use a matched filter to discriminate the received pulses from noise (cf. Section 2.1). The matched filter response of a single pulse, calculated by its autocorrelation, is shown in Fig. 4.1 (c). It shows a peak at zero delay with a FWHM of 90 ps. This corresponds to a range resolution of $\Delta R = 1.35$ cm. The ringing after the pulse causes range side lobes in the matched filter response, which prevent the detection of weak targets in the vicinity of another target. For the pulse in Fig. 4.1 (c) the peak side lobe level (PSL) is 20 dB below the maximum of the center peak.

The use of single pulses as radar waveforms has several limitations. The amplitude of the generated pulses is finite, which limits the detection sensitivity when a pulse like in the example is used. One possibility to increase the sensitivity would be to increase the transmitted energy by generating longer pulses. This, however, decreases the bandwidth and the range resolution of the pulse. Alternatively, the sensitivity in signal acquisition can be increased by coherently averaging over multiple pulses. However, this decreases the acquisition speed of the measurement. Also, moving objects prevent the use of averaging, since the coherence is destroyed by the movement. Hence, the use of pulses as radar waveform requires a strict trade-off between sensitivity, resolution, and acquisition speed. In modern radar systems, waveforms using pulse compression by frequency or phase modulation are often preferred.

4.2 PHASE-CORRELATED DUO-BINARY WAVEFORMS

To apply conventional pulse compression techniques like phase coded waveforms [6] with RTD-MOSFET pulse generators, is not straight forward. In Paper I, phase-correlated duo-binary waveform generation, a novel technique for the generation of modulated radar waveforms, is introduced. A delay is used to modulate the phase of generated pulses, similar to delay-based binary phase-shift-keying (DB-BPSK) [49]. This is achieved by synchronizing

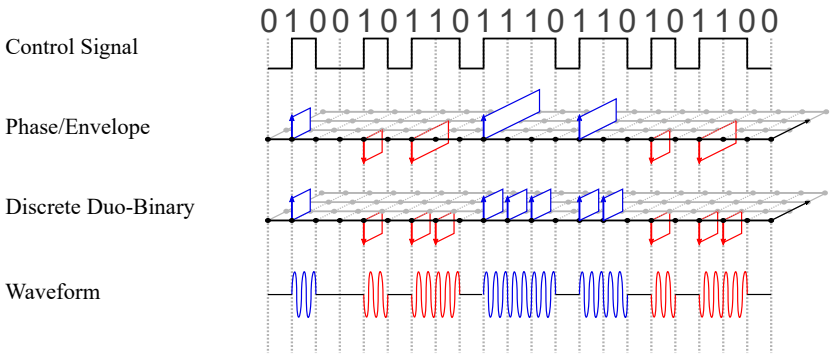

Figure 4.2: The principle of phase correlated duo-binary waveform generation with the RTD-MOSFET pulse generator. The phase of a generated waveform can be modulated, by synchronizing the oscillation frequency, f_0, to the chip rate, T_{Chip}, of the control signal. The envelope of generated pulses is defined by the rising flanks (transitions from "0" to "1") and the length of the control signal. For the duo-binary case, the phase is positive or negative, depending if the flank occurs on an even or odd chip, respectively. The signal can be expressed with a discrete duo-binary sequence, where a variable c_n takes values of -1, 0, and 1.

the oscillation frequency, f_0, to the chip rate, $1/T_{\text{chip}}$, of a non-return-to-zero (NRZ) binary control signal. No additional delay circuits or pulse carving filters are necessary. The phase, ϕ_n, of each pulse in a generated pulse sequence is given by:

$$\phi_n = n2\pi f_0 T_{\text{chip}}. \tag{4.1}$$

If the control signal is synchronized to the oscillation frequency so that $f_0 T_{\text{chip}}$ is an integer number, the phase shift is always multiples of 2π. All generated pulses are in phase for this case. If the remainder of $f_0 T_{\text{chip}}$ is 0.5, on the other hand, ϕ_n is altering between 0 and π. A schematic of the generation principle of the phase-correlated duo-binary waveforms is shown in Fig. 4.2. The phase of pulses in the sequence is set by the starting instance, i.e., the transition from “0” to “1” in the control signal. Consecutive “1” in the control signal mean that the phase is the same as in the previous state. The waveforms can be expressed with a discrete duo-binary sequence:

$$x(t) = \sum_n c_n A(t - nT_{\text{chip}}), \tag{4.2}$$

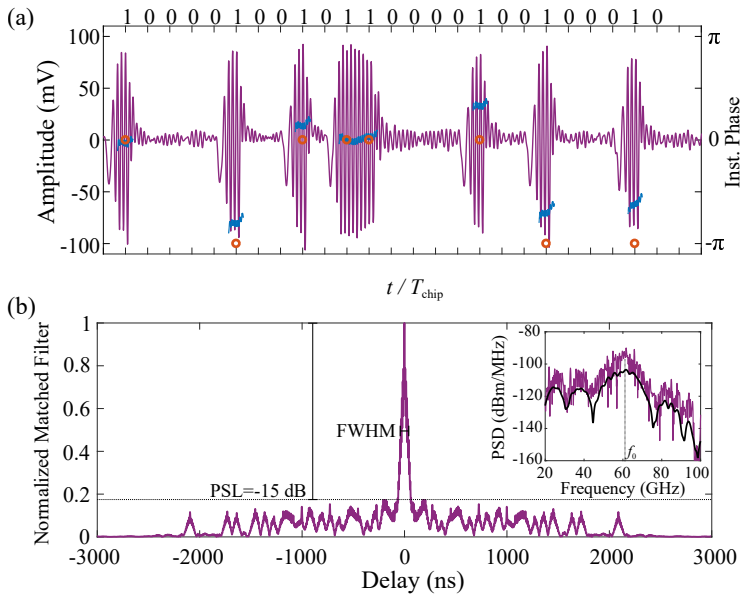

Figure 4.3: a) An example of a phase-correlated duo-binary waveform that can be generated by the RTD-MOSFET circuit. The instantaneous phase according to theory (red) and measurement (blue) is overlayed over the pulses. b) The matched filter response. The FWHM is 70 ps, resulting in range resolution of $\Delta R = 1.05$ cm. The inlay shows the PSD of the phase-correlated duo-binary waveform (purple), in comparison with the PSD of a single pulse (black). The phase-correlated duo-binary waveform, has an approximately 13 dB higher peak PSD than the single pulse.

where $A(t - nT_{\text{chip}})$ is the unit envelope function of the length of one chip, T_{chip}, and

$$c_n = \begin{cases} 0, & \text{for } a_n = 0 \text{ and arbitrary } a_{n-1}, c_{n-1} \\ (-1)^n, & \text{for } a_n = 1 \text{ and } a_{n-1} = 0 \text{ and } c_{n-1} = 0 \\ c_{n-1} & \text{for } a_n = 1 \text{ and } a_{n-1} = 1 \text{ and } c_{n-1} \neq 0 \end{cases} \tag{4.3}$$

The waveform has three allowed states: 0, 1, and -1, analogous to duo-binary signals [50]. However, the phase in the sequence cannot be set independently. It is correlated with the position in the sequence. To differentiate the waveform generation technique from existing methods, the name phase-correlated duo-binary waveform was introduced in Paper I.

Phase-correlated duo-binary waveforms can be used as high resolution radar signals. The concept is to transmit long sequences of pulses and,

hereby, increase the transmitted energy of the waveform. These modulated waveforms are designed to be compressed by a matched filter, concentrating the energy of the waveform at the delay of the target. For many waveforms, side lobes appear in the matched filter response, which limit the detection of weak targets. The phase-correlated duo-binary waveforms are conceptually similar to staggered pulse sequences [6, 51, 52], which are generated by a sequence of pulses without phase shift. Just like for these sequences, the PSL is limited by the energy of a single pulse. Optimal radar waveforms for pulse trains as well as for phase-correlated duo-binary sequences are, therefore, sequences with a PSL equal to the energy of a single pulse. The center peak in the matched filter response, on the other hand, increases with an increasing number of pulses. The key is to find optimal sequences with as many pulses as possible. In Paper I, optimal phase-correlated duo-binary sequences with a length of up to 25 chips and 8 pulses are presented.

As an example of phase-correlated duo-binary waveforms, generated with the RTD-MOSFET pulse generator, Fig. 4.3 (a) shows the waveform generated by the binary control sequence `1000010010110000010010001`. The waveform is generated by a pulse generator with 60.5 GHz, the control signal has a T_{chip} of 91 ps. This means $f_0 T_{\text{chip}}$ is 5.5, which enables the generation of phase-correlated duo-binary waveforms. The sequence has 8 chips with a "1" and, therefore, carries 8 times the energy as a single pulse. This is visible in the PSD of the waveform, plotted in the inlay in Fig. 4.3 (b). Compared to a single pulse, the peak PSD is approximately 13 dB higher. The bandwidth of the waveform, on the other hand, is approximately the same as the bandwidth of a single pulse. The instantaneous phase of the pulses in Fig. 4.3 (a) demonstrates that the pulses are phase modulated. There is some deviation from the ideal behavior of the phase described by (4.3). This deviation is caused by imperfect starting conditions for closely spaced pulses. The bias stabilization capacitor in the circuit discharges during each pulse and doesn't have enough time to charge again. The matched filter response of the waveform is depicted in 4.3 (b). The FWHM of the matched filter response is 70 ps, which corresponds to a range resolution of $\Delta R = 1.05$ cm. This shows that high resolution waveforms can be generated with this technique. Side lobes occur, which limit the detection of weak targets. However, the achieved PSL of -15 dB still offers a good dynamic range. The phase-correlated duo-binary waveforms can be used as a radar waveform with increased gain, compared to single pulse waveforms. This is important for the use in low power applications, as for instance gesture recognition in battery-powered, hand-held devices. In Paper V, the detection of radar reflections, scattered on the human hand, has been demonstrated with this technique. More details about the use for gesture recognition systems will be discussed in Chapter 7.

5

Measurement Setup and Calibration

Radar systems are highly sensitive towards any interaction of the transmitted electromagnetic waves with the environment. To develop the signal analysis for radar systems, it is beneficial to measure in a laboratory environment, where the environment can be controlled and monitored. This enables the development of calibration routines, which will aid data analysis in the real application, but also provide high precision measurements that aid future system design. Further, prototype architectures can be tested, which will aid the future implementation of integrated systems. In this thesis, different laboratory setups were developed to evaluate the use of the millimeter-wave (mm-wave) pulse generator in various applications. This chapter presents an overview over the used equipment and considerations about calibration of the measurements.

5.1 MEASUREMENT SETUP OVERVIEW

The core of the presented measurements is the pulse generator circuit, described in Chapter 3. The circuit was typically contacted using coplanar ground-signal-ground (GSG) probes. These probes were positioned with a Karl Süss PSM 6 probe station. To perform free-space measurements, antennas were either mounted directly on the output probe, or a short coaxial cable was used to transmit the pulse to the antennas mounted on a holder next to the probe station. An example of a measurement configuration is shown in Fig. 5.1 (a). To allow more flexible measurement configurations, a modular probing setup on an optical table was developed. The probing parts are more compact than in the commercial probe station and unnecessary parts can be removed when they are not needed. The microscope, for instance, can be removed after probing the circuit. This way, obstruction or unwanted

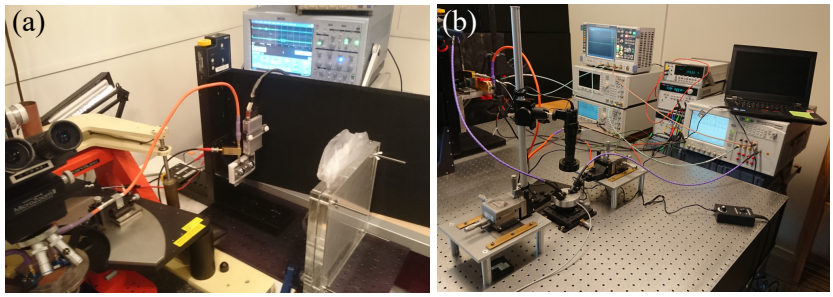

Figure 5.1: Photographs of different measurement setups a) Setup using a commercial probe station b) Custom built probing setup on an optical table

scattering in the free-space path can be avoided. A photograph of this measurement configuration is shown in Fig. 5.1 (b). More details about the custom measurement setup and the parts used can be found in Appendix B.

As antennas for free-space measurements, either V-band standard gain horn antennas with a nominal gain of 20 dBi or specially designed leaky-lens antennas were used. These very wideband antennas with 16 dBi gain show low dispersion and allow a nearly undistorted transmission of the generated mm-wave pulses [53, 54]. A full radar system was implemented by several commercial instruments. Two principle variants of the measurement setup with different receiver configurations were developed. A block diagram of these setups is shown in Fig. 5.2. The common transmitter part consisted of the RTD-MOSFET pulse generator circuit, an Agilent N4906B bit-error-rate tester, and an Agilent E8257D signal generator. The Agilent N4906B bit-error-rate tester provided the non-return-to-zero (NRZ) binary baseband input to the pulse generator. Its clock reference in the range of 10 to 12.5 GHz was supplied by an Agilent E8257D signal generator.

For the first receiver configuration, shown in Fig. 5.2 (a), a coherent interleaved sampling oscilloscope (LeCroy WaveExpert 100H with a SE-100/SE-70 sampling head) was used. Multiple instances of a coherent signal with fixed period are sampled with a rate much lower than the Nyquist limit, but synchronized to a shifted reference. From these, the signal can be reconstructed. The prerequisite for using this technique is that the signal is repeating and coherent during the full acquisition interval. As shown in Fig. 5.2 (a), the sampling oscilloscope was synchronized to the baseband signal by using the clock output of the bit-error-rate tester as trigger input. Since this receiver method uses multiple instances of the pulse to detect the signal, measurements cannot be taken in real time. Detection of moving objects is, therefore, only possible, if movement is so slow that the coherence requirement is not violated. For static measurements the sensitivity of this

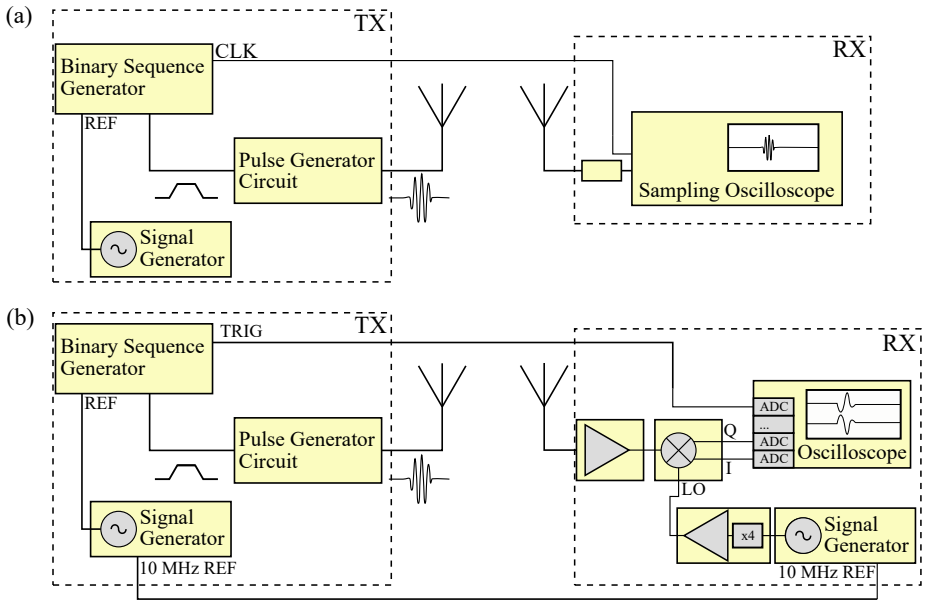

Figure 5.2: Block diagram of two measurement setup configurations. The basic Transmitter (TX) configuration is identical for both setups. (a) The measurement configuration using a sampling oscilloscope with coherent interleaved sampling as receiver (RX). (b) A configuration with a coherent down-conversion receiver (RX).

measurement method can be increased by averaging the signal. Implementing the techniques used in sampling oscilloscopes in integrated radar receiver is impractical. The accuracy of these instruments can't be realized in efficient system implementations. For a real system, receiver concepts as discussed in Section 3.5 might be more feasible.

A more realistic approach to receive mm-wave signals, is down-conversion with a heterodyne coherent receiver. This approach was also realized in a laboratory setup. The block diagram for this configuration is shown in Fig. 5.2 (b). A Millitech MIQ-15-01900 IQ-mixer was used to generate the harmonic difference frequency of the mm-wave signal and a heterodyne local oscillator (LO). The mixer generates an in-phase (I) and quadrature-phase (Q) component of the signal at an intermediate frequency (IF). The I and Q components can then be used to represent the analytical signal of the pulse. Critical for this technique is that the LO is synchronized to the control signal of the pulse to ensure coherent demodulation. In the laboratory, setup this was achieved by synchronizing two Agilent E8257D signal generators with a 10 MHz reference. One signal generator is used as baseband reference for the

pulse generator. The other signal generator, in combination with a Millitech AMC-15-RFH00 multiplier, provided the LO of the Mixer. The IF signal was sampled directly with an oscilloscope (Tectronix TDS7404 or R&S RTO 1044) and then processed digitally. To accurately detect a pulse, the bandwidth of the oscilloscope should be large enough to fit the down-converted main lobe of the pulse around the IF. This setup works in real time and single pulses or modulated waveforms can be used. To increase the sensitivity in this setup a HXI HLNAV-383 low noise amplifier (LNA) with a gain of 30 dB and a noise figure of 5.2 dB was used.

5.2 MATERIAL MEASUREMENTS AND CALIBRATION

Knowing the dielectric properties of materials is important for many radio frequency (RF) and mm-wave applications, from the design of integrated circuits to the design of antenna radomes. Various methods for characterizing the dielectric permittivity have been developed over the last decades [55]. The choice of the characterization method typically depends on the material properties. For low-loss materials, resonant methods, for instance with a split-cylinder resonator, enable measurements with good accuracy. For lossy materials, other methods are preferred, for example based on transmission lines [56].

Measurements in this thesis use a free-space method for material characterization. Material characterization with the mm-wave pulses, generated by the RTD-MOSFET pulse generator, has been demonstrated in a transmission setup in previous work [57]. Measuring the permittivity of materials in transmission is limited to materials under test (MUTs) with moderate losses or extremely thin slices of the MUT. In this thesis, a setup for characterizing the dielectric permittivity in reflection was developed. This measurement setup allows the evaluation of high loss MUTs in bulk, as demonstrated when measuring water and skin in Paper III.

For the quantitative measurement of the material permittivity, calibration with known calibration standards is necessary. For free-space setups, calibration using shifted reflectors or a shifted network as standards has been proposed [58–61]. Paper II presents an analysis of the unwanted reflections in the reflectometry setup with similar techniques. A schematic of the measurement setup used is shown in Fig. 5.3 (a). A 300x300 mm metal sheet was attached to a Thorlabs LTS300 translational stage. The metal reflector was swept in 1 mm steps from 200 mm to 300 mm distance and the reflection was recorded. Since the displacement of the reflector is known, the response from the target can be separated from position dependent clutter in the setup. The time-domain response of the measurement is shown in Fig. 5.3 (b). A

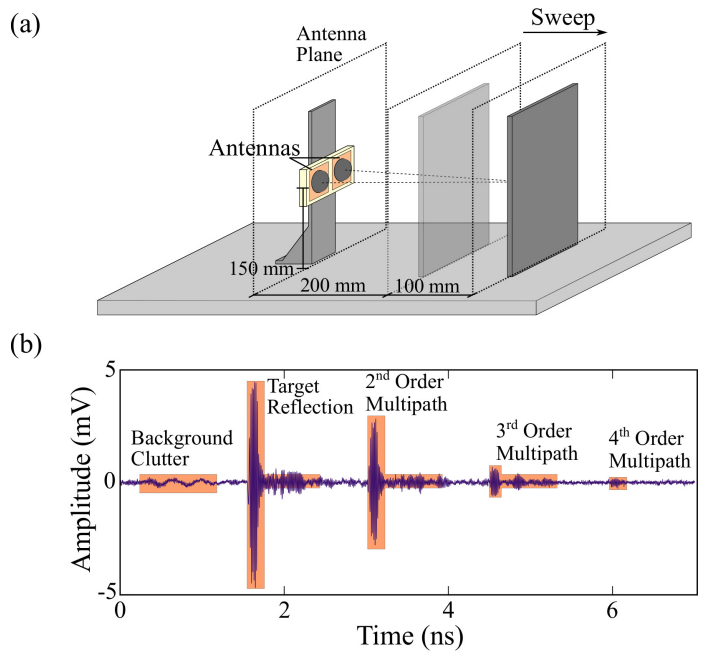

Figure 5.3: (a) Schematic of the reflectometry setup. To investigate the propagation in the setup, a metal reflector was swept from a distance of 200 mm to a distance of 300 mm in 1 mm steps. The reflection was recorded in each step. (b) The time-domain reflection signal recorded at one position. From the relation the displacement of the target reflection, multi-path reflections and static system clutter can be identified.

strong primary reflection from the target is visible. Weak static background clutter exists due to direct coupling from the transmitting to the receiving antenna. Multipath reflections between the target and transmitter, including its holding structure, appear at distinct locations corresponding to multiples of the distance of the target. The Multipath reflections are distorted and, therefore, have to be modeled position dependent. This prevents the direct application of shifted reflector calibration routines in the measurement setup. The primary reflection, however, is coherent and can be separated from the static background reflection by coherent superposition. For short pulses, multiple reflections are spatially separated from the primary reflection and can be removed by temporal gating of the signal [62–64]. For the material measurements, normalization and time-domain gating is used as calibration approach.

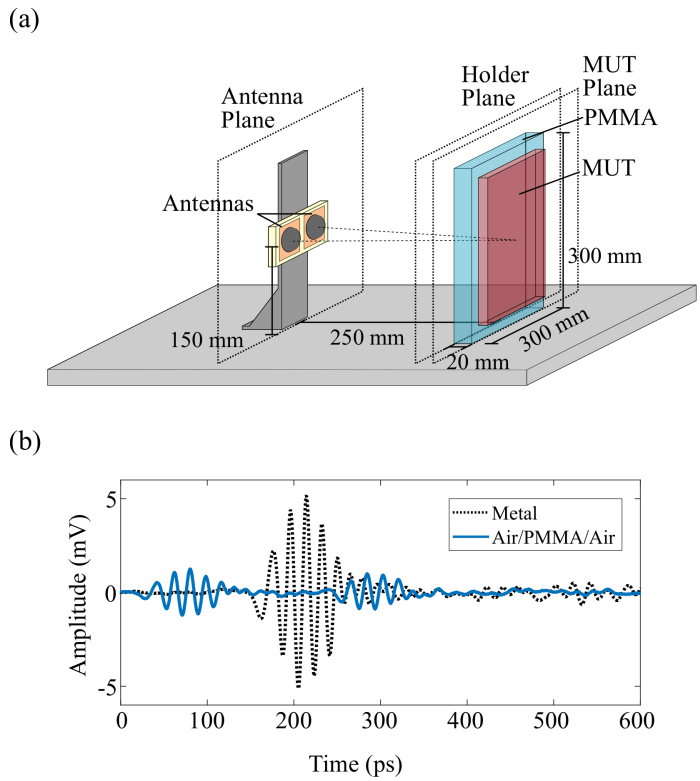

Figure 5.4: (a) Schematic of the permittivity measurement setup. (b) Time-domain reflection of the PMMA holder structure. The reflection from the reference metal reflector is shown dashed.

A sketch of the reflectometry setup for material measurements is shown in Fig. 5.4 (a). The wideband leaky lens antennas for transmitter and receiver are fixed with 5 degree tilt towards each other, 150 mm above an optical table. A 300x300x20 mm poly(methyl methacrylate) (PMMA) is positioned and centered at the focal point of the antennas at 250 mm distance. The MUT is attached in contact to the back of the PMMA slab for characterization. For calibration of material measurements in the reflectometry setup, the reflection of a flat metal sheet is used. To correctly position the reflector, it is brought in contact with the back interface of the PMMA holder, before the holder is removed. This way, the metal reflector is aligned in angle to the holder surface. The reflection from the metal reflector is recorded as reference measurement, before the PMMA holder is mounted back to its initial position. A second reference measurement is recorded from the reflection of the empty PMMA

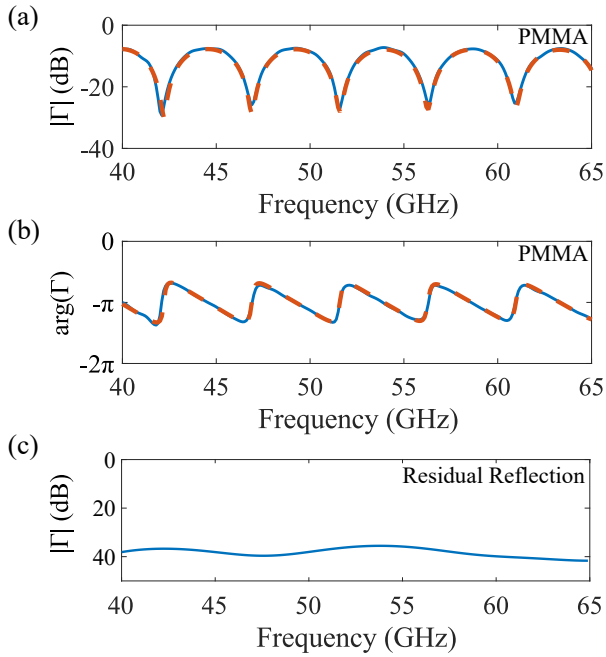

Figure 5.5: (a) Amplitude of the measured and fitted reflection coefficient of PMMA. (b) Phase of the measured and fitted reflection coefficient of PMMA. (c) Residual reflection after de-embedding the PMMA holder. The amplitude gives an estimate of the measurement error in material characterization.

holder. For material characterization, a MUT is brought in contact to the back interface of the PMMA and clamped, if necessary, by a second PMMA plate. For measurements of liquids as MUTs, like the measurement of water in Paper III, a low-density polyethylene (LDPE) bag was used to contain the water. To eliminate multiple reflections in the setup, only 2 ns of the signal around the primary reflection was recorded. This way, higher order reflections were removed by time gating. Since the metal reflector was aligned to the back interface of the PMMA, the primary reflection of the reference measurement from the metal sheet is time shifted, compared to the other measurements. This time shift is corrected by aligning the primary reflection of the metal measurement to the reflection from the PMMA surface and compensating for the propagation loss. The metal reference measurement is then used to normalize the measurements in frequency domain to approximate the reflection coefficient. The time-domain signal of the measurement is shown in Fig. 5.4 (b).

For characterization of the MUT in the reflectometry setup, the reflection from the PMMA holder needs to be de-embedded. Hence, the dielectric permittivity of the PMMA is characterized first. Figure 5.5 (a) and (b) show the measured reflection coefficient. The PMMA holder is modeled as a dielectric slab (cf. the layered dielectric in Section 2.2) and a brute-force fit is performed to minimize the error of the model compared to the measurement. The obtained permittivity value of $\varepsilon_r = 2.55 - 0.013j$ is in line with measurements in transmission [57] and also other measurements reported in literature [65]. The obtained permittivity is then used to de-embed the PMMA holder from the MUT measurements. To estimate the measurement error, the empty PMMA holder is de-embedded from the reference measurement. Ideally, this should result in zero reflection. The residual reflection, shown in Fig. 5.5 (c), gives an estimate of the achievable measurement accuracy for material measurements. The setup can be used to determine the permittivity of different materials. In Paper III, the setup was used to characterize the dispersive materials: water and porcine skin. The characterization of organic tissues, like porcine skin, will be discussed in more detail in Chapter 6.

6

Millimeter-Wave Measurements of Biological Tissue

Electromagnetic radiation in the microwave spectrum is widely used in medical diagnostics and therapy. In hyperthermia cancer therapy, for instance, tumor cells are selectively destroyed by heating the cells with microwave radiation in the megahertz range [66]. Typically, microwave radiation is applied locally by an antenna focused on the tumor region. Phased arrays can be used to reach a maximum field density at the location of deeper tumors, while limiting the heating of surrounding healthy tissue [67]. Heating of the biological tissue is caused by absorption of electromagnetic waves. Other applications use lower field intensities to avoid heating of the tissue. Microwave tomography, for instance, makes use of material contrasts in the tissue to generate images of the inside of the material. The most widely spread microwave imaging technique is magnetic resonance imaging (MRI), using the magnetic material properties. However, also dielectric microwave tomography, for example for the diagnosis of breast cancer, has been proposed [68–72]. Absorption of the tissue, as well as transmission and reflection properties, are in general material and frequency dependent. Imaging systems using millimeter-wave (mm-wave) radiation enable unprecedented resolution, though penetration depth for organic materials is limited. This chapter will give an overview over the interaction of microwave and mm-wave radiation with biological tissue.

6.1 DIELECTRIC PROPERTIES OF BIOLOGIC TISSUES

Predicting the permittivity of biologic tissue is a challenging task due to the variety of materials and the inhomogeneous composition. Most commonly, the permittivity is described by fitting a permittivity model from measurements. An overview of different permittivity models for biological tissue is

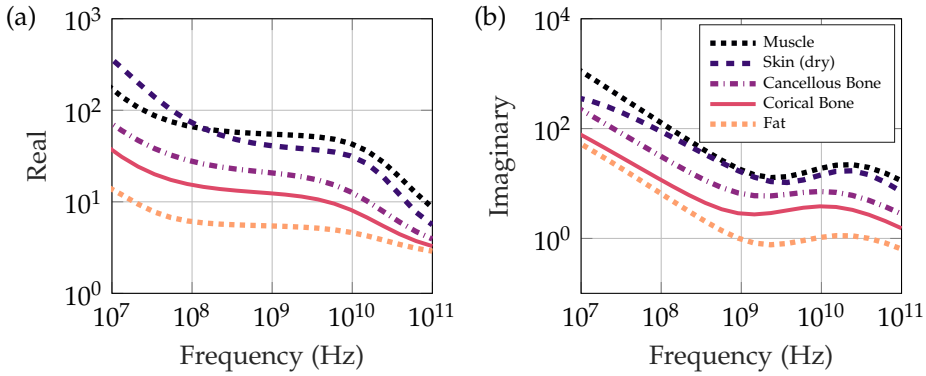

Figure 6.1: Modeled real part (a) and imaginary part (b) of the dielectric permittivity of selected human tissue materials. The model is based on a multi-pole Cole-Cole model by Gabriel *et al.* [73]

Table 6.1: Common Permittivity Models for Organic Tissue

Model	Equation
Constant Permittivity	$\varepsilon_r = \varepsilon' + j\varepsilon''$
Debye [74]	$\varepsilon_r = \varepsilon_\infty + \sum_n \frac{\varepsilon_\infty - \varepsilon_{s,n}}{1+j\omega\tau_n}$
Cole-Cole [75]	$\varepsilon_r = \varepsilon_\infty + \sum_n \frac{\varepsilon_\infty - \varepsilon_{s,n}}{1+(j\omega\tau_n)^{(1-\alpha_n)}}$

given in Table 6.1. For some applications, the permittivity is approximated by a single complex value. This simplification, however, is only applicable for narrow-band signals due to the strong frequency dependence of the materials. Due to the high water content, the dispersion of many biologic tissues shows similar behavior as water. The Debye model, widely used for modeling the permittivity of water, has been shown to represent muscular tissue [76] and is widely used for numerical modeling of tissue with the finite difference time domain (FDTD) method [77,78]. To fit the permittivity over a frequency range of several orders of magnitude, multiple Debye resonance terms are commonly used [76]. Not all of the water in biological tissues is present in its free form. Rather, part of the water is bound for example by nucleic acid and proteins [79,80]. This causes a shift and a broadening of the resonances compared to the Debye resonances of water. Cole and Cole proposed a modified version of the Debye resonance model to take this broadening into account [75]. Additionally to these resonance terms, often a conductivity term $\frac{\sigma}{j\omega\epsilon_0}$ is also included in the model [73,76]. This term describes the static ionic conductivity in the tissue.

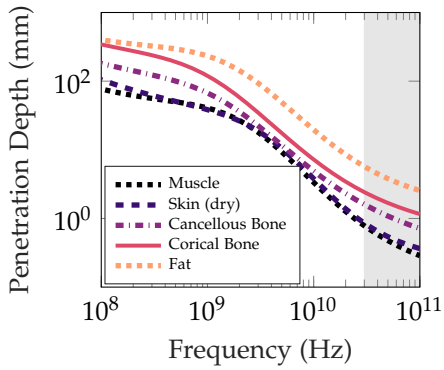

Figure 6.2: The depth of penetration of electromagnetic radiation into different organic tissues. The lower mm-wave range is shown grey. Muscle and skin show the highest attenuation and, therefore, the smallest penetration depth.

Differences in density, water content, and the amount of bound water lead to significant differences in the properties of organic tissues. Figure 6.1 shows the modeled dielectric permittivity of several human tissue materials [73]. Values for both real and imaginary part are spread over several orders of magnitude. Tissue with a high water content, like muscle tissue or skin, show higher values, whereas other tissues with mainly solid components, like the bone tissue show lower values. Attempts have been made to connect the water content of tissues directly to the tissue permittivity by using Maxwell-Garnett mixing theory [81–83]. Also, bottom-up modeling approaches have been proposed to describe the dielectric properties based on material composition and morphology [84–86]. In these approaches a priori knowledge of the composition and morphology of the specific sample are required. For the practical evaluation of organic tissue, this information is often hard to obtain. Hence, the top-down modeling approach, determining effective material parameters, is often preferred.

6.2 REFLECTION OF HUMAN SKIN IN THE MILLIMETER-WAVE RANGE

The penetration depth of electromagnetic waves into a material is dependent on its dielectric permittivity. A significant part of incident electromagnetic radiation is reflected at the surface and material losses lead to an exponential decay of the amplitude of the electromagnetic field in the material (cf. Section 2.2). Therefore, the dielectric properties of biological tissues, described in the previous section, determine how deep an incident electromagnetic wave penetrates in the tissue. Typically, the penetration depth of electromagnetic

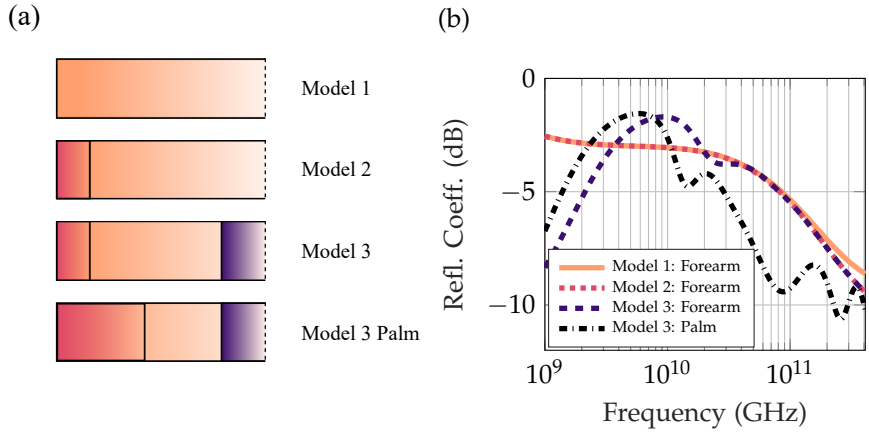

Figure 6.3: (a) Different Skin Models [88]. Model 1 describes the material with homogeneous permittivity. Model 2 adds a layer on the surface to represent the lower water content of the stratum corneum. For skin at the palm of the hand, this top layer is thicker. Model 3 adds a deeper layer to represent the fat layer in the dermis. (b) Calculated reflection coefficients for the described models based on measured data in [88].

fields is given by the depth where the field strength has decayed to 36.8 %. Figure 6.2 describes the penetration depth of some biological tissues in dependence of the frequency. Whereas in the megahertz and lower gigahertz range the field penetrates several tens of centimeters, the field in the mm-wave range is attenuated strongly and penetrates only millimeters or less, depending on the material. For example for skin, the penetration depth is only 0.47 mm at 60 GHz. Since the skin layer is thicker than this, penetration to deeper tissues can be neglected for mm-wave radiation with normal power levels. On the other hand, the high spatial resolution of mm-wave systems might enable resolving features in the skin itself. One application would, for instance, be to resolve cancerous tissue in the skin. For tumors in breast tissue, it has been demonstrated that cancerous cells exhibit a higher water content and, therefore, also a different dielectric permittivity compared to healthy tissue [87].

The inhomogeneous material composition, in particular differences in water content, influence the permittivity of organic tissues. Anatomically, skin tissue is described by a layer structure with different cell types and morphologies. The epidermis, the top layer of the skin, consists mainly of kreatinocyte cells in different stages of their life cycle. Towards the surface, cells die off and have lost nearly all their cytoplasm and cytoplasmic organelles. Cells therefore have a very low water content and are mainly formed by lipids and cross-

linked remains of the dead cell. This region is called stratum corneum [89,90]. At deeper layers of the epidermis and the subjacent dermis, the cells typically have a higher water content. The deepest skin layer, the hypodermis, contains a varying number of fat cells, depending on the position of the body and the nutrition of the subject [89, 90]. Compared to other organic tissues, fat has a lower permittivity [73] (cf. Fig. 6.4). It has been demonstrated that for broadband measurements of the skin in the mm-wave and terahertz range the layered structure of the skin has to be taken into account in certain cases [88, 91]. Figure 6.3 (a) gives an overview of different skin models based on the reflection of layered dielectric media (cf. Equation (2.13)) [88]. The simulated reflection coefficient of the skin, according to these models, is shown in Fig. 6.3 (b). Model 1 simulates the behavior of the skin as semi-infinite homogeneous material with Debye model permittivity. Adding a layer with low dispersion at the surface changes the behavior at high frequencies (cf. Model 2). For Model 3, the skin is simulated as a finite layer with a semi-infinite fat layer in the back. This improves the low frequency fit of the permittivity. As reported by Alekseev *et al.* [88], measurements on the palm of the hand, where the stratum corneum of the skin is very thick, have to be represented by a multilayer model to be fitted accurately. In fact, it can be seen from the simulations in Fig. 6.3 (b) that the reflection coefficient looks significantly different to the forearm skin. Resonances appear in the reflection of the skin at 14.5 GHz, 85 GHz, and 260 GHz. The resonance frequencies are, however, outside of the measurement range, from 37 to 74 GHz, evaluated in the original paper [88]. Resonances might, therefore, occur at other frequencies or not be as clearly defined. Indeed, in broadband measurements of palm skin in the frequency range from 0.5 and 110 GHz, no resonance is visible at high frequencies [92]. Measurements at even higher frequencies are required to investigate the properties and thickness of the stratum corneum.

6.3 MILLIMETER-WAVE SKIN PERMITTIVITY MEASUREMENTS

Mm-wave measurements have been proposed for clinical applications like cancer diagnosis [71,72] and the imaging of skin anomalies like wounds and other injuries [72,93,94]. Commonly, frequency-domain techniques are used, since linear measurements with high sensitivity are possible. For laboratory measurements a vector network analyzer (VNA) has become the standard instrument. In practical applications, however, it might not always be feasible to use high-precision laboratory equipment due to cost or power consumption. In this thesis, pulsed radar systems are investigated as alternative. With this technology, low-cost and low-power medical imaging systems might be

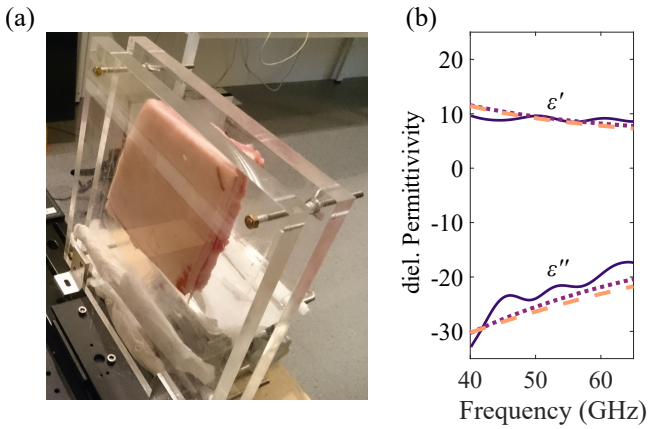

Figure 6.4: a) A photograph of the sample holder with porcine skin as material under test (MUT). To hold the sample and planarize its surface, the sample is clamped between two PMMA sheets. b) The measured dielectric permittivity (solid) and the Debye model fit (dotted) of the porcine skin. Values are similar to the values of human skin on the forearm (dashed) reported in [88].

implemented in the future.

As a first study, the permittivity measurement setup, described in Section 5.2, was used to characterize biological tissues. In Paper III, the measurement of skin from the pork belly has been presented. For these measurements, the skin sample was clamped in a fixture at 250 mm distance from the antennas. The fixture, depicted in Fig 6.4 (a), consisted of two 300x300x20 mm poly(methyl methacrylate) (PMMA) sheets with four screws in the corners to press them together. By applying moderate pressure with the screws, the surface of the skin was planarized. To illuminate the sample homogeneously with the antennas, relatively large samples (approximately 150x150 mm) are required. This limits the use of the measurement setup to ex-vivo measurements of large skin pieces. A de-embedding procedure was used to obtain the frequency dependent reflection coefficient of the skin sample. A brute-force optimization was then applied to find the Debye parameters of the skin. A single order Debye model is used for simplicity. The obtained permittivity, in comparison to values for human skin from literature [88], is shown in Fig. 6.4 (b). Since the stratum corneum in the porcine skin sample is thin, the homogeneous skin model (Model 1) is sufficient for modeling the material in the characterized frequency range.

Pulsed measurements enable evaluation of the dielectric material properties directly in time domain. For measurements in transmission, it has been shown that pulse amplitude and delay are directly related to the complex material

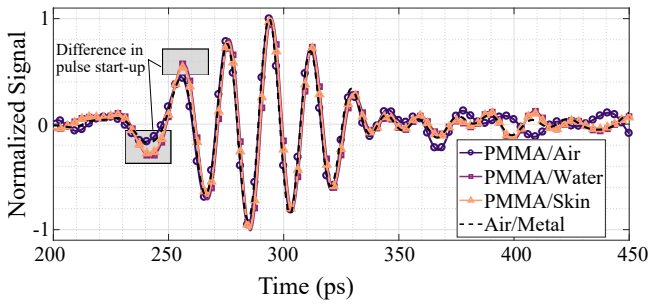

Figure 6.5: The reflection of mm-wave pulses at different material interfaces, normalized to it's maximum. The reflection of the Air/Metal interface is assumed to be the undistorted incident signal. The reflection on the PMMA/Air interface is basically undistorted compared to the reference. Reflections from the PMMA/Water and PMMA/Skin interface are clearly distorted, resulting in a difference in the pulse start-up

permittivity and sample thickness [57]. The relation to the material reflection can be considered similarly. The amplitude of the reflected pulse is related to the frequency averaged permittivity contrast of the materials at an interface. Material interfaces are separated by a time delay. For layers thicker than the resolution of the radar (aproximately 1.2 cm for the waveforms used), it is, therefore, straight forward to de-embed multiple layers. Pulses reflected on dispersive materials are distorted. In Paper IV, it was demonstrated that pulse distortion is directly related to the dispersive properties of the material. A stronger frequency dependence of the reflection coefficient results in a stronger pulse distortion. Pulses from reflection measurements on metal, PMMA, porcine skin tissue, and water are shown in Fig. 6.5. The pulses are clearly distorted and exhibit a difference in the start-up behavior. The distortion mainly originates from a weighting of side-lobes of the frequency spectrum of the pulse. For the measurement of the distortion, it is, therefore, important to resolve the reflection with sufficient signal-to-noise ratio (SNR). To evaluate the impact of the distortion on practical radar applications with matched filter processing, the fidelity factor can be used. The fidelity factor gives a measure for the similarity of the reflected pulse in comparison to the incident pulse [95]. It is defined as:

$$F = \max_{\tau} \left(\int \frac{p(t) r(t+\tau)}{E_{\mathrm{p}} E_{\mathrm{r}}} dt \right), \tag{6.1}$$

where E_{r} and E_{p} is the energy of the reflected pulse, $r(t)$, and the incident pulse, $p(t)$, respectively. The reflections on skin and water both have a fidelity factor of approximately 99 %. For radar measurement of biological targets,

matched filter processing can, therefore, be used without significant amplitude loss. For practical applications in radar systems, the pulse distortion has only negligible influence.

The results demonstrate that the RTD-MOSFET pulse generator is suitable for obtaining qualitative as well as quantitative data for the material properties of organic tissues. This raises interest in a variety of new measurements with this technique. A contrast between different skin samples, distinguishable in layer thicknesses or water content, should be visible. Combining the presented techniques with synthetic aperture radar (SAR) measurements would introduce spatial resolution to distinguish materials. This also would enable measuring smaller samples and in-vivo measurements. Some first investigation of SAR with the RTD-MOSFET pulse generator was done in the PhD-thesis by Iman Vakili [54] and the master thesis by Rickard Ståhl and Oscar Gylling [96], co-supervised by the author of this thesis. Scaling measurements to higher frequencies would help to increase spatial resolution. According to the previously described skin models, resonances due to the layer structure occur at higher frequencies. This might open up several interesting applications, for instance, in medical imaging. The RTD-MOSFET pulse generator offers a promising way to implement these systems in a power efficient way.

7

Gesture Recognition

The recent development of automotive radar systems has led to affordable millimeter-wave (mm-wave) radar systems on the market. This makes radar available for many novel niche applications. Gesture recognition is a promising new field where radar sensors might revolutionize existing technology. Radar sensors can operate completely touchless and no additional controller is required. Compared to gesture recognition systems based on machine vision [97], radar systems are insensitive to lighting conditions and other environmental influences like dust.

In recent years, radar based gesture recognition has been demonstrated in many studies. An overview of radar-based gesture recognition, presented in literature, is given in Appendix C. By far the most common approach is frequency modulated continuous wave (FMCW) radar. Pulse-based mm-wave radar systems for gesture recognition have been proposed [98] but have not been demonstrated previously. The first practical demonstration is presented in Paper VI. This chapter will give an overview over mm-wave pulse radar measurements of the human hand. Implementing gesture recognition systems with the pulse-based radar transmitters, investigated in this thesis, might enable energy efficient radar systems by duty cycling the mm-wave parts of the system.

7.1 GESTURE SIGNAL DETECTION WITH WIDEBAND PULSES

For the design of a low-power gesture recognition systems, it is critical to have enough signal-to-noise ratio (SNR) to be able to resolve scattering features of the human hand. As part of the work presented in Paper V, the link budget for pulses scattered from the hand in three different postures, the flat hand, the fist, and a hand with raised index finger was investigated. A photograph

of these hand postures is shown in Fig. 7.1 (a). The link budget of a radar system is given by the radar range equation (2.2). To avoid uncertainty by estimating unknown parameters, the link budget is obtained by comparing the link to the measurement of a reference object with known parameters. From this measurement, the strength of the signal in a reference distance can be determined. Measurements were taken using a modified version of the reflectometry setup, described in Chapter 5. A LeCroy WaveExpert 100H sampling oscilloscope was used as receiver. A flat metal sheet was used as reference object. The radar cross section (RCS) of this sheet can be derived as $\sigma_{\text{ref}} = \pi R^2$, assuming an infinitely extended mirror. The RCS of any target object, σ_{obj}, at R can then be obtained by

$$\sigma_{\text{obj}} = \frac{P_{\text{obj}}}{P_{\text{ref}}} \cdot \sigma_{\text{ref}} \tag{7.1}$$

where P_{obj} and P_{ref} are the received power level from the target object and the reference, respectively.

An important aspect of the link budget is the noise level of the receiver. The dominating noise in the microwave and mm-wave frequency range is thermal noise. The thermal noise is modeled by a additive white Gaussian stochastic process, having a constant power spectral density (PSD), $S_{xx}(\omega) = N_0$, at all frequencies [2]. For a signal in a measurement system, the noise power is given by the integral of $S_{xx}(\omega)$ over the receiver bandwidth, B. For signal acquisition with the sampling oscilloscope, B is constant and each sample is affected by random noise. This noise can be expressed by a root mean square (RMS) voltage deviation, V_{RMS}, obtained from the data sheet of the instrument [99]. In that case, the noise spectral density can be derived as

$$S_{xx}(\omega) = \frac{V_{\text{RMS}}^2}{f_{\text{s}} N_{\text{avg}}}, \tag{7.2}$$

where N_{avg} is the number of averages and f_{s} is the equivalent sampling frequency. The requirement for signal detection is that the signal energy significantly exceeds the noise energy during the measurement interval. The energy of the transmitted pulses can be increased by transmitting longer pulses or using modulated pulses, as discussed in Chapter 4. For the measurements in Paper V a phase-correlated duo-binary waveform was applied. In the measurements, the signal from the reference metal reflector with a RCS $\sigma = -7$ dBsm was 30 dB over the noise floor. Therefore, objects down to a SNR of approximately -37 dBsm could be detected. The result of the frequency averaged RCS for the three hand postures is shown in Fig. 7.1 (b). The RCS of the flat hand was measured as -29.8 dBsm and the RCS of the fist as -35.1 dBsm. In the posture with raised index finger, the RCS was

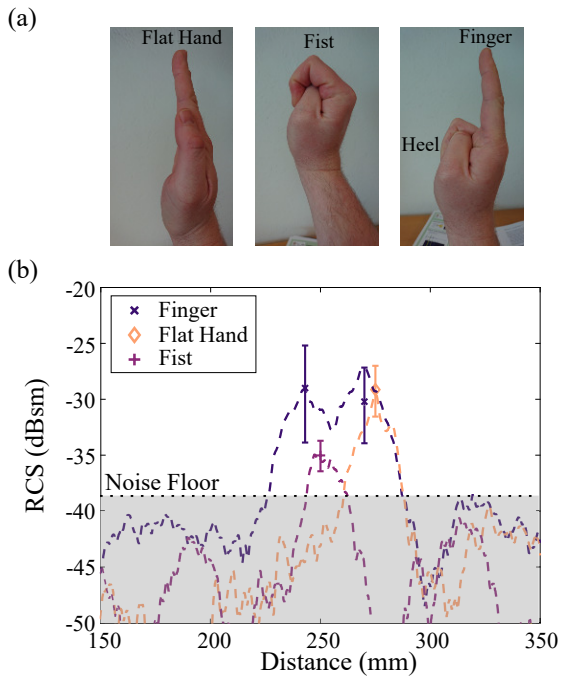

Figure 7.1: (a) The three examined hand postures: a flat hand, a fist and a hand with raised index finger (b) The measured frequency averaged radar cross-section in dependence of distance.

determined as -29.5 dBsm for the heel and -30.6 dBsm for the index finger. The values are in the same range of values in E-band reported by [100].

For measurements with a real-time down-conversion receiver (cf. Section 5.1), the requirements on the link budget are similar. The horn antennas have slightly more gain than the leaky-lens antennas in the measurements. The peak signal level at the receiver is, therefore, slightly higher than in the previous case. The performance of the receiver is limited by the properties of the down-conversion mixer. The mixer has a nominal bandwidth of 9 GHz and a conversion loss of 6.5 dB. The noise figure of the mixer is not specified, but can be approximated to be the same as the conversion loss. Adding an additional low noise amplifier (LNA) at the receiver would reduce the system noise figure. The HXI HLNAV-383 LNA has a nominal noise figure of 5.2 dB and a gain of 30 dB. For an optimized system implementation, a LNA with lower noise figure would increase the performance even more. The implementation with the HLNAV-383 was sensitive enough to detect hand gestures of single 600 ps pulses with good SNR. The SNR in the

measurements could be improved further by using the presented duo-binary phase correlated waveforms (see Chapter 4).

7.2 THE GEOMETRY AND MOVEMENTS OF THE HUMAN HAND

Radar-based gesture recognition relies on detecting an electromagnetic wave scattered on the human hand. Bones in the hand are connected by several joints, allowing the hand to perform movements with a total of 21 degrees of freedom [101]. The hand is covered by several groups of muscles and a layer of skin. The electromagnetic properties of the skin were discussed in Chapter 6. The reflection of mm-wave signals is mainly determined by the surface of the skin. Reflections from deeper skin layers, bones, and muscles can be disregarded. All muscles play together to allow the hand to perform complex movements with good precision. The range, speed, and precision of movements can be trained and achieve virtuous levels, for instance when playing a piano. Controlled movements of the hand are supported by sensory feedback from muscles, eyes or the tactile sense [101]. A kinematic model for hand gestures, based on the anatomy, has been presented in literature [102]. Since the goal with hand gestures is to provide an intuitive human-machine interface, the choice of simple hand gestures is important. Hand gestures with sensory feedback, as for instance proposed in [1], help to make gestures more precise and intuitive.

The radar properties of the chosen gestures are another important aspect for the design of a gesture-based control system. To classify the gestures reliably, their radar signatures should be significantly different. In general, this is dependent on the exact placement of radar transmitters and receivers relative to the hand. As shown in Section 7.1 and Paper V, the RCS is dependent on the posture of the hand. Specular reflections from normal incidence of the radar signal during the gesture might cause high signal levels in some instances, but might not occur reliably during each repetition when the angle is slightly different. Additionally, the geometry of the hand transforms significantly when performing a gesture. For a rigorous evaluation of the electromagnetic scattering, each posture should be evaluated individually, which makes this require a lot of computational power to simulate. A simplified attempt to model the scattering of hand gestures can be found in the master thesis by Erik Ingemarsson [103], co-supervised by the author of this thesis.

In another approach, the signal of different hand gestures was evaluated experimentally. The coherent down-conversion setup (cf. Chapter 5) was used to examine hand gestures on different movement scales. The 12 hand gestures, including large scale hand movements as well as finger movements, used are shown in Fig. 7.2. Since the radar system used has only a single

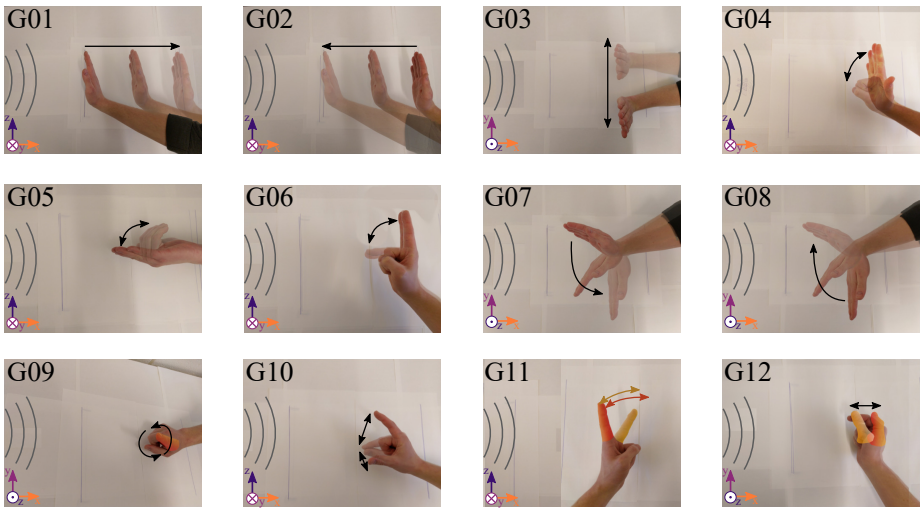

Figure 7.2: Hand Gestures: (G01) Backward hand movement, (G02) Forward hand movement, (G03) Hand moving right and left, (G04) Hand transitioning from flat hand to fist and back, (G05) Flat hand closing and opening, (G06) Raised index finger folding back and forth, (G07) Hand rotating leftwards around the wrist, (G08) Hand rotating rightwards around the wrist, (G09) Finger spinning counter clockwise, (G10) Fingers simulating push button press, (G11) Two raised fingers alternating back and forth, (G12) Fingers simulating slider button.

receiver and transmitter, it is not possible to resolve the angle. Movements perpendicular to the propagation direction, however, also cause a change of the distance to the target. Cross range movements can, therefore, either be detected by a high spatial resolution or by the Doppler caused by the movement profile. The results of the real time gesture measurements are summarized in Paper VI, which contains the first demonstration of hand gesture measurement and classification with a mm-wave pulsed radar. These results were obtained in the scope of the master thesis by Anton Evertsson and Hannes Dahlberg [104], co-supervised by the author of this thesis. The students handled the recording of the training data and implemented the classification algorithm. Details about the acquisition and signal processing of pulsed radar data will be discussed in the next section.

7.3 GESTURE SIGNAL PROCESSING AND CLASSIFICATION

For the acquisition of hand gestures with a pulsed radar system, a fast receiver is essential. For a first evaluation of pulsed measurements in the laboratory, the down-conversion setup, presented in Chapter 5, was used. This section will give an overview of the principle acquisition and signal processing approaches for gesture measurements.

In a pulsed radar system, the momentary posture of the hand is recorded by a short waveform. Movements are acquired by repeating this measurement at a fixed pulse repetition interval (PRI). This PRI should be set according to the maximum expected movement speed. Using too low PRI will cause aliasing of the Doppler frequencies and movement speeds cannot be resolved without ambiguity. As an example, a 60 GHz radar with a PRI of 1 ms can resolve movement speeds up to 125 cm/s. This should be enough for the main movements of hand gestures. The PRI also sets the unambiguous range of the radar system. Gestures are typically performed close to the radar and, therefore, the unambiguous range is uncritical. On the contrary, it is sufficient when the receiver is only active in a short time window after the pulse transmission. The advantage of this is twofold. One one hand, background signals occurring at different delays can be gated out, on the other hand, the interval between signal acquisition is large enough to duty cycle the radar system. Typically, gesture recognition systems operate at short ranges. Assuming a maximum operation range of 1 m, all echoes will be received within a delay of 6.67 ns. Additionally, the length of the waveform should be taken into account. The presented phase-correlated duo-binary waveforms, for instance, have a duration below 2.3 ns. Hence, an acquisition time in the order of 10 ns in each PRI should be sufficient. For the rest of the PRI, the radar system can be put in a sleep state. For a PRI of 10 ms, the resulting duty cycle is $1 : 10^5$. With the right system design, gesture recognition radars with very low power consumption should be feasible.

In literature, pulse-Doppler processing (cf. Fig. 2.2) is widely used for the analysis of gesture data. The micro-Doppler signatures of the observed gestures are calculated by partitioning the range-time signal in smaller processing interval and taking a Fourier transform in slow-time direction. The micro-Doppler signatures contain the average speed of movements in each partition interval. With the pulsed radar used in this thesis, the maximum Doppler is limited by the acquisition rate of the measurement equipment. With the coherent down-conversion setup, as described in Chapter 5, PRIs of 7.1 ms can be achieved reliably. In principle pulse-Doppler processing can still be used but movements faster than 17.5 cm/s will lead to ambiguous speeds. Figure 7.3 demonstrates the range-time data of an exemplary gesture and pulse-Doppler images for this gesture. In the range-time profile the backward

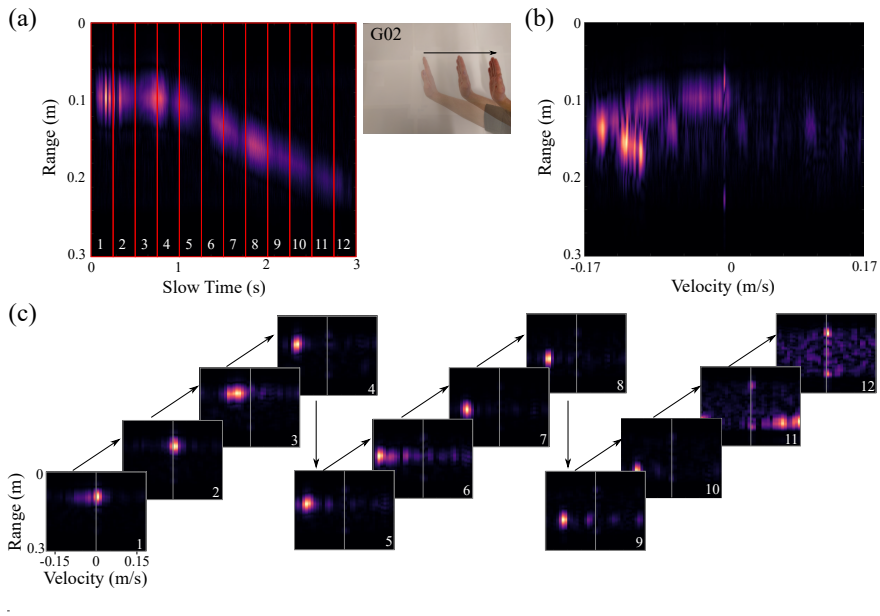

Figure 7.3: (a) Millimeter-wave pulsed radar measurement of a hand moving away from the radar (G02). The movement profile can be clearly seen in the range-time plot acquired by the radar. (b) Range-Doppler profile for the full 3 s movement. This representation gives the high Doppler resolution, but the temporal information of the movement is lost. (c) Range-Doppler images obtained by segmented pulse-Doppler processing of the radar data. Each image contains the average range and velocity in a 250 ms interval.

movement of the hand can be clearly seen as an object with increasing distance over time. This can be seen as negative speeds in the range-Doppler images. In the range-Doppler over the full 3 s interval, the Doppler signatures are smeared out, since the movement is accelerating and decelerating during the observation interval. For the segmented range-Doppler images, the instantaneous speed and position can be estimated.

Radar reflections from hand gestures can be processed with modern classification techniques, like deep neural networks. In literature, this has been demonstrated for FMCW radar [105–109]. Paper VI presents the first demonstration of gesture recognition using mm-wave pulsed radar. Since pulse-Doppler images might show ambiguity in Doppler, direct classification of range-time data is performed. It is demonstrated that standard image recognition techniques can be used to directly classify the data, without the need of pulse-Doppler processing. Transfer learning allowed a reliable classification after training with a relatively small data set. The training set

contained 108 measurements of each of the 12 hand gestures (cf. Fig. 7.2). A recognition accuracy of 98.6 % was achieved by using a convolutional neural network (CNN) on the range-time plots of the gestures. The training was performed by transfer learning with ResNet50 [110]. This network is a deep residual neural network, pre-trained with the ImageNet database [111]. It has been shown that the first layers of CNNs recognize high level features in images [112]. Because of this, using networks pre-trained with completely unrelated data still have a benefit. However, most of the remaining pre-training is unnecessary and a more efficient network for the recognition of hand gestures might be developed. Work towards more efficient gesture classification approaches can be found in the master thesis by Anton Evertsson and Hannes Dahlberg [104].

8

Conclusions and Outlook

In this thesis, various aspects of the development of pulsed millimeter-wave (mm-wave) radar systems for novel applications were investigated. The first part introduced an efficient implementation of a radar transmitter. A radar pulse generator was fabricated in-house using a RTD-MOSFET oscillator. The contact resistance in this fabrication process was optimized. The simple circuit architecture enables efficient generation of mm-wave pulses in the 60 GHz band. Pulses are generated directly at the mm-wave frequency and, therefore, a continuously running mm-wave oscillator can be avoided. For this pulse generator, a modulation scheme was developed to increase the energy of the transmitted waveform without reduction of the spatial resolution.

In the second part of the thesis, measurements and applications using pulsed radar were explored. A laboratory setup for radar measurements was developed and optimized for different use cases. In a free-space material characterization setup, quantitative data of the material parameters can be obtained, as demonstrated for instance by measurements of porcine skin. Further, qualitative analysis of the material reflection is also possible by looking at the reflected pulse and its distortion directly in time domain. Using this method, material classification can be implemented. In further measurements, the application of the RTD-MOSFET for gesture recognition has been presented. This experiment is the first demonstration of mm-wave gesture recognition with a pulsed radar.

In future work, the pulsed radar system might be improved in several ways. The techniques and measurements could be transfered to an integrated radar system. An integrated pulse transmitter has already been presented in prior work [113]. When using an integrated transmitter, coupling losses to the antennas can be avoided and, therefore, a higher transmitted power can be achieved. In principle, the phase-correlated duo-binary modulation technique

should also be applicable for the integrated pulse generators. However, the impact of the limited bandwidth of the transmitter on the modulated waveforms should be investigated.

Another important aspect of an integrated implementation is the receiver. Different receiver concepts are feasible and future research should focus on an energy efficient implementation. Savings in power consumption due to duty cycled waveforms should be demonstrated. Implementing a system with multiple transmitters and receivers in a multiple-input multiple-output (MIMO) system would allow to resolve targets in angle. Implementation of MIMO systems might be aided by the presented phase-correlated duo-binary modulation technique. Finding sequences with low cross-correlation would offer a way to distinguish signals from different transmitters simultaneously. In the presented gesture recognition measurements, the angular resolution would provide an additional classification feature.

RTD-MOSFET technology is a promising way to generate signals at even higher frequency. Resonant-tunneling diodes (RTDs) can be scaled to frequencies well beyond 1 THz. Integrating a MOSFET enables an efficient way to modulate these circuits. Many applications would benefit from the high available bandwidth at these frequencies. High-data rate communication is one example. Also the measurements, presented in this thesis, can be transfered to higher frequencies. For biomedical measurements, for instance, the layer structure of the skin could be examined. Combining the technique with synthetic aperture radar (SAR), imaging systems that can visualize permittivity contrast would be enabled.

Bibliography

[1] J. Lien, N. Gillian, M. E. Karagozler, P. Amihood, C. Schwesig, E. Olson, H. Raja, and I. Poupyrev, "Soli: Ubiquitous gesture sensing with millimeter wave radar," *ACM Trans. Graph.*, vol. 35, no. 4, pp. 142:1–142:19, Jul. 2016.

[2] M. A. Richards, J. Scheer, W. A. Holm, and W. L. Melvin, *Principles of modern radar - Vol. 1: basic principles*. Citeseer, 2010.

[3] E. F. Knott, J. F. Schaeffer, and M. T. Tulley, *Radar cross section*. SciTech Publishing, 2004.

[4] R. P. Feynman, R. B. Leighton, and M. Sands, *The Feynman Lectures on Physics: Vol 1*. Reading, MA: Addison-Wesley, 1966, ch. 34.

[5] L. Cohen, *Time-frequency analysis*. Prentice hall, 1995.

[6] C. Cook, *Radar signals: An introduction to theory and application*. Academic Press, 1967.

[7] R. H. Khan and D. K. Mitchell, "Waveform analysis for high-frequency FMICW radar," *IEE Proc. F - Radar and Signal Process.*, vol. 138, no. 5, pp. 411–419, Oct 1991.

[8] S. J. Orfanidis, *Electromagnetic waves and antennas*. New Brunswick, NJ: Rutgers University, 2002.

[9] R. Izumi, S. Suzuki, and M. Asada, "1.98 THz resonant-tunneling-diode oscillator with reduced conduction loss by thick antenna electrode," in *42nd Int. Conf. Infrared, Millimeter, and Terahertz Waves (IRMMW-THz)*, Aug 2017, pp. 1–2.

[10] L. Ohlsson, "Compact and efficient millimetre-wave circuits for wide-band applications," Ph.D. dissertation, Department of Electrical and Information Technology, 2015.

[11] M. Ärlelid, "Millimeter-wave impulse radio," Ph.D. dissertation, Lund University, 2012.

[12] M. Egard, "Electron tunneling and field-effect devices in mm-wave circuits," Ph.D. dissertation, Lund University, 2012.

[13] J. P. Sun, G. Haddad, P. Mazumder, and J. Schulman, "Resonant tunneling diodes: models and properties," *Proc. IEEE*, vol. 86, no. 4, pp. 641–660, Apr 1998.

[14] G. Gonzalez, *Microwave transistor amplifiers: analysis and design.* Englewood Cliffs, N.J.: Prentice-Hall, 1984.

[15] R. Lake and Junjie Yang, "A physics based model for the RTD quantum capacitance," *IEEE Trans. Electron Devices*, vol. 50, no. 3, pp. 785–789, March 2003.

[16] L. Wang, J. M. L. Figueiredo, C. Ironside, and E. Wasige, "DC characterization of tunnel diodes under stable non-oscillatory circuit conditions," *IEEE Trans. Electron Devices*, vol. 58, no. 2, pp. 343–347, Feb 2011.

[17] L. Wang and E. Wasige, "A design procedure for tunnel diode microwave oscillators," in *Int. Conf. Microw. Millimeter Wave Technol. (ICMMT)*, vol. 2, April 2008, pp. 832–834.

[18] A. Al-Khalidi, K. Alharbi, J. Wang, and E. Wasige, "A compact terahertz source technology for automotive radar and other applications," in *19th Int. Radar Symp. (IRS)*, June 2018, pp. 1–6.

[19] M. Asada, S. Suzuki, and N. Kishimoto, "Resonant tunneling diodes for sub-terahertz and terahertz oscillators," *Jpn. J. Appl. Phys*, vol. 47, no. 6R, p. 4375, 2008.

[20] T. Maekawa, H. Kanaya, S. Suzuki, and M. Asada, "Oscillation up to 1.92 THz in resonant tunneling diode by reduced conduction loss," *Appl. Phys. Express*, vol. 9, no. 2, p. 024101, jan 2016.

[21] M. Egard, M. Arlelid, E. Lind, G. Astromskas, and L. . Wernersson, "20 GHz wavelet generator using a gated tunnel diode," *IEEE Microw. Wireless Compon. Lett.*, vol. 19, no. 6, pp. 386–388, June 2009.

[22] M. Arlelid, M. Egard, E. Lind, and L. E. Wernersson, "Coherent V-band pulse generator for impulse radio BPSK," *IEEE Microw. Wireless Compon. Lett.*, vol. 20, no. 7, pp. 414–416, July 2010.

[23] M. Egard, M. Arlelid, L. Ohlsson, B. Borg, E. Lind, and L. E. Wernersson, "$In_{0.53}Ga_{0.47}As$ RTD-MOSFET millimeter-wave wavelet generator," *IEEE Electron Device Lett.*, vol. 33, no. 7, pp. 970–972, July 2012.

[24] K. Ishigaki, M. Shiraishi, S. Suzuki, M. Asada, N. Nishiyama, and S. Arai, "Direct intensity modulation and wireless data transmission characteristics of terahertz-oscillating resonant tunnelling diodes," *Electron. Lett.*, vol. 48, no. 10, pp. 582–583, May 2012.

[25] J. Wang, A. Al-Khalidi, L. Wang, R. Morariu, A. Ofiare, and E. Wasige, "15-Gb/s 50-cm wireless link using a high-power compact III-V 84-GHz transmitter," *IEEE Trans. Microw. Theory Techn.*, vol. 66, no. 11, pp. 4698–4705, Nov 2018.

[26] L. Ohlsson, P. Fay, and L.-E. Wernersson, "Picosecond dynamics in a millimetre-wave RTD-MOSFET wavelet generator," *Electron. Lett.*, vol. 51, no. 21, pp. 1671–1673, 2015.

[27] M. Egard, M. Ärlelid, E. Lind, and L. Wernersson, "Bias stabilization of negative differential conductance oscillators operated in pulsed mode," *IEEE Trans. Microw. Theory Techn.*, vol. 59, no. 3, pp. 672–677, March 2011.

[28] C. Chang, Y. Fang, and S. Sze, "Specific contact resistance of metal-semiconductor barriers," *Solid-State Electron.*, vol. 14, no. 7, pp. 541 – 550, 1971.

[29] D. Kim and J. A. del Alamo, "Scalability of sub-100 nm InAs HEMTs on InP substrate for future logic applications," *IEEE Trans. Electron Devices*, vol. 57, no. 7, pp. 1504–1511, July 2010.

[30] J. Yao, Y. Lin, H. Hsu, K. Yang, H. Hsu, S. M. Sze, and E. Y. Chang, "Evaluation of a 100-nm gate length E-Mode InAs high electron mobility transistor with Ti/Pt/Au ohmic contacts and mesa sidewall channel etch for high-speed and low-power logic applications," *IEEE J. Electron Devices Soc.*, vol. 6, pp. 797–802, 2018.

[31] M. Egard, L. Ohlsson, B. M. Borg, F. Lenrick, R. Wallenberg, L. E. Wernersson, and E. Lind, "High transconductance self-aligned gate-last surface channel $In_{0.53}Ga_{0.47}As$ MOSFET," in *IEEE Int. Electron Devices Meeting (IEDM)*, Dec 2011, pp. 13.2.1–13.2.4.

[32] C. B. Zota, F. Lindelow, L. Wernersson, and E. Lind, "InGaAs tri-gate MOSFETs with record on-current," in *IEEE Int. Electron Devices Meeting (IEDM)*, Dec 2016, pp. 3.2.1–3.2.4.

[33] H. H. Wieder, "Surface and interface barriers of $In_xGa_{1-x}As$ binary and ternary alloys," *J. Vac. Science Technol. B*, vol. 21, no. 4, pp. 1915–1919, 2003.

[34] H. Berger, "Models for contacts to planar devices," *Solid-State Electron.*, vol. 15, no. 2, pp. 145 – 158, 1972.

[35] A. M. Crook, E. Lind, Z. Griffith, M. J. W. Rodwell, J. D. Zimmerman, A. C. Gossard, and S. R. Bank, "Low resistance, nonalloyed ohmic contacts to InGaAs," *Appl. Phys. Lett.*, vol. 91, no. 19, pp. –, 2007.

[36] S. Reynolds, B. Floyd, U. Pfeiffer, and T. Zwick, "60 GHz transceiver circuits in SiGe bipolar technology," in *IEEE Int. Solid-State Circuits Conf.*, Feb 2004, pp. 442–538 Vol.1.

[37] B. Razavi, "A 60 GHz CMOS receiver front-end," *IEEE J. Solid-State Circuits*, vol. 41, no. 1, pp. 17–22, Jan 2006.

[38] G. F. Engen, "The six-port reflectometer: An alternative network analyzer," *IEEE Trans. Microw. Theory Techn.*, vol. 25, no. 12, pp. 1075–1080, Dec 1977.

[39] A. Koelpin, F. Lurz, S. Linz, S. Mann, C. Will, and S. Lindner, "Six-port based interferometry for precise radar and sensing applications," *Sensors*, vol. 16, no. 27669246, p. 1556, Sep. 2016.

[40] D. Cabric, M. S. Chen, D. A. Sobel, S. Wang, J. Yang, and R. W. Brodersen, "Novel radio architectures for UWB, 60 GHz, and cognitive wireless systems," *EURASIP J. Wireless Commun. Netw.*, vol. 2006, no. 1, p. 017957, Mar 2006.

[41] R. Okuizumi, Y. Inada, and M. Muraguchi, "RF direct orthogonal phase under-sampling technique for software defined radio," *Electron. Lett.*, vol. 44, no. 18, pp. 1074–1075, August 2008.

[42] K. Norishima, T. Koizumi, M. Motoyoshi, S. Kameda, and N. Suematsu, "Demodulation characteristics of a 20 GHz-band direct RF undersampling receiver," in *Asia-Pacific Microw. Conf. (APMC)*, Dec 2016, pp. 1–3.

[43] N. Yoshino, K. Norishima, M. Motoyoshi, S. Kameda, and N. Suematsu, "A 28 GHz-band direct RF undersampling S/H CMOS IC with 40 dB SNR," in *2018 IEEE International Symposium on Radio-Frequency Integration Technology (RFIT)*, Aug 2018, pp. 1–3.

[44] V. Jain, S. Sundararaman, and P. Heydari, "A 22-29 GHz UWB pulse-radar receiver front-end in 0.18-μm CMOS," *IEEE Trans. Microw. Theory Techn.*, vol. 57, no. 8, pp. 1903–1914, Aug 2009.

[45] C. Tu, B. Liu, and H. Chen, "An analog correlator for ultra-wideband receivers," *EURASIP J. Adv. Signal. Process.*, vol. 2005, no. 3, p. 546896, Mar 2005.

[46] Chunjiang Tu, Boan Liu, and Hongyi Chen, "A CMOS correlator for UWB front-end circuit," in *6th Int. Conf. ASIC*, vol. 1, Oct. 2005, pp. 488–492.

[47] N. Karandikar, S. Jung, S. C. Lee, P. Gui, and Y. Joo, "Design of an analog correlator for 22-29 GHz UWB vehicular radar system using improved high gain multiplier architecture," in *53rd IEEE Int. Midwest Symp. Circuits and Syst.*, Aug 2010, pp. 930–933.

[48] A. G. Stove, "Linear FMCW radar techniques," *IEE Proc. F - Radar and Signal Process.*, vol. 139, no. 5, pp. 343–350, Oct 1992.

[49] D. D. Wentzloff and A. P. Chandrakasan, "Delay-based BPSK for pulsed-UWB communication," in *IEEE Int. Conf. Acoust., Speech, Signal Process. (ICASSP)*, vol. 3, April 2007, pp. III–561–III–564.

[50] A. Lender, "The duobinary technique for high-speed data transmission," *Trans. Am. Inst. Electrical Eng. Part I: Commun. Electron.*, vol. 82, no. 2, pp. 214–218, May 1963.

[51] A. W. Rihaczek, "Radar resolution properties of pulse trains," *Proc. IEEE*, vol. 52, no. 2, pp. 153–164, Feb 1964.

[52] C. P. Kaiteris and W. L. Rubin, "Radar-waveform design for detecting targets in clutter," *Proc. Inst. Electr. Eng.*, vol. 114, no. 6, pp. 696–702, June 1967.

[53] I. Vakili, L. Ohlsson, M. Gustafsson, and L.-E. Wernersson, "Wideband and non-dispersive wavelet transmission using leaky lens antenna," *Electron. Lett.*, vol. 49, no. 5, pp. 321–322, February 2013.

[54] I. Vakili, "Time-domain antenna and scattering analysis for micro- and millimeter-wave applications," Ph.D. dissertation, Lund University, 2015.

[55] M. Afsar, J. Birch, R. Clarke, and G. Chantry, "The measurement of the properties of materials," *Proc. IEEE*, vol. 74, no. 1, pp. 183–199, Jan 1986.

[56] J. Baker-Jarvis, M. D. Janezic, and D. C. Degroot, "High-frequency dielectric measurements," *IEEE Instr. Meas. Mag.*, vol. 13, no. 2, pp. 24–31, April 2010.

[57] I. Vakili, L. Ohlsson, L.-E. Wernersson, and M. Gustafsson, "Time-domain system for millimeter-wave material characterization," *IEEE Trans. Microw. Theory Techn.*, vol. 63, no. 9, pp. 2915–2922, 2015.

[58] D. K. Ghodgaonkar, V. V. Varadan, and V. K. Varadan, "Free-space measurement of complex permittivity and complex permeability of magnetic materials at microwave frequencies," *IEEE Trans. Instrum. Meas.*, vol. 39, no. 2, pp. 387–394, Apr 1990.

[59] M. H. Umari, D. K. Ghodgaonkar, V. V. Varadan, and V. K. Varadan, "A free-space bistatic calibration technique for the measurement of parallel and perpendicular reflection coefficients of planar samples," *IEEE Trans. Instrum. Meas.*, vol. 40, no. 1, pp. 19–24, Feb 1991.

[60] I. Rolfes, "Microwave free space calibration methods," in *Conf. Precision Electromag. Meas. Digest*, June 2004, pp. 72–73.

[61] M. Zhao, J. D. Shea, S. C. Hagness, and D. W. van der Weide, "Calibrated free-space microwave measurements with an ultrawideband reflectometer-antenna system," *IEEE Microw. Wireless Compon. Lett.*, vol. 16, no. 12, pp. 675–677, Dec 2006.

[62] P. G. Bartley and S. B. Begley, "Improved free-space S-parameter calibration," in *IEEE Instr. Meas. Technol. Conf. Proc.*, vol. 1, May 2005, pp. 372–375.

[63] Y. Kato and M. Horibe, "Improvement of transmission/reflection method for permittivity measurement using long fixtures with time-domain analysis approach," *IEEE Trans. Instrum. Meas.*, vol. 66, no. 6, pp. 1201–1207, June 2017.

[64] L. Ohlsson, I. Vakili, D. Sjöberg, and L. E. Wernersson, "Mixed-domain gating algorithm for time-domain characterisation of millimetre-wave antennas," in *47th European Microw. Conf. (EuMC)*, Oct 2017, pp. 256–259.

[65] W. Culshaw and M. Anderson, "Measurement of permittivity and dielectric loss with a millimetre-wave fabry-perot interferometer," *Proc. Inst. Elect. Eng. B - Electron. Commun. Eng*, vol. 109, no. 23, pp. 820–826, 1962.

[66] C. J. Diederich, "Thermal ablation and high-temperature thermal therapy: Overview of technology and clinical implementation," *Int. J. Hyperthermia*, vol. 21, no. 8, pp. 745–753, 2005.

[67] H. I. Vargas, W. C. Dooley, R. A. Gardner, K. D. Gonzalez, R. Venegas, S. H. Heywang-Kobrunner, and A. J. Fenn, "Focused microwave phased array thermotherapy for ablation of early-stage breast cancer: Results of thermal dose escalation," *Ann. Surg. Oncol.*, vol. 11, no. 2, pp. 139–146, Feb 2004.

[68] K. L. Carr, "Microwave radiometry: its importance to the detection of cancer," *IEEE Trans. Microw. Theory Techn.*, vol. 37, no. 12, pp. 1862–1869, Dec 1989.

[69] E. C. Fear, X. Li, S. C. Hagness, and M. A. Stuchly, "Confocal microwave imaging for breast cancer detection: localization of tumors in three dimensions," *IEEE Trans. Biomed Eng.*, vol. 49, no. 8, pp. 812–822, Aug 2002.

[70] F. Topfer and J. Oberhammer, "Millimeter-wave tissue diagnosis: The most promising fields for medical applications," *IEEE Microw. Mag.*, vol. 16, no. 4, pp. 97–113, May 2015.

[71] S. D. Meo, P. F. Espín-López, A. Martellosio, M. Pasian, G. Matrone, M. Bozzi, G. Magenes, A. Mazzanti, L. Perregrini, F. Svelto, P. E. Summers, G. Renne, L. Preda, and M. Bellomi, "On the feasibility of breast cancer imaging systems at millimeter-waves frequencies," *IEEE Trans. Microw. Theory Techn.*, vol. 65, no. 5, pp. 1795–1806, May 2017.

[72] F. Kazemi, F. Mohanna, and J. Ahmadi-Shokouh, "Nondestructive high-resolution microwave imaging of biomaterials and biological tissues," *AEU - Int. J. Electron. and Commun.*, vol. 84, pp. 177 – 185, 2018.

[73] S. Gabriel, R. W. Lau, and C. Gabriel, "The dielectric properties of biological tissues: III. parametric models for the dielectric spectrum of tissues," *Phys. Med. Biol.*, vol. 41, no. 11, p. 2271, 1996.

[74] P. Debye, *Polar Molecules*. The Chemical Catalog Company, 1929.

[75] K. S. Cole and R. H. Cole, "Dispersion and absorption in dielectrics I. alternating current characteristics," *J. Chem. Phys.*, vol. 9, no. 4, pp. 341–351, 1941.

[76] W. Hurt, "Multiterm debye dispersion relations for permittivity of muscle," *IEEE Trans. Biomed. Eng.*, vol. BME-32, no. 1, pp. 60–64, Jan 1985.

[77] A. A. Ijjeh, M. M. Ney, and F. P. Andriulli, "Stability and dispersion analysis of a TLM unified approach for dispersive anisotropic media," *IEEE Trans. Microw. Theory Techn.*, vol. 65, no. 4, pp. 1141–1149, April 2017.

[78] Q. Abbasi, A. Sani, A. Alomainy, and Y. Hao, "Numerical characterization and modeling of subject-specific ultrawideband body-centric radio channels and systems for healthcare applications," *IEEE Trans. Inf. Technol. Biomed*, vol. 16, no. 2, pp. 221–227, March 2012.

[79] K. Walkley, "Bound water in stratum corneum measured by differential scanning calorimetry," *J. Investig. Dermatol.*, vol. 59, no. 3, pp. 225 – 227, 1972.

[80] I. D. Kuntz, T. S. Brassfield, G. D. Law, and G. V. Purcell, "Hydration of macromolecules," *Science*, vol. 163, no. 3873, pp. 1329–1331, 1969.

[81] L. Aamodt, M. Manwaring, and K. Manwaring, "In vivo brain tissue water measurement," in *Proc. 12th IEEE Symp. Computer-Based Med. Syst.*, June 1999, pp. 130–135.

[82] M. J. Schroeder, A. Sadasiva, and R. M. Nelson, "An analysis on the role of water content and state on effective permittivity using mixing formulas," *J. Biomechan. Biomed. Biophys. Eng.*, vol. 2, 2008.

[83] K. R. Foster, J. L. Schepps, R. D. Stoy, and H. P. Schwan, "Dielectric properties of brain tissue between 0.01 and 10 GHz," *Phys. Med. Biol.*, vol. 24, no. 6, pp. 1177–1187, nov 1979.

[84] S. Huclova, D. Erni, and J. Frölich, "Modelling and validation of dielectric properties of human skin in the MHz region focusing on skin layer morphology and material composition," *J. Phys. D: Appl. Phys.*, vol. 45, no. 2, p. 025301, 2012.

[85] J. L. Sebastián, S. Muñoz, M. Sancho, G. Álvarez, and J. M. Miranda, "Electric field distribution and energy absorption in anisotropic and dispersive red blood cells," *Phys. Med. Biol.*, vol. 52, no. 23, pp. 6831–6847, nov 2007.

[86] V. Raicu, T. Saibara, H. Enzan, and A. Irimajiri, "Dielectric properties of rat liver in vivo: analysis by modeling hepatocytes in the tissue architecture," *Bioelectrochem. Bioenerg.*, vol. 47, no. 2, pp. 333 – 342, 1998.

[87] R. M. Woodward, V. P. Wallace, R. J. Pye, B. E. Cole, D. D. Arnone, E. H. Linfield, and M. Pepper, "Terahertz pulse imaging of ex vivo basal cell carcinoma," *J. Investig. Dermatol.*, vol. 120, no. 1, pp. 72 – 78, 2003.

[88] S. Alekseev and M. Ziskin, "Human skin permittivity determined by millimeter wave reflection measurements," *Bioelectromagn.*, vol. 28, no. 5, pp. 331–339, 2007.

[89] J. A. McGrath and J. Uitto, *Anatomy and Organization of Human Skin*. John Wiley & Sons, Ltd, 2010, ch. 3, pp. 1–53.

[90] P. Millington and R. Wilkinson, *The Skin in Depth*, ser. Biological Structure and Function Books. Cambridge University Press, 1983, ch. 3, pp. 48–59.

[91] D. B. Bennett, W. Li, Z. D. Taylor, W. S. Grundfest, and E. R. Brown, "Stratified media model for terahertz reflectometry of the skin," *IEEE Sensors J.*, vol. 11, no. 5, pp. 1253–1262, May 2011.

[92] H. Hwang, J. Yim, J.-W. Cho, C. Cheon, and Y. Kwon, "110 GHz broadband measurement of permittivity on human epidermis using 1 mm coaxial probe," in *IEEE MTT-S Int. Microw. Symp. Digest*, vol. 1, June 2003, pp. 399–402 vol.1.

[93] F. Töpfer, L. Emtestam, and J. Oberhammer, "Long-term monitoring of skin recovery by micromachined microwave near-field probe," *IEEE Microw. Wireless Compon. Lett.*, vol. 27, no. 6, pp. 605–607, June 2017.

[94] F. Kazemi, F. Mohanna, and J. Ahmadi-shokouh, "Microwave reflectometry for noninvasive imaging of skin abnormalities," *Australas. Phys. Eng. Sci. Med.*, vol. 41, no. 4, pp. 881–890, Dec 2018.

[95] D. Lamensdorf and L. Susman, "Baseband-pulse-antenna techniques," *IEEE Antennas Propag, Mag.*, vol. 36, no. 1, pp. 20–30, Feb 1994.

[96] R. Ståhl and O. Gylling, "Short range millimeter-wave inverse synthetic aperture radar imaging," Master's thesis, Lund University, 2018.

[97] B. K. Chakraborty, D. Sarma, M. K. Bhuyan, and K. F. MacDorman, "Review of constraints on vision-based gesture recognition for humanâĂŞcomputer interaction," *IET Comput. Vision*, vol. 12, no. 1, pp. 3–15, 2018.

[98] A. Arbabian, S. Callender, S. Kang, M. Rangwala, and A. M. Niknejad, "A 94 GHz mm-wave-to-baseband pulsed-radar transceiver with applications in imaging and gesture recognition," *IEEE J. Solid-State Circuits*, vol. 48, no. 4, pp. 1055–1071, April 2013.

[99] *LeCroy WaveExpert 100H, Data-Sheet*.

[100] P. Hügler, M. Geiger, and C. Waldschmidt, "RCS measurements of a human hand for radar-based gesture recognition at E-band," in *German Microw. Conf. (GeMiC)*, March 2016, pp. 259–262.

[101] L. A. Jones and S. J. Lederman, *Human hand function*. Oxford University Press, 2006.

[102] S. Cobos, M. Ferre, M. Á. Sánchez-Urán, J. Ortego, and R. Aracil, "Human hand descriptions and gesture recognition for object manipulation," *Comput. Methods Biomech. Biomed. Engin.*, vol. 13, no. 3, pp. 305–317, 2010.

[103] E. Ingemarsson, "Modelling of hand gestures and motions," Master's thesis, Lund University, 2019.

[104] H. Dahlberg and A. Evertsson, "Short range gesture sensing using pulsed millimeter-wave radar," Master's thesis, Lund University, 2019.

[105] K. A. Smith, C. Csech, D. Murdoch, and G. Shaker, "Gesture recognition using mm-wave sensor for human-car interface," *IEEE Sensors Lett.*, vol. 2, no. 2, pp. 1–4, June 2018.

[106] Y. Kim and B. Toomajian, "Hand gesture recognition using micro-doppler signatures with convolutional neural network," *IEEE Access*, vol. 4, pp. 7125–7130, 2016.

[107] S. Ryu, J. Suh, S. Baek, S. Hong, and J. Kim, "Feature-based hand gesture recognition using an FMCW radar and its temporal feature analysis," *IEEE Sensors J.*, vol. 18, no. 18, pp. 7593–7602, Sept 2018.

[108] T. Sakamoto, X. Gao, E. Yavari, A. Rahman, O. Boric-Lubecke, and V. M. Lubecke, "Hand gesture recognition using a radar echo IQ plot and a convolutional neural network," *IEEE Sensors Lett.*, vol. 2, no. 3, pp. 1–4, Sept 2018.

[109] F. K. Wang, M. C. Tang, Y. C. Chiu, and T. S. Horng, "Gesture sensing using retransmitted wireless communication signals based on doppler radar technology," *IEEE Trans. Microw. Theory Techn.*, vol. 63, no. 12, pp. 4592–4602, Dec 2015.

[110] K. He, X. Zhang, S. Ren, and J. Sun, "Deep residual learning for image recognition," *CoRR*, vol. abs/1512.03385, 2015.

[111] J. Deng, W. Dong, R. Socher, L. Li, Kai Li, and Li Fei-Fei, "ImageNet: A large-scale hierarchical image database," in *IEEE Conf. Computer Vision Pattern Recognition*, June 2009, pp. 248–255.

[112] M. D. Zeiler and R. Fergus, "Visualizing and understanding convolutional networks," *CoRR*, vol. abs/1311.2901, 2013.

[113] L. Ohlsson, D. Sjöberg, and L. E. Wernersson, "Codesign of compact III-V millimeter-wave wavelet transmitters with on-chip antennas," *IEEE Trans. Microw. Theory Techn.*, vol. 66, no. 1, pp. 273–279, 2018.

[114] Pu, Gupta, Gollakota, and Patel, "Whole-home gesture recognition using wireless signals," in *Proc. 19th Annual Int. Conf. Mobile Computing & Networking*, 2013, pp. 27–38.

[115] Wan, Li, Li, and Pal, "Gesture recognition for smart home applications using portable radar sensors," in *36th Annual Int. Conf. IEEE Eng. Med. Biol. Soc.*, Aug 2014, pp. 6414–6417.

[116] Zhang, Tao, Huangfu, and Shi, "Doppler-radar based hand gesture recognition system using convolutional neural networks," *Int. Conf. Commun. Signal Process. Syst.*, vol. abs/1711.02254, 2017.

[117] Fan, Ma, Gu, Lv, Chen, Ye, Huangfu, Sun, Li, and Ran, "Wireless hand gesture recognition based on continuous-wave doppler radar sensors," *IEEE Trans. Microw. Theory Techn.*, vol. 64, no. 11, pp. 4012–4020, Nov 2016.

[118] Peng, Li, Muñoz-Ferreras, and Gómez-García, "An FMCW radar sensor for human gesture recognition in the presence of multiple targets," in *1st IEEE MTT-S Int. Microw. Bio Conf. (IMBIOC)*, May 2017, pp. 1–3.

[119] Khan, Leem, and Cho, "Hand-based gesture recognition for vehicular applications using IR-UWB radar." *Sensors*, vol. 17, no. 4, Apr 2017.

[120] Alnujaim, Alali, Khan, and Kim, "Hand gesture recognition using input impedance variation of two antennas with transfer learning," *IEEE Sensors J.*, vol. 18, no. 10, pp. 4129–4135, May 2018.

[121] Molchanov, Gupta, Kim, and Pulli, "Short-range FMCW monopulse radar for hand-gesture sensing," in *IEEE Radar Conf. (RadarCon)*, May 2015, pp. 1491–1496.

[122] Zhang, Tian, and Zhou, "Latern: Dynamic continuous hand gesture recognition using fmcw radar sensor," *IEEE Sensors J.*, vol. 18, no. 8, pp. 3278–3289, April 2018.

[123] Suh, Ryu, Han, Choi, Kim, and Hong, "24 GHz FMCW radar system for real-time hand gesture recognition using LSTM," in *Asia-Pacific Microw. Conf. (APMC)*, Nov 2018, pp. 860–862.

[124] Skaria, Al-Hourani, Lech, and Evans, "Hand-gesture recognition using two-antenna doppler radar with deep convolutional neural networks," *IEEE Sensors J.*, vol. 19, no. 8, pp. 3041–3048, April 2019.

[125] Dekker, Jacobs, Kossen, Kruithof, Huizing, and Geurts, "Gesture recognition with a low power FMCW radar and a deep convolutional neural network," in *European Radar Conf. (EURAD)*, Oct 2017, pp. 163–166.

[126] Li, Zhang, Ritchie, and Griffiths, "Sparsity-driven micro-doppler feature extraction for dynamic hand gesture recognition," *IEEE Trans. Aerosp. Electron. Syst.*, vol. 54, no. 2, pp. 655–665, April 2018.

[127] Patra, Geuer, Munari, and Mähönen, "mm-wave radar based gesture recognition: Development and evaluation of a low-power, low-complexity system," in *Proc. 2nd ACM Workshop Millimeter Wave Netw. Sens. Syst.*, ser. mmNets '18. New York, NY, USA: ACM, 2018, pp. 51–56.

[128] Hazra and Santra, "Robust gesture recognition using millimetric-wave radar system," *IEEE Sensors Lett.*, pp. 1–1, 2018.

[129] Nasr, Jungmaier, Baheti, Noppeney, Bal, Wojnowski, Karagozler, Raja, Lien, Poupyrev, and Trotta, "A highly integrated 60 GHz 6-channel transceiver with antenna in package for smart sensing and short-range communications," *IEEE J. Solid-State Circuits*, vol. 51, no. 9, pp. 2066–2076, Sept 2016.

[130] Sun, Fei, Schliep, and Pohl, "Gesture classification with handcrafted micro-doppler features using a FMCW radar," in *IEEE MTT-S Int. Conf. Microw. Intellig. Mobility (ICMIM)*, April 2018, pp. 1–4.

[131] Wang, Wang, Zhou, Jiang, and Tian, "TS-I3D based hand gesture recognition method with radar sensor," *IEEE Access*, vol. 7, pp. 22 902–22 913, 2019.

[132] Zhou, Cao, and Pi, "Dynamic gesture recognition with a terahertz radar based on range profile sequences and doppler signatures," *Sensors*, vol. 18, no. 1, 2018.

[133] Infineon Technologies, "24 GHz FMCW radar module: BGT24MTR12."

[134] Analog Devices, "24 GHz FMCW radar MMIC evaluation board: EV-RADAR-MMIC."

[135] Suijker, Bolt, van Wanum, van Heijningen, Maas, and van Vliet, "Low cost low power 24 GHz FMCW radar transceiver for indoor presence detection," in *44th European Microw. Conf. (EuMC)*, Oct 2014, pp. 1758–1761.

[136] Novelda, "Impulse radar transceiver: NVA6201."

[137] Maxim Integrated, "2.4 GHz transceiver: MAX2829."

[138] Company, "5.8 GHz CW radar board: Bumblebee."

APPENDICES

A

Fabrication Process

A.1 CONTACT EVALUATION

Millimeter-wave (mm-wave) pulse generators in this thesis were fabricated in the Lund Nanolab. The fabricated circuits are based on the design by Lars Ohlsson [10]. In this thesis, the process was optimized with respect to the contact resistance of the metal-oxide-semiconductor field-effect transistor (MOSFET) and the collector contact of the resonant-tunneling diode (RTD). To evaluate the contact resistance using the transmission line method (TLM), a simplified process was implemented with dedicated samples. The contact evaluation process tries to reproduce conditions from the circuit fabrication process as close as possible. Processing steps are identical to the same sample preparation (SP), mesa etch (ME), contact regrow (CR), RTD definition and isolation (DI) and contact metalization (CM) steps of the device fabrication process (see Appendix A.2). Different etching recipes and regrow schemes were evaluated on this contact evaluation samples.

A.2 FABRICATION OF RTD-MOSFET PULSE GENERATORS

The mm-wave pulse generator design [26] was modified to include the sulfuric acid based etching recipe that gave the best results in the contact resistance evaluation.

SAMPLE PREPARATION (SP) Base of the fabrication process is an InP wafer with a molecular beam epitaxy (MBE) grown layer structure. This layer growth was performed by Intellepi Inc, Richardson, TX, USA.

SP 1. MBE layer growth on a InP wafer.

SP 2. Wafer dicing to 8 mm x 10 mm big chips

SP 3. Organic Solvent clean
- **SP 3.1.** acetone on hotplate 75 °C, 3 min.
- **SP 3.2.** transfer to ultrasonic bath, 1 min.
- **SP 3.3.** acetone on hotplate 75 °C, 3 min.
- **SP 3.4.** isopropanol on hotplate 75 °C, 1 min.

SP 4. Sample dehydration, hotplate 200 °C, 15 min.

MESA ETCH (ME) Since the RTD layer structure covers the whole sample, the layer structure is etched back selectively. The channel layer of the MOSFET is exposed, while on other areas the mesa structure of the RTD remains on the sample.

ME 1. Apply ma-N2403 Photoresist
- **ME 1.1.** spin-coating 4500 rpm, 45 s, (1500 rpm/s acceleration)
- **ME 1.2.** Softbake: hotplate 100 °C, 2min

ME 2. UV lithography (240 nm), 11s exposure

ME 3. Development:
- **ME 3.1.** MF319, submerge for 4 min
- **ME 3.2.** MF319, stir for 1 min
- **ME 3.3.** Deionized Water, submerge for 1 min

ME 4. O_2 Plasma ashing, 60 s

ME 5. Hardbake: Hotplate 140 °C, 10 min

ME 6. Wet etching
- **ME 6.1.** H_2SO_4:H_2O_2:H_2O (1:1:60), stir for 210 s
- **ME 6.2.** Deionized Water, stir for 30 s
- **ME 6.3.** HCl:H_3PO_4 (2:8), stir for 15 s
- **ME 6.4.** Deionized Water, stir for 60 s
- **ME 6.5.** H_2SO_4:H_2O_2:H_2O (1:1:60), stir for 100 s
- **ME 6.6.** Deionized Water, stir for 60 s

ME 7. Strip resist
- **ME 7.1.** acetone in ultrasonic bath, 2 min.
- **ME 7.2.** isopropanol, 1 min.

DUMMY GATE (DG) A layer of hydrogen silsesquioxane (HSQ) is structured to form a dummy gate, acting as template for the regrowth of contacts in the following step.

DG 1. Ozone Cleaning, O_2 flow 500 sccm, 10 min

DG 2. Wet etching
- **DG 2.1.** NH_4OH, stir for 10 s
- **DG 2.2.** Deionized Water, stir for 30 s
- **DG 2.3.** HCl:H_3PO_4 (2:8), stir for 10 s
- **DG 2.4.** Deionized Water, stir for 60 s

DG 2.5. NH_4OH, stir for 30 s
DG 2.6. Deionized Water, stir for 60 s
DG 3. Sample dehydration, hotplate 200 °C, 15 min
DG 4. Apply HSQ XR-1541-006 electron beam resist
DG 4.1. spin-coating 4500 rpm, 45 s, (1500 rpm/s acceleration)
DG 4.2. Softbake: hotplate 200 °C, 2min
DG 5. Electron Beam Lithography, 30 kV, Dose 700 $\mu C/cm^2$
DG 6. Development
DG 6.1. tetra-methyl ammonium hydroxide (TMAH), submerge for 60 s
DG 6.2. TMAH, stir gently for 60 s
DG 6.3. Deionized water, stir gently for 60 s
DG 6.4. new beaker of Deionized water, stir gently for 60 s

CONTACT REGROWTH (CR) A highly doped InGaAs layer and an InP support layer are regrown around the dummy gate. The regrown InGaAs layer forms the contacts to source and drain of the MOSFET and the collector of the RTD. The InP layer acts as support for the gate structure.

CR 1. Ozone Cleaning, O_2 flow 500 sccm, 10 min
CR 2. Wet etching
CR 2.1. NH_4OH, 30 s
CR 2.2. Deionized Water, 60 s
CR 3. Metal-organic vapour-phase epitaxy (MOCVD) Regrowth
CR 3.1. 30 nm highly doped InGaAs
CR 3.2. 55 nm InP, doped
CR 3.3. 55 nm InP, undoped

GATE FORMATION (GF) The dummy gate is etched, revealing the bare channel layer of the MOSFET. The gate stack is deposited on this layer: The gate oxide, consisting of a AlO2/HfO bilayer, and the gate metal (Ti/Pd/Au). After the gate deposition, the oxide is removed from the rest of the sample and also the sacrificial InP layer, regrown in the previous step, is etched back to form a T-shaped gate structure.

GF 1. Organic solvent clean
GF 1.1. acetone on hotplate 75 °C, submerge for 3 min.
GF 1.2. transfer to ultrasonic bath, 1 min.
GF 1.3. isopropanol on hotplate 75 °C, submerge for 1 min.
GF 2. Wet etching to strip HSQ resist
GF 2.1. Buffered oxide etch (BOE) 10:1, submerge for 3 min
GF 2.2. Deionized Water, submerge for 60 s
GF 3. Ozone Cleaning, O_2 flow 500 sccm, 10 min

GF 4. Surface Passivation
- **GF 4.1.** $(NH_4)_2S$:H_2O (1:2), submerge for 20 min
- **GF 4.2.** Deionized Water, submerge for 15 s

GF 5. Atomic layer deposition (ALD) of the gate oxide
- **GF 5.1.** 5 cycles: TMAl pulse at 300 °C
- **GF 5.2.** 5 cycles: TMAl pulse, H_2O pulse at 300 °C
- **GF 5.3.** 50 cycles: TDMAHf pulse, H_2O pulse at 100 °C

GF 6. apply PMMA 950 A6 electron beam resist
- **GF 6.1.** spin-coating 4500 rpm, 45 s, (1500 rpm/s acceleration)
- **GF 6.2.** Softbake: hotplate 180 °C, 2min
- **GF 6.3.** spin-coating 4500 rpm, 45 s, (1500 rpm/s acceleration)
- **GF 6.4.** Softbake: hotplate 180 °C, 2min

GF 7. Electron beam Lithography, Dose 250$\mu C/cm^2$

GF 8. Development
- **GF 8.1.** MIBK, submerge for 60 s
- **GF 8.2.** Isopropanol, submerge for 30 s

GF 9. O_2 Plasma ashing, 20 s

GF 10. Metal deposition by evaporation
- **GF 10.1.** 0.6 nm Ti, deposition rate 0.05 nm/s
- **GF 10.2.** 10 nm Pd, deposition rate 0.1 nm/s
- **GF 10.3.** 290 nm Au, deposition rate 0.2-0.5 nm/s

GF 11. Lift-Off
- **GF 11.1.** Acetone, submerge for 2 h
- **GF 11.2.** Isopropanol, submerge for 60 s

GF 12. Ozone Cleaning, O_2 flow 500 sccm, 10 min

GF 13. Wet etching
- **GF 13.1.** Buffered oxide etch (BOE) 10:1, submerge for 7 min
- **GF 13.2.** Deionized Water, sumberge for 1 min
- **GF 13.3.** NH_4OH, submerge for 10 s
- **GF 13.4.** HCL:H_2O (1:1), magnetic stir 500 rpm for 10 min
- **GF 13.5.** Deionized Water, submerge for 60 s
- **GF 13.6.** NH_4OH, submerge for 30 s
- **GF 13.7.** Deionized Water, submerge for 60 s

TOP CONTACT (TC) The collector contact on top of the RTD is deposited in this processing step. The contact metalization also acts as etch mask for the RTD during the wet etching in the next processing step.

TC 1. apply PMMA 950 A6 electron beam resist
- **TC 1.1.** spin-coating 4500 rpm, 45 s, (1500 rpm/s acceleration)
- **TC 1.2.** Softbake: hotplate 180 °C, 2min
- **TC 1.3.** spin-coating 4500 rpm, 45 s, (1500 rpm/s acceleration)

TC 1.4. Softbake: hotplate 180 °C, 2min
TC 2. Electron beam Lithography, Dose 250μC/cm^2
TC 3. Development
TC 3.1. MIBK, submerge for 60 s
TC 3.2. Isopropanol, submerge for 30 s
TC 4. O_2 Plasma ashing, 20 s
TC 5. Metal deposition by evaporation
TC 5.1. 20 nm Ti, deposition rate 0.1-0.2 nm/s
TC 5.2. 40 nm Pd, deposition rate 0.1-0.3 nm/s
TC 5.3. 340 nm Au, deposition rate 0.5-1 nm/s
TC 6. Lift-Off
TC 6.1. Acetone, submerge for 2 h
TC 6.2. Isopropanol, submerge for 60 s

RTD DEFINITION AND ISOLATION (DI) The semiconductor mesa is etched back to define the RTD structure. Around the MOSFETs, the mesa is etched to isolate the device from the rest of the circuit.

DI 1. Apply S1813 Photoresist
DI 1.1. spin-coating 6000 rpm, 45 s, (1500 rpm/s acceleration)
DI 1.2. Softbake: hotplate 115 °C, 90 s
DI 2. UV lithography (365 nm)
DI 2.1. Edge Bead Removal, 7 s exposure, develop
DI 2.2. Lithography, 5 s exposure
DI 3. Development:
DI 3.1. MF319, submerge for 1 min
DI 3.2. MF319, stir for 30 s
DI 3.3. MF319, stir for 30 s in new beaker
DI 3.4. Deionized Water, submerge for 1 min
DI 4. O_2 Plasma ashing, 20 s
DI 5. Hardbake: Hotplate 125 °C, 10 min
DI 6. Wet etching
DI 6.1. H_2SO_4:H_2O_2:H_2O (1:1:60), stir for 270 s
DI 6.2. Deionized Water, stir for 30 s
DI 6.3. HCl:H_3PO_4 (2:8), stir for 10 s
DI 6.4. Deionized Water, stir for 60 s
DI 6.5. NH_4OH, stir for 30 s
DI 6.6. Deionized Water, stir for 60 s
DI 7. Strip resist
DI 7.1. acetone on hotplate 75 °C, submerge for 2 min.
DI 7.2. isopropanol on hotplate 75 °C, submerge for 1 min.
DI 8. Ozone Cleaning, O_2 flow 500 sccm, 10 min

CONTACT METALISATION (CM) A metal layer is deposited to contact the emitter of the RTD and the source and drain of the MOSFET. The metal is structured by a lithography process using lift-off.

- **CM 1.** Apply LOR 10B Lift-off Resist
  - **CM 1.1.** spin-coating 3500 rpm, 45 s, (1500 rpm/s acceleration)
  - **CM 1.2.** Softbake: hotplate 190 °C, 5 min
- **CM 2.** Apply S1805 Photoresist
  - **CM 2.1.** spin-coating 6000 rpm, 45 s, (1500 rpm/s acceleration)
  - **CM 2.2.** Softbake: hotplate 115 °C, 90 s
- **CM 3.** UV lithography (365 nm), 18 s exposure
- **CM 4.** Development:
  - **CM 4.1.** MF319, stir for 27 s
  - **CM 4.2.** Deionized Water, stir for 1 min
- **CM 5.** Ozone Cleaning, O_2 flow 500 sccm, 10 min
- **CM 6.** Oxide etch
  - **CM 6.1.** HCL:H_2O (1:9), submerge for 60 s
  - **CM 6.2.** Deionized Water, submerge for 30 s
- **CM 7.** Metal deposition by evaporation, tilted 20°, rotation
  - **CM 7.1.** 15 nm Ti, deposition rate 0.1-0.2 nm/s
  - **CM 7.2.** 25 nm Pd, deposition rate 0.1-0.3 nm/s
  - **CM 7.3.** 400 nm Au, deposition rate 0.5-1 nm/s
- **CM 8.** Lift-Off
  - **CM 8.1.** Acetone, submerge for 2 h
  - **CM 8.2.** Isopropanol, submerge for 60 s
  - **CM 8.3.** Remover 1165 on hotplate 75 °C, 5 min
  - **CM 8.4.** Deionized Water, stir for 60 s

INTERLAYER DIELECTRIC (ID) A low permittivity interlayer dielectric (BCB) is deposited and structured by dry etching. The layer acts as passivation of the RTD and MOSFET. Also it isolates the devices from the following metalization layers.

- **ID 1.** Ozone Cleaning, O_2 flow 500 sccm, 10 min
- **ID 2.** Sample Dehydration, Hotplate at 200 °C
- **ID 3.** Apply Cyclotene 3022-46 dielectric (BCB)
  - **ID 3.1.** spin-coating 6000 rpm, 45 s, (1500 rpm/s acceleration)
  - **ID 3.2.** Softbake: hotplate 120 °C, 60 s
- **ID 4.** Cure BCB in RTP oven, N_2 Atmosphere
  - **ID 4.1.** Ramp 20 °C to 150 °C for 10 min
  - **ID 4.2.** Ramp 150 °C to 250 °C for 20 min
  - **ID 4.3.** Hold 250 °C for 50 min
  - **ID 4.4.** Let cool down

ID 5. Apply UV26 photo resist
- **ID 5.1.** spin-coating 4500 rpm, 45 s, (1500 rpm/s acceleration)
- **ID 5.2.** Softbake: hotplate 110 °C, 2 min

ID 6. UV lithography (240 nm)
- **ID 6.1.** Edge Bead Removal, 5 s exposure, develop
- **ID 6.2.** Lithography, 3 s exposure

ID 7. Post Exposure Bake: hotplate 110 °C, 2 min

ID 8. Development
- **ID 8.1.** MF26A, stir for 45 s
- **ID 8.2.** Deionized Water, stir for 30 s

ID 9. Dry etching, monitored by interferometer
- **ID 9.1.** Chamber preconditioning: SF_6:O_2 5:50 sccm, 200 mTorr, 5 min, 150 W
- **ID 9.2.** BCB etching: SF_6:O_2 5:50 sccm, 200 mTorr, 112 s, 150 W
- **ID 9.3.** mask etching: O_2 15 sccm, 300 mTorr, 35 s, 75 W
- **ID 9.4.** thinning: SF_6:O_2 3:25 sccm, 100 mTorr, 750 s, 30 W

ID 10. Hard Bake: hotplate 200 °C, 15 min

LOWER METAL LAYER (M1) The lower metal layer is deposited forming the coplanar waveguide (CPW) inductor, the interconnects, and the lower part of the metal-insulator-metal (MIM) capacitors.

M1 1. Apply LOR 10B Lift-off Resist
- **M1 1.1.** spin-coating 3500 rpm, 45 s, (1500 rpm/s acceleration)
- **M1 1.2.** Softbake: hotplate 190 °C, 5 min

M1 2. Apply S1805 Photoresist
- **M1 2.1.** spin-coating 6000 rpm, 45 s, (1500 rpm/s acceleration)
- **M1 2.2.** Softbake: hotplate 115 °C, 90 s

M1 3. UV lithography (365 nm), 18 s exposure

M1 4. Development:
- **M1 4.1.** MF319, stir for 26 s
- **M1 4.2.** Deionized Water, stir for 1 min

M1 5. O_2 Plasma ashing, 60 s

M1 6. Metal deposition by evaporation
- **M1 6.1.** 5 nm Ti, deposition rate 0.1-0.2 nm/s
- **M1 6.2.** 500 nm Au, deposition rate 0.5-1 nm/s

M1 7. Lift-Off
- **M1 7.1.** Acetone, submerge for 2 h
- **M1 7.2.** Isopropanol, submerge for 60 s
- **M1 7.3.** Remover 1165 on hotplate 75 °C, 5 min
- **M1 7.4.** Deionized Water, stir for 60 s

CAPACITOR DIELECTRIC (CD) A layer of HfO is deposited as dielectric for the MIM capacitor. Excess oxide is removed by wet etching and vias are formed to contact the lower metal layers.

CD 1. Ozone Cleaning, O_2 flow 500 sccm, 10 min
CD 2. ALD of the capacitor dielectric
  CD 2.1. 90 cycles: TDMAHf pulse, H_2O pulse at 150 °C
CD 3. Apply S1813 Photoresist
  CD 3.1. spin-coating 6000 rpm, 45 s, (1500 rpm/s acceleration)
  CD 3.2. Softbake: hotplate 115 °C, 90 s
CD 4. UV lithography (365 nm)
  CD 4.1. Lithography, 5 s exposure
CD 5. Development:
  CD 5.1. MF319, stir for 60 s
  CD 5.2. Deionized Water, stir for 30 s
CD 6. O_2 Plasma ashing, 60 s
CD 7. Hardbake: Hotplate 125 °C, 10 min
CD 8. Wet etching
  CD 8.1. BOE (10:1), submerge for 12 min
  CD 8.2. Deionized Water, stir for 60 s
CD 9. Strip resist
  CD 9.1. acetone on hotplate 75 °C, submerge for 2 min.
  CD 9.2. isopropanol, submerge for 1 min.

UPPER METAL LAYER (M2) Another metal layer is deposited to form interconnects, contact pads, and the upper layer of the MIM capacitor.

M2 1. Apply LOR 10B Lift-off Resist
  M2 1.1. spin-coating 3500 rpm, 45 s, (1500 rpm/s acceleration)
  M2 1.2. Softbake: hotplate 190 °C, 5 min
M2 2. Apply S1805 Photoresist
  M2 2.1. spin-coating 6000 rpm, 45 s, (1500 rpm/s acceleration)
  M2 2.2. Softbake: hotplate 115 °C, 90 s
M2 3. UV lithography (365 nm), 18 s exposure
M2 4. Development:
  M2 4.1. MF319, stir for 26 s
  M2 4.2. Deionized Water, stir for 1 min
M2 5. O_2 Plasma ashing, 30 s
M2 6. Metal deposition by evaporation
  M2 6.1. 5 nm Ti, deposition rate 0.1-0.2 nm/s
  M2 6.2. 500 nm Au, deposition rate 0.5-1 nm/s
M2 7. Lift-Off
  M2 7.1. Acetone, submerge for 2 h

M2 7.2. Isopropanol, submerge for 60 s
M2 7.3. Remover 1165 on hotplate 75 °C, 5 min
M2 7.4. Deionized Water, stir for 60 s

B

Modular Probing Setup

B.1 SETUP DESCRIPTION

For free-space millimeter-wave (mm-wave) measurements, a rigid measurement setup and precise alignment are crucial. No standardized way to build measurement setups exist, since the requirements depend on the specific application. In general, it is beneficial to be able to place the transmitter and receiver as freely as possible and to avoid any obstruction of the free-space path. In the scope of this thesis, a modular measurement setup was developed that allows to implement measurements for multiple purposes.

The base of the setup is formed by a Newport optical table with passively damped legs. The table has a 25 mm x 25 mm grid with M6 screw holes. These holes can be used to attach the different components of a measurement setup. Holders and motorized stages can be used to support antennas in free-space measurements. One limitation for free-space setups is the metallic surface of the optical table. For many measurements unwanted reflections can be avoided, by using directional antennas, placing the metal surface out of the main beam path. Additionally, microwave absorbers can be placed on the table surface to dampen its reflection.

For the measurements in this thesis, the fabricated pulse generator circuits were probed with a probe station. Since no packaging approach was investigated in the scope of this thesis, the circuits were contacted with RF probes. To mitigate this limitation, a modular probing setup was designed. A photograph of the probing part of the setup is shown in Fig. B.1. The probing setup uses commercially available probe positioners and probes in combination with a custom made platform to support the positioners. The sample can be placed on a custom made vacuum chuck attached to precision positioners to align the sample. To be able to place the probes precisely, a

USB-microscope on a separate removable holder is used. The setup allows to remove unused parts, to ensure that the free-space path during measurement is not obstructed.

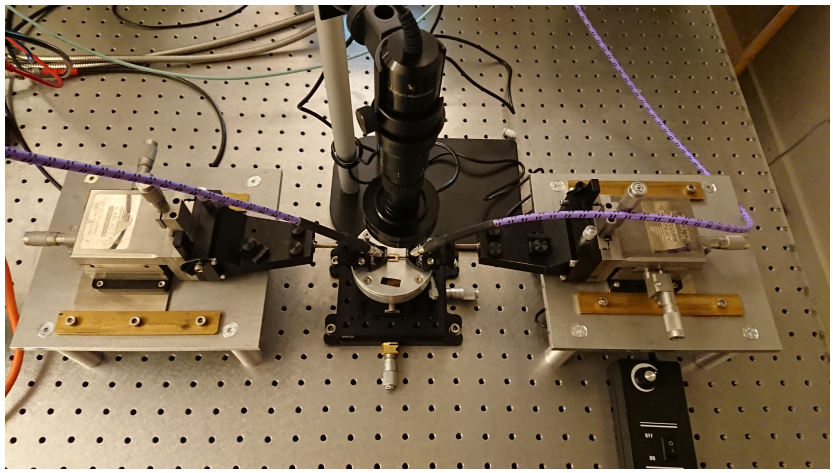

Figure B.1: A photograph of the custom made probing setup.

B.2 BILL OF MATERIALS

The bill of materials of the setup is summarized in Table B.1.

Table B.1: Bill of Materials

Supplier	ID	Qty	Description
Newport	RS 2000	1	Optical Table as rigid platform
Newport	SL-600	4	Passively Damped legs for the table
Thorlabs	LTS-300	6	motorized linear stage with 30 cm travel
Thorlabs	CR1/M	2	motorized rotational stage
Thorlabs	XYT1/M	1	2 axis liner positioning stage
Thorlabs	PRO1/M	1	Rotation positioning stage
Cascade	114-746B	2	Probe positioners
Custom[1]	-	1	Vacuum chuck
Custom[1]	-	2	Platform to hold the Probe positioners
GGB	67A-GSG	2	RF Probes DC-67GHz
Dino-Eye	AM4023CT-LH1	1	22X-220X Zoom USB Microscope

[1]Manufactured by Prototypverkstaden AB, Lund

C

Overview of Radar-Based Gesture Recognition Systems

In recent years, radar based gesture recognition has been demonstrated in many studies. Table C.1 shows an overview of radar-based gesture recognition approaches. Gesture recognition has been implemented with various radar systems in different frequency bands. First approaches showed that the radiation from wireless local area networking (WLAN) in the environment can be used for the detection of arm gestures [109, 114]. Similarly, also active radar systems using radar systems at frequencies below 10 GHz have been presented [106, 108, 115–118]. Even sensors based on ultra-wideband (UWB) pulses [119] and near field perturbation [120] have been proposed. At higher frequencies, the 24 GHz band [107,121–126], the 60 GHz band [1,105,127–129], the 77 GHz band [130, 131], and even in the 340 GHz band [132], have been used. By far the most common approach is frequency modulated continuous wave (FMCW). The spatial resolution of these systems is mainly used to make these systems more robust against background signals. For gesture classification, the micro-Doppler signatures obtained by pulse-Doppler processing (cf. Fig. 2.2) are used as input for the classifier. Classification algorithms of different complexity have been proposed, achieving classification accuracies of 84 % and higher. The classification approach in Paper VI, directly uses range time data for classification. Zhou *et al.* also demonstrated a direct classification of range-time data at 340 GHz [132]. The high available bandwidth at these frequency enables to resolve features of the hand with very high resolution. Potentially, much smaller scale movements of the hand might be resolved. Scaling the RTD-MOSFET pulse generator to these frequencies might offer a efficient way, to implement a gesture recognition systems at 340 GHz and beyond.

Table C.1: Comparison of radar-based gesture recognition

	Scale	Type	Band	Resolution	# Channels	# Gestures	Accuracy	Platform
Paper VI	Hand	Pulse	60 GHz	9 cm	1	12	98.60 %	RTD-MOSFET
[1]	Hand	FMCW	60 GHz	2.1 cm	8	4	92.10 %	[129]
[105]	Hand	FMCW	60 GHz	2.1 cm	8	5	93.30 %	[129]
[128]	Body	FMCW	60 GHz	2.1 cm	4	5	95.38 %	[129]
[127]	Body	FMCW	60 GHz	2.1 cm	2	8	87 %	[129]
[130]	Body	FMCW	77 GHz	9.3 cm	1	7	84 %	[129]
[131]	Body	FMCW	77 GHz	3.8 cm	1	10	96.2 %	n.a.
[132]	Hand	FMCW	340 GHz	0.7 cm	1	3	91.5 %	n.a.
[107]	Hand	FMCW	24 GHz	85 cm	4	7	83.3 %	n.a.
[122]	Body	FMCW	24 GHz	3.8 cm	2	8	95.5 %	[133]
[124]	Hand	FMCW	24 GHz	3.8 cm	2	14	95 %	[133]
[123]	Hand	FMCW	24 GHz	60 cm	4	7	91 %	[134]
[125]	Hand	FMCW	24 GHz	60 cm	1	3	99 %	[135]
[126]	Hand	CW	25 GHz	-	1	4	96 %	n.a.
[119]	Hand	IR-UWB	6.8 GHz	6.5 cm	1	5	99 %	[136]
[116]	Body	CW	5.8 GHz	-	2	4	98 %	[137]
[106]	Hand	CW	5.8 GHz	-	1	7	93.10 %	[138]
[108]	Hand	CW	2.4 GHz	-	1	6	91 %	n.a.
[120]	Hand	near field	2.4 GHz	-	2	5	94.60 %	n.a.
[114]	Body	WiFi	2.4 GHz	-	5	9	90 %	n.a.

PAPERS

Paper I

Paper I

Pre-peer-reviewed version, reproduced in printed version only, submitted as:

Sebastian Heunisch, Lars Ohlsson Fhager, and Lars-Erik Wernersson, "A Phase-Correlated Duo-Binary Waveform Generation Technique for Millimeter-Wave Radar Pulses," *International Journal of Circuit Theory and Applications*, submitted: May 2019.

Paper II

Paper II

Peer-reviewed version, reproduced from:

Sebastian Heunisch, Lars Ohlsson Fhager, and Lars-Erik Wernersson, "Clutter Analysis in a Time-Domain Millimeter-Wave Reflectometry Setup," *12th European Conference on Antennas and Propagation (EuCAP)*, London, 2018, pp. 1-4..

Clutter Analysis in a Time-Domain Millimeter-Wave Reflectometry Setup

Sebastian Heunisch, Lars Ohlsson, and Lars-Erik Wernersson
Electrical and Information Technology, EIT
Lund University
22311 Lund Sweden
Email: Sebastian.Heunisch@eit.lth.se

***Abstract*—In this work, we study the clutter and multi-path propagation in a time-domain millimeter-wave reflectometry setup, used for material characterization or short-range imaging. The signal energy and fidelity factor of the different reflection components is analyzed in dependence of the distance from the target. Due to the change in pulse distortion in the multi-path components, the system impulse response is dependent on the target position. The principal reflection from the target on the other hand is only influenced by the path loss. By coherent superposition we are able to separate the target reflection from the static system clutter and multi-path reflections in the setup.**

***Index Terms*—clutter, millimeter-wave reflectometry, multi-path propagation, time-domain measurements.**

I. Introduction

Millimeter-waves (mm-waves) find use in applications ranging from automotive radar systems [1] to high-speed communication systems [2]. With recent advances of mm-wave circuit technology, the integration of mm-wave transmitters in hand-held or wearable devices comes in reach. This opens up a range of interesting new applications, like gesture control [3] or material identification [4] using hand-held devices. For these applications the power consumption of those circuits is crucial. Pulsed, time-domain systems can achieve very low power consumption by using low duty cycles [5]. Therefore, time-domain systems are well suited for applications, like high-resolution imaging or high-precision material characterization, where high pulse repetition rates are not necessary.

For these time-domain reflectometry systems, unwanted reflections, so called clutter, interfere with the signal. Similarly to wireless communication systems, the interaction of the transmitted waves with the environment leads to interference and distortion, which limit the measurement accuracy. Existing narrowband models cannot be used directly in ultra-wideband, time-domain systems and therefore new models are investigated [6]. In general, clutter is correlated to the signal and therefore cannot be removed by averaging or matched filtering. For narrowband frequency-domain reflectometry systems free-space calibration techniques have been proposed [7]–[9]. Due to the broadband nature of time-domain pulses, they cannot be applied directly, though. Usually, time-domain gating techniques are used to remove multi-path components [10], however, additional errors can be introduced in the signal. Also, the parts of the clutter interfering with the signal cannot be removed.

In this work, we study the signal and clutter in a time-domain mm-wave reflectometry setup. We identify and separate background clutter and multiple reflections in the setup from the primary reflection of a target using coherent superposition of shifted measurements. We examine the fidelity factor and pulse energy of the primary and higher order reflections in dependence on the distance from the antennas.

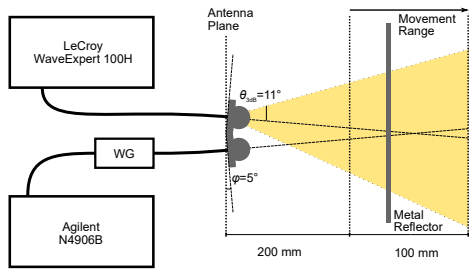

Fig. 1. The used reflectometry setup. A 300x300 mm big metal mounted on a translational stage in a distance of 200 mm from a pair of wideband leaky lens antennas ($\theta_{3dB} = 11°$ at 60 GHz). The reflector is swept over a distance of 100 mm and the reflection is recorded.

II. Measurement

We performed measurements with a reflectometry setup (cf. Fig. 1) comparable to our previously presented material characterization setup [11]. Time-domain pulses with a carrier frequency of 65 GHz and a duration of 80 ps are generated using an in-house wavelet generator [12]. The pulse duration is set by the pulse generator of an Agilent N4906B bit error rate tester. Wavelets are transmitted and received using a pair of wideband leaky lens antennas. This antenna type shows low dispersion over a wide bandwidth, and pulse distortion caused by the antennas is therefore negligible [13]. A LeCroy WaveExpert 100h sampling oscilloscope acts as a receiver. Antennas are mounted side by side, with a tilt of 5° towards each other. The antennas illuminate the center of a 300x300 mm big metal plate as target. The metal plate is swept by a Thorlabs LTS300 translational stage from a distance of 200 mm to 300 mm from the antennas with a step of 1 mm. At each step the target reflection was recorded, while averaging over 5000 measurements to suppress uncorrelated noise. An overview over the resulting measurements is shown in Fig. 2.

III. Reflectometry Clutter Analysis

From the position dependent reflection in Fig. 2b, we identify different clutter components. Those components can

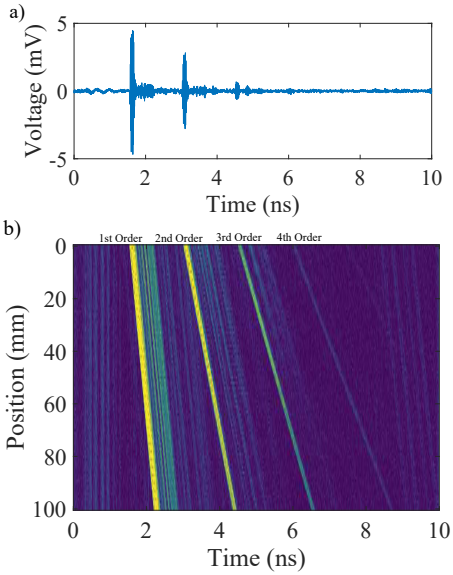

Fig. 2. The measured reflection of the metal plate at 200 mm distance to the antennas (a). When sweeping the distance over a range of 100 mm the time delays of the reflections change. This can be seen in the intensity map of the reflections in dependence of time delay and target position (b). Multiple reflections between the reflector and the environment differ in time delay.

be grouped by their delay. Certain parts of the signal are static and don't change when changing the target position. The principal reflection from the target changes linearly with a displacement of the target. Other parts change with multiples of the target delay τ_s. We therefore use a generic model of the impulse response of the reflectometry setup:

$$h(t) = h_0(t) + A(t-\tau_s) + B(t-2\tau_s) + C(t-3\tau_s) + ..., \quad (1)$$

where $h_0(t)$ describes the static reflection in the setup, and A, B and C describe the impulse responses of the principal and multiple reflections, respectively. The target delay τ_s in dependence of the range, x, from the antennas can simply be calculated by

$$\tau_s = \frac{2x}{c_0}, \quad (2)$$

where c_0 is the speed of light in free space. The reflection response to a wavelet $w(t)$ is calculated by the convolution of $h_0(t)$ and $w(t)$.

The model is easily verified by looking at the time delays of the individual components in dependence of the position of the reflector (cf. Fig. 3). The measured time delays agree well with the expected time delays. The impulse responses $h_0(t), A(t), B(t)$ and $C(t)$, however, still need to be characterized. We start by investigating the background clutter $h_0(t)$. Various static clutter components can be identified in Fig. 2. These components are correlated to the transmitted wavelet, since they are not canceled by averaging the measurements. When we superimpose the measurements by averaging the

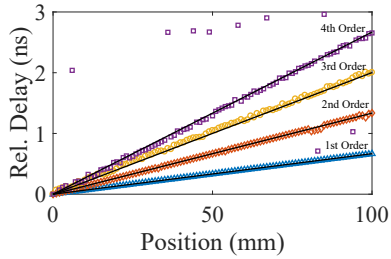

Fig. 3. Relative Delay of the reflection from the target and higher order reflections between the target and the environment. The measurement (Markers) are in well agreement to the expected delay (solid line).

measurements at all different positions, they will therefore remain. The reflections from the target at different positions, on the other hand, will be suppressed, since the wavelets are out of phase and therefore uncorrelated. The resulting waveform (cf. Fig. 4a) contains only the background clutter $h_0(t)$ convoluted with the incident wavelet $w(t)$ and some residual error from the superposition of the target reflections, which disappears for averaging over a large number of measurements. In a similar way the primary target reflection can be obtained. By shifting the reflection from each target position back by its propagation delay, the reflections are brought in phase. The amplitude difference due to the free space path loss can easily be compensated by multiplying with a position dependent constant, obtained from the energy of the pulse. When superimposing the delay and path loss corrected reflections of the target by averaging, other components cancel out and only the target response remains (cf. Fig. 4b). The remaining multi-path clutter can be obtained by subtracting the background clutter and the target reflection from the initial measurement (cf. Fig. 4c).

Applying the same method to the multi-path reflections from the target failed. The superposition of the secondary target reflection resulted in a wavelet of only about half the amplitude of the initial pulse. This indicates a distortion of the pulses at higher order reflection that causes partial incoherence of the pulses. To analyze this, we examine the waveforms of the individual higher order reflections separately. We define a span of 1500 ps starting 200 ps before the maximum of the pulse. The energy of the pulse $p(t)$ can be defined as:

$$E = \int_{t_0}^{t_1} |p(t)|^2 dt, \quad (3)$$

where the integration boundaries t_0 and t_1 are the borders of the examined timespan. The energy of the wavelets in dependence of the reflector position is shown in Fig. 5a. In general, the energy of the individual reflection components decay with distance of the target to the antennas. The energy of the secondary reflection, for instance, drops significantly with target position. However, the ternary target reflection even increases with distance from the target before it drops. This effect can be attributed to the diffuse scattering of the wavelets in the antenna plane. Diffuse scattering would cause distortion in the pulses. To examine how well the coherence of wideband

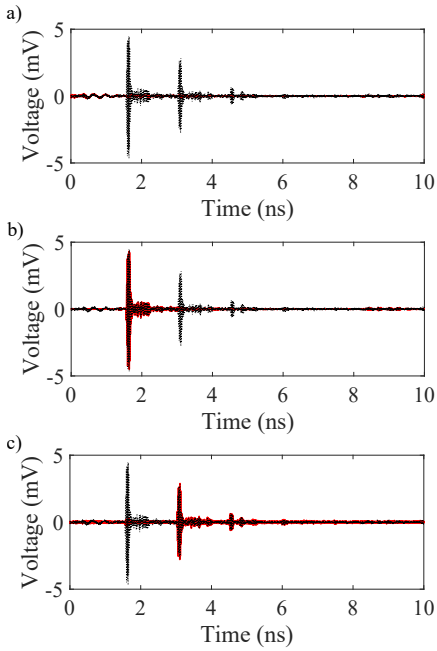

Fig. 4. Using coherent superposition the signal (dashed line), can be separated in the background clutter, the principal reflection and a residual clutter component, containing multiple reflections.

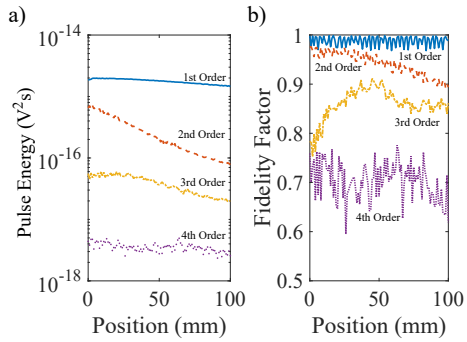

Fig. 5. Energy (a) and fidelity factor (b) of the wavelets for different reflection components. The primary reflection (solid) of the target is nearly undistorted (fidelity factor close to unity) and the energy is decaying according to the free space path loss. For the higher order reflections, the pulse distortion and energy doesn't scale linearly with the target position.

pulses is preserved, the fidelity factor has been proposed [14], [15]. Similarly, the fidelity factor can be defined for the pulses in the examined frequency span around the pulse

$$F = \max_{\tau} \left(\int \frac{p(t)}{E_{\mathrm{p}}} \frac{w(t+\tau)}{E_{\mathrm{w}}} dt \right), \tag{4}$$

where E_{p} and E_{w} is the energy according to (3) of the pulse $p(t)$ and the incident wavelet $w(t)$, respectively. The fidelity factor for the principal reflection is close to unity for all target positions while it is varying with distance for higher order components (cf. Fig 5b).

IV. Discussion

The presented analysis shows, that a simple model of the form (1) can be used to describe the clutter components in a reflectometry setup. The impulse response $A(t)$ of the principal reflection is mainly dependent on the target reflection coefficient. The fidelity factor is constant over the measurement range and close to unity. The fluctuations in the fidelity factor can possibly be attributed to defocusing through the bistatic configuration or the illumination of reflector edges. This is subject to further investigation. The higher order impulse responses $(B(t), C(t), ...)$, however, are influenced by the reflection in the antenna plane as well. The energy of the higher order reflections doesn't scale linearly with the distance of the target. Also higher order reflections introduce significant distortion of the incident wavelet, also not linearly dependent on the target position. This is caused by scattering on the complex geometry in the antenna plane. Diffuse scattering at edges and closely spaced objects will lead to incoherence of the pulse in dependence of the target position. For a narrow band system this effect could be formulated as a frequency dependent phase error. For wideband pulses this is not possible, and the impulse responses for higher order reflections need to be formulated in dependence of the target position.

V. Conclusion

We measured the reflection in a time-domain mm-wave reflectometry setup and characterized the clutter in the system. A simple model for the impulse response is able to describe the time delays of the target reflection and multiple reflections to the target. We were able to separate the target reflection from the static background clutter and multiple reflections with the target. We quantified the energy dependence and the fidelity factor of the different order pulses, in dependence of the target position. The principle reflection preserves the coherence of the incident pulse well, shown by a fidelity factor close to unity. Higher order reflections of the target, however, show a significant distortion of the pulse, which is not linearly dependent on the target position. Impulse responses of higher order reflections are therefore dependent on the distance to the target. Modeling the impulse responses in dependence to antenna and target geometry is subject to future investigations.

Acknowledgment

This work was supported in part by the Swedish Foundation for Strategic Research (SSF), in part by the Swedish Research Council (VR), and in part by the Knut and Alice Wallenberg Foundation.

REFERENCES

[1] J. Hasch, E. Topak, R. Schnabel, T. Zwick, R. Weigel, and C. Waldschmidt, "Millimeter-wave technology for automotive radar sensors in the 77 GHz frequency band," *IEEE Transactions on Microwave Theory and Techniques*, vol. 60, no. 3, pp. 845–860, March 2012.

[2] L. Ohlsson and L.-E. Wernersson, "A 15-Gb/s wireless ON-OFF keying link," *Access, IEEE*, vol. 2, pp. 1307–1313, 2014.

[3] J. Lien, N. Gillian, M. E. Karagozler, P. Amihood, C. Schwesig, E. Olson, H. Raja, and I. Poupyrev, "Soli: Ubiquitous gesture sensing with millimeter wave radar," *ACM Trans. Graph.*, vol. 35, no. 4, pp. 142:1–142:19, Jul. 2016.

[4] H.-S. Yeo, G. Flamich, P. Schrempf, D. Harris-Birtill, and A. Quigley, "Radarcat: Radar categorization for input & interaction," in *Proceedings of the 29th Annual Symposium on User Interface Software and Technology*, ser. UIST '16. New York, NY, USA: ACM, 2016, pp. 833–841.

[5] R. J. Fontana, "Recent system applications of short-pulse ultra-wideband (UWB) technology," *IEEE Transactions on Microwave Theory and Techniques*, vol. 52, no. 9, pp. 2087–2104, Sept 2004.

[6] A. F. Molisch, "Ultrawideband propagation channels-theory, measurement, and modeling," *IEEE Transactions on Vehicular Technology*, vol. 54, no. 5, pp. 1528–1545, Sept 2005.

[7] M. H. Umari, D. K. Ghodgaonkar, V. V. Varadan, and V. K. Varadan, "A free-space bistatic calibration technique for the measurement of parallel and perpendicular reflection coefficients of planar samples," *IEEE Transactions on Instrumentation and Measurement*, vol. 40, no. 1, pp. 19–24, Feb 1991.

[8] P. G. Bartley and S. B. Begley, "Improved free-space S-parameter calibration," in *2005 IEEE Instrumentationand Measurement Technology Conference Proceedings*, vol. 1, May 2005, pp. 372–375.

[9] I. Rolfes, "Microwave free space calibration methods," in *Precision Electromagnetic Measurements Digest, 2004 Conference on*, June 2004, pp. 72–73.

[10] A. M. Nicolson, C. L. Bennett, D. Lamesdorf, and L. Susman, "Applications of time-domain metrology to the automation of broad-band microwave measurements," *IEEE Transactions on Microwave Theory and Techniques*, vol. 20, no. 1, pp. 3–9, Jan 1972.

[11] I. Vakili, L. Ohlsson, L.-E. Wernersson, and M. Gustafsson, "Time-Domain System for Millimeter-Wave Material Characterization," *IEEE Transactions on Microwave Theory and Techniques*, vol. 63, no. 9, pp. 2915–2922, 2015.

[12] L. Ohlsson, P. Fay, and L.-E. Wernersson, "Picosecond dynamics in a millimetre-wave RTD-MOSFET wavelet generator," *Electronics Letters*, vol. 51, no. 21, pp. 1671–1673, 2015.

[13] I. Vakili, L. Ohlsson, M. Gustafsson, and L.-E. Wernersson, "Wideband and non-dispersive wavelet transmission using leaky lens antenna," *Electronics Letters*, vol. 49, no. 5, pp. 321–322, February 2013.

[14] D. Lamensdorf and L. Susman, "Baseband-pulse-antenna techniques," *IEEE Antennas and Propagation Magazine*, vol. 36, no. 1, pp. 20–30, Feb 1994.

[15] D.-H. Kwon, "Effect of antenna gain and group delay variations on pulse-preserving capabilities of ultrawideband antennas," *IEEE Transactions on Antennas and Propagation*, vol. 54, no. 8, pp. 2208–2215, Aug 2006.

Paper III

Paper III

Peer-reviewed version, reproduced from:

Sebastian Heunisch, Lars Ohlsson Fhager, and Lars-Erik Wernersson, "Reflection of Coherent Millimeter-Wave Wavelets on Dispersive Materials: A Study on Porcine Skin," *IEEE Transactions on Microwave Theory and Techniques*, vol. 66, no. 4, pp. 0018-9480, 2018..

Reflection of Coherent Millimeter-Wave Wavelets on Dispersive Materials: A Study on Porcine Skin

Sebastian Heunisch, Lars Ohlsson, and Lars-Erik Wernersson

***Abstract*—Differences in the material reflection are required for any contrast in microwave and millimeter-wave imaging systems. Therefore the dielectric properties, which determine the reflection of materials, need to be characterized. The characterization of skin and other biological tissue is therefore necessary, to apply imaging systems for instance in cancer diagnosis.**

In this paper, short, coherent millimeter-wave pulses (wavelets) are generated and their reflection on dispersive materials is studied. The reflections of wavelets on porcine skin and water are examined in time- and frequency domain. A first order Debye model is fitted to the reflection coefficient in frequency domain to quantify material dispersion. The frequency-dependent reflection on dispersive materials causes a distortion of the wavelets in the time domain. The start-up behavior of the pulses is examined by simulation and measurements. The rise time of the pulses is identified as a feature in time domain for wavelets reflected on dispersive media. Together with other features characteristic for a pulse, for instance the wavelet amplitude, this enables identification of dispersive materials by reflectometry measurements, making it suitable for applications in millimeter-wave imaging systems.

***Index Terms*—Biomedical applications, Debye model, dispersive materials, ex-vivo tissues, microwave imaging, millimeter waves, reflectometry, rise time, time-domain analysis, permittivity measurement**

I. Introduction

WITH the evolution of integrated microwave circuits, microwave and millimeter wave (mm-wave) radar and imaging systems have become more and more available. Millimeter-wave radar sensors are, for instance, used in body scanners at airports and distance sensors in cars. The material properties of the target determine the reflection of radar signals. Therefore, in particular the complex dielectric permittivity of the imaged materials need to be known. Frequency domain measurements using a vector network analyzer have become the standard technique to perform material characterization with high precision in a laboratory environment. However, for the integration in low-power imaging systems and sensors, time-domain systems offer an attractive alternative. Low pulse-rate time-domain systems can achieve very low power consumption by using very low duty-cycles [1]. This may enable the integration of these sensors in portable systems, leading to a variety of new interesting applications.

Manuscript received XX XX, 201X; revised XX XX, 201X; accepted XX XX, 201X. Date of publication XX XX, 201X; date of current version XX XX, 201X. This work was supported in part by the Swedish Research Council (VR), in part by the Swedish Foundation for Strategic Research (SSF), and in part by the Knut and Alice Wallenberg Foundation. The authors are with the Department of Electrical and Information Technology, Lund University, SE-221 00 Lund, Sweden (e-mail: sebastian.heunisch@eit.lth.se). Color versions of one or more of the figures in this paper are available online at http://ieeexplore.ieee.org.

Microwave imaging has been proposed for early detection of cancer [2]. Cancer diagnosis with microwaves is potentially cheaper than magneto-resonance tomography (MRT), more sensitive than ultrasound, and less harmful than X-Ray imaging. For breast cancer recognition, for instance, it is considered as a promising technology to replace mammography as a standard diagnosis method [3]. The resolution of a microwave imaging system depends mainly on the bandwidth of the signals used [4]. The available bandwidth increases with frequency, however, the penetration depth in many materials is decreasing with frequency due to higher attenuation. Electromagnetic waves at mm-wave frequencies penetrate only the top layers of organic tissue [5]. Nevertheless, this can be an advantage when screening only surface layers (e.g. skin), since reflections from buried features like fat layers and bones can be neglected. Millimeter wave and terahertz imaging might therefore be suitable for the recognition of skin cancer [6].

The dielectric properties of organic tissue are mainly determined by its water content [7], [8]. For cancerous cells, a higher water content than in healthy tissue has been observed [6]. Therefore a dielectric contrast exists between the two, which has been demonstrated for measurements on breast cancer tissue [9]. To accurately measure the dielectric properties of materials, various methods have been proposed and used [10]–[12]. Unfortunately, many of those methods require the material under test (MUT) to be cut in thin slices for measuring transmission or fitting a fixture (e.g. a waveguide). Since the frequency components of a pulse propagate with different speed, dispersion leads to broadening and phase distortion of a pulse. The interaction strength for dispersive propagation is proportional to the propagation length in the medium. The influence of dispersion on the reflection at a material interface, on the other hand, is independent of the propagation depth. Theoretical approximations for the material impulse response in reflection have been described in [13]–[15]. Just like in transmission, the reflection of a pulse on a dispersive medium leads to a distortion of the pulse [16].

In this work, we studied the reflection of coherent time-domain pulses (wavelets) on dispersive materials, deionized water and porcine skin, in a free space setup. For this, we used 80-ps-long wavelets with a center frequency of 55 GHz, generated by an in-house fabricated wavelet generator [17]. The short pulse duration enables the interaction of the pulses over a large measurement bandwidth. Debye parameters of the measured materials were estimated in frequency domain by fitting a model for the reflection using a brute force search. The coherent property of the generated wavelets enables a direct evaluation of the shape of the reflected pulses in time domain. The influence of the dispersive reflection was evalu-

ated by simulating time-domain waveforms and comparing to measured wavelets.

The paper is organized as follows. In Section II, the measurement setup and the sample preparation is described. In Section III, the measured signals are analyzed in frequency domain and the permittivity of the MUTs are estimated with brute force fitting. The dispersive reflection is then analyzed qualitatively in time domain in Section IV. The reflection response from dispersive MUTs are simulated and compared to measured wavelets. Finally, the conclusions of the paper are summarized in Section V.

II. Experiments

To study the reflection of short wavelets on dispersive materials a special measurement system was developed. The measurement setup uses similar components as our previous characterization system [18], but, in contrast to our previous setup, measurements are acquired in reflection. This requires more care about alignment of angles and positions, since any error in alignment leads to an error in the amplitude and phase of the measured signals. To solve this, special holders were fabricated and additional calibration measurements were taken.

A. Measurement System

An in-house fabricated circuit is used to generate wavelets in the mm-wave range [17]. This circuit consists of a negative differential conductance oscillator formed by a resonant tunneling diode (RTD) in parallel with a coplanar waveguide stub as inductance. The oscillation frequency is set by the capacitance of the RTD and the parallel inductance in the circuit. A metal-oxide-semiconductor field-effect transistor (MOSFET) integrated in series with the RTD is used to switch its bias and quench the oscillation during the off-state. This efficiently generates wavelets with the circuit's oscillation frequency and a pulse length defined by a baseband signal connected to the gate of the MOSFET. The circuits are designed to have a oscillation frequency of 55 GHz and the baseband signal is chosen as a 80-ps-long rectangular pulse with a repetition time of 10 ns. The baseband signal is provided by the pulse pattern generator of an Agilent N4906B BERT.

The generated wavelets are transmitted using a wideband antenna consisting of a slot waveguide radiating into a hemispherical silicon lens. This leaky lens antenna shows good matching and low distortion of emitted wavelets over a bandwidth from 15 GHz till 67 GHz [19] [19]. An identical antenna in combination with an LeCroy WaveExpert 100h/SE-70 sampling oscilloscope with a nominal bandwidth of 70 GHz is used for receiving the reflected wavelets.

The receiving antenna is arranged side by side with the transmitting antenna, as illustrated in Fig. 1. The antennas are mounted with a separation of 50 mm center to center, having a 5 degree tilt towards each other. The beam path is located 150 mm above a metal baseplate. At a distance of 250 mm from the antennas, a sample holder consisting of a 300x300x20 mm slab of poly(methyl methacrylate) glass (PMMA) is mounted. A second slab of PMMA can be used to sandwich flexible materials under test (MUT) and clamp them

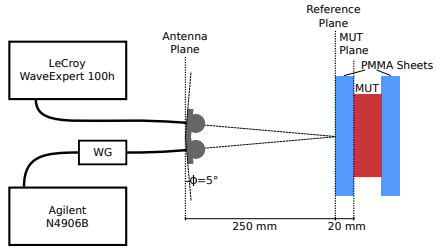

Fig. 1. Schematic top view of the measurement setup

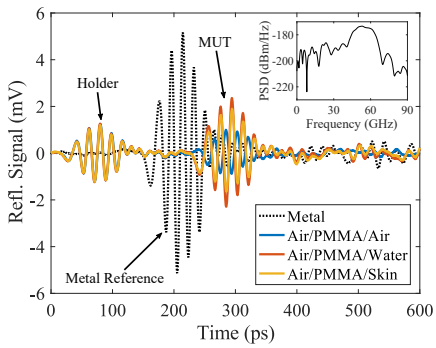

Fig. 2. Principal reflected pulses from PMMA holder interface (left) and material under test (MUT) interface (right). The reflection from the air-PMMA interface of the sample holder is the same for all the measurements while the reflection from the PMMA-MUT interface differs in amplitude and carrier phase for the different MUTs. The reflection of a metal sheet (dotted), located in the same physical position as the MUTs, is used as reference.

to the first slab. For reference measurements, a metal sheet can be aligned with the back of the first PMMA slab of the sample holder. To provide the necessary mechanical stability and positioning accuracy, the sample holder, the reference objects, as well as the antennas are fixed to the same base plate as the antennas. Noise in the measurements was suppressed by averaging over 5000 measurements. To examine repeatability, the measurements were taken in different measurement sessions. We are able to reproduce time-domain waveforms between independent measurements of the same object with negligible variation.

B. Sample Preparation and Measurements

As calibration procedure, a metal sheet was brought in contact with the back of the first PMMA slab of the sample holder. The PMMA was then removed and the reflection on a blank metal sheet was recorded as a first reference measurement. The PMMA slab was then mounted back to its previous position and the metal sheet was removed. The reflection of the PMMA slab was recorded as second reference measurement.

Deionized water, taken from a Millipore Milli-Q filter system, was filled in a low-density-polyethylene (LDPE) bag between the PMMA slabs of the sample holder. The spacing of the PMMA slabs was fixed with spacers to 4.8 mm. Care was taken that the bag LDPE was in tight contact with the PMMA slabs and no air bubbles formed in the water.

The porcine skin sample was cut from a fresh piece of porcine rind to a thickness of approximately 20 mm. It was kept in a refrigerator and removed 30 minutes prior to the measurement to let the skin layer adjust to room temperature. The sample was clamped with moderate pressure in between two PMMA sheets of the sample holder to stabilize the sample and planarize its surface.

Wavelets with a oscillation frequency of 55 GHz and a duration of 80 ps were generated and the reflection recorded. The first 2 ns of a reflected signal were recorded with the sampling oscilloscope. The reflection responses from the MUTs as well as the reference measurements are shown in Fig. 2. The reflection at the first interface of the sample holder (left pulse) is the same for all MUTs and is used as reference plane. The reflection from the second interface (right pulse) is determined by the dielectric contrast of the materials, and is therefore different for the MUTs. The reflection of a metal sheet (dotted pulse) is used as a reference.

III. Frequency-Domain Permittivity Estimation

To quantify the material dispersion, the measured MUTs were analyzed in frequency domain. Using the reference measurements the reflection transfer function was calculated. The PMMA slab of the sample holder was characterized first and then de-embedded from the measurements of the MUT. Finally Debye parameters of skin and water were fitted using a brute force parameter optimization.

A. Signal Processing

The signal processing follows the scheme in Fig. 3. First the transfer function $\Gamma(\omega)$ is calculated by normalizing the reflected signal by a template wavelet in frequency domain. This template wavelet including the transmission through the measurement system is obtained by the measurement of the reflection of the wavelet on a metal slab. The reflection from this slab is assumed as ideal with a reflection coefficient of $\Gamma(\omega) = -1$. To perform this normalization accurately, a precise reference measurement is crucial. A small offset in angle or position results in an error in the reflected amplitude and phase. To minimize positioning errors and ensure reliable alignment of the reflection angle, the reflection of a metal reflector aligned with the back of the sample holder is measured (cf. Section II-B). The resulting offset of the metal sheet is compensated by shifting the measurement by the electrical distance of the sample holder and compensating for the propagation loss according to Friis transmission equation [20]. This shifting can be performed very precisely since the measurement of the sample holder can be used to align the pulse peaks. Aligning the measurements to the reflection peak from the sample holder can also be used to compensate for drift in the sampling oscilloscope.

The reflection measurements, shifted to the same reference plane, are then transformed to frequency domain using a fast Fourier transform (FFT). The corresponding power spectral density of the reference pulse is shown as inset in Fig. 2. As expected, the maximum of the power spectral density of the pulse is at the wavelet's center frequency of 55 GHz. The power spectral density decays towards the side lobes at lower frequencies. At low frequencies, the signal is distorted by the transfer function of the antennas [19] and therefore the signal to noise ratio is low for frequencies below 20 GHz. For high frequencies, the signal is limited by the bandwidth of the sampling oscilloscopes to 70 GHz. The usable frequency range for the system transfer function is therefore from 20 GHz to 70 GHz.

Within the measurement bandwidth, the transfer function $\Gamma(\omega)$ of the measured reflection is calculated by normalizing to the reflection of the shifted metal reflector. Multiple reflections at all interfaces in the setup contribute to the measured reflection transfer functions $\Gamma_{\mathrm{M}}(\omega)$. The reflection at the interface between two materials is given as:

$$\rho(\omega) = \frac{\sqrt{\varepsilon_1(\omega)} - \sqrt{\varepsilon_2(\omega)}}{\sqrt{\varepsilon_1(\omega)} + \sqrt{\varepsilon_2(\omega)}}, \tag{1}$$

where ε_1 and ε_2 describe the dielectric permittivity at the left and right side of the interface, respectively. The reflection at multiple interfaces can be expressed by the recursive expression:

$$\Gamma_i(\omega) = \frac{\rho_i - \Gamma_{i+1} T_i^2}{1 + \rho_i \Gamma_{i+1} T_i^2} \tag{2}$$

where $T_i = \exp(-j\omega\sqrt{\varepsilon_i} l_i / c)$ describes the propagation between two interfaces separated by a material of permittivity ε_i and length l_i [21]. If the complex permittivity $\varepsilon(\omega)$ and the thickness of the PMMA sample holder are known, the reflection transfer function of the MUT can be de-embedded by inverting (2). Therefore the permittivity of the PMMA holder is first extracted from the reference measurement. We assume a non-dispersive dielectric slab with constant permittivity to model the PMMA holder. The reflection transfer function of this dielectric slab can easily be modeled using (2).

To determine the unknown permittivity from the measured reflection transfer function $\Gamma_M(\omega)$, a brute force fit is used. For the modeled reflection transfer function $\Gamma_{\mathrm{model}}(\omega)$, an optimization problem of the form

$$\text{Minimize}: \quad \|\Gamma_{\mathrm{M}}(\omega) - \Gamma_{\mathrm{model}}(\omega)\| \tag{3}$$

is formulated, where $\|\cdot\|$ describes the L^2 norm. Since the solutions to this problem in general are non-unique, starting and boundary values in the vicinity of values from literature [18], [22] are chosen.

Using the obtained PMMA parameters the holder is de-embedded and an optimization problem according to (3) is formulated for the measurements of water and porcine skin as MUT. Since both MUTs are highly absorbing, reflections from the back interface of the material can be neglected. Also multiple reflections in different layers of the skin can be neglected as a first approximation. Therefore the reflection can be modeled by a single reflection at the interface by (1).

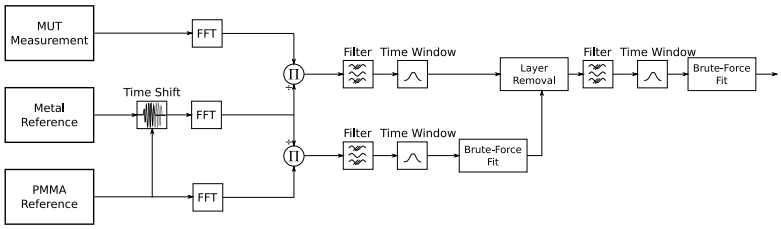

Fig. 3. Signal Processing Scheme for the frequency-domain Debye parameter estimation.

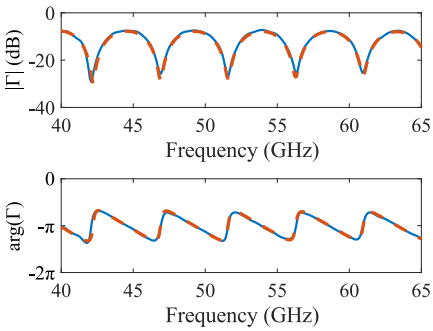

Fig. 4. Comparison of the measured reflection transfer function for PMMA (solid) with the fitted model (dashed). The permittivity is determined to $\varepsilon = 2.55 - 0.013j$.

The permittivity of skin and water is expressed by a first order Debye model:

$$\varepsilon(\omega) = \varepsilon_\infty + \frac{\varepsilon_s - \varepsilon_\infty}{1 + j\omega\tau}, \tag{4}$$

where ε_∞ describes the permittivity in the high frequency limit, ε_s is the permittivity in the static limit, and τ the relaxation constant characteristic to the material [7], [23].

B. Dielectric Permittivity Estimation and Error Analysis

Using the previously described signal processing scheme, the permittivity for the PMMA holder as well as the MUT can be estimated. The complex permittivity of the PMMA sheet was found as $\varepsilon = \varepsilon' + j\varepsilon'' = 2.55$ - 0.013j. The modeled reflection for the PMMA and the corresponding reference measurement are shown in Fig. 4. The values extracted for the PMMA are in good agreement with our previous findings in [18], [24] as well as the values measured with a Fabry-Perot interferometer in [22]. The comparison is summarized in Table I.

The permittivity of water is well studied in literature (c.f. [23], [25]–[28] among others). At frequencies below 100 GHz a single resonance Debye model has been proven to fit measured data [23], [28]. The dielectric permittivity of skin can also be described by a Debye model [29], whereas the quality of the fit depends on the layer structure of the skin

TABLE I
DIELECTRIC PERMITTIVITY OF PMMA

Method	ε'	ε''	
Brute Force Reflection	2.55	0.013	this work
Direct Time-Domain Transmission	2.532	0.009	[18]
Fabry-Perot Interferometer	2.557	0.0083	[22]

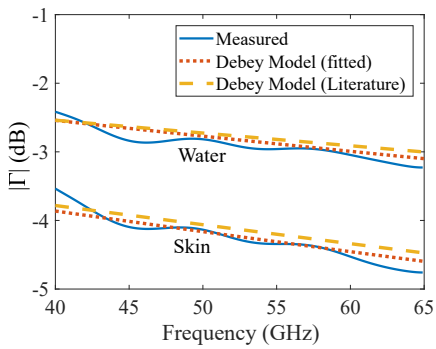

Fig. 5. Absolute of the reflection transfer function for water (top) and porcine skin (bottom). A single resonance Debye model is fitted to the responses. The fitted curves (dotted) fit well to the measured data (solid) and values for water and skin from [23] and [7], respectively (dashed).

[7]. As a first assumption, we assumed a single resonance Debye model for a homogeneous material. The comparison of the measured, de-embedded transfer function with the reflection transfer function calculated from the Debye parameters obtained from fitting and from literature are shown in Fig. 5. The fitted Debye parameters and values taken from literature are summarized in Table II. The complex permittivity of water and skin is shown in Fig. 6 (a) and (b), respectively.

For both, skin and water, the absolute of the fitted reflection transfer function is in well agreement with the values reported in literature. Within the examined frequency range, the fitted permittivity of skin and water corresponds well to the values from literature as well.

To estimate the measurement error of our system, the PMMA sheet without MUT was examined. With only air present at the back interface of the material, the reflection co-

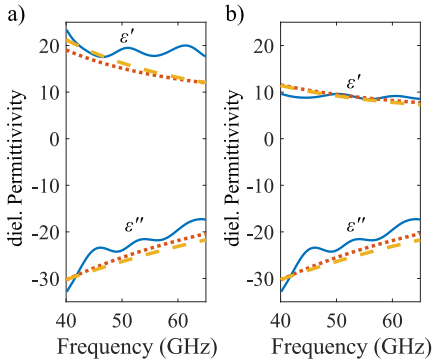

Fig. 6. Comparison of the fitted complex permittivities for water (a) and skin (b). The fitted curves (dotted) agree well with the values reported in literature (dashed) [7], [23]. For water the deviation compared to the model increases with frequency due to the influence of the LDPE bag used to contain the water.

TABLE II
SINGLE RESONANCE DEBYE PARAMETERS FOR WATER AND SKIN

Material	ε_∞	ε_s	τ (ps)	σ (S/m)	
Water	4.73	76.68	7.28	0	[23]
Water	9.92	71.88	7.28	0	this work
Skin	4	36	6.9	1.4	[7]
Skin	4.67	34.67	7.23	0.64	this work

efficient should be zero after de-embedding the PMMA sheet. Any residual reflection is caused by an error in calibration or de-embedding. Using the same de-embedding and time gating as previously, the measurement error in the reflection coefficient at the back interface can be estimated. The root-mean-square (RMS) residual error in reflection is determined as 1.27 %. This residual error in reflection propagates when calculating the dielectric permittivity. Converting the reflection coefficient to the dielectric permittivity with (1) should ideally give the permittivity of air. The RMS deviation from the expected permittivity was determined as 2.53 %. For breast tissue, the dielectric contrast between healthy tissue and tumors is larger than 12 % [9]. Therefore, the presented method should be sufficient to resolve this contrast. However, vector network analyzer based measurements using open-ended coaxial probe measurements might offer a higher accuracy [30].

This measurement error causes the Debye parameters to deviate as well. However, the fitted model and the model from literature are within the error margins. Additionally, the real permittivity of water deviates for high frequencies. This effect can also be observed in the parameter ε_∞, which represents the high frequency behavior of the permittivity. This error can be attributed to the increasing influence of the LDPE bag used to contain the water, which we considered as negligibly thin in our modeling. The estimated Debye parameters for skin, on the other hand, doesn't contain the LDPE layer and therefore doesn't show this inaccuracy in the measurement. The results are close to the values for human skin on the forearm reported in [7].

IV. TIME-DOMAIN ANALYSIS

The frequency dispersion of the material permittivity, as characterized in the previous section, leads in time domain to a distortion of the reflected pulses. In the following, this distortion is quantified in measurement and simulation. This also verifies, that essential features of the reflection are captured in the material models used.

A. Wavelet Response Simulation

To evaluate the response of a wavelet reflected on a MUT, the transfer function of the whole measurement system needs to be taken into account. A wavelet $a(t)$, incident on the MUT, is defined by a mm-wave pulse generated by the circuit, the transmitting antenna, and the propagation of the wavelet in the transmission lines and free space. The reflected wavelet is also propagated in free space and through the receiving antenna to the receiver circuit. The effects from antennas and the propagation in the receiver part can be summarized with a system transfer function $g_{\mathrm{sys}}(t)$. The wavelet response $b(t)$ for the reflection on a MUT can be expressed as:

$$b(t) = a(t) * g_{\mathrm{sys}}(t) * g_{\mathrm{MUT}}(t), \tag{5}$$

where $g_{\mathrm{MUT}}(t)$ is the reflection impulse response of the MUT.

For a metal reflector the reflection impulse response can be approximated by a Dirac delta impulse $g_{\mathrm{MUT}}(t) = -\delta(t_0)$ at t_0 as for a perfect electrical conductor. The wavelet response $b(t)$ can therefore be written as:

$$b(t) = a(t) * g_{\mathrm{sys}}(t) * -\delta(t_0) = w_{\mathrm{reflector}}(t). \tag{6}$$

The wavelet obtained from the measurement on a metal reflector can therefore be used as a template wavelet $w_{\mathrm{reflector}}(t)$. The wavelet response of a MUT is then given by $w_{\mathrm{reflector}}(t)$ convoluted with the reflection impulse response $g_{\mathrm{MUT}}(t)$. These calculations are best performed in frequency domain. The Fourier transform of (5) with the measured wavelet $w_{\mathrm{reflector}}(t)$ results in:

$$B(\omega) = W_{\mathrm{reflector}}(\omega) \cdot \Gamma_{\mathrm{MUT}}(\omega), \tag{7}$$

where $\Gamma_{\mathrm{MUT}}(\omega)$ is the reflection transfer function for the MUT and $W_{\mathrm{reflector}}(\omega)$ is the Fourier transform of the template wavelet. For the reflection responses of the measured MUTs, the PMMA sample holder needs to be taken into account. To do so, $\Gamma_{\mathrm{MUT}}(\omega)$ is replaced by the transfer function of a multilayer structure representing the structure of the sample holder and the MUT. Analogous to the calculations in Section III, the transfer function for the multilayer structure containing both sample holder and MUT is given by (2).

To simulate the wavelet responses of the measured MUTs, the transfer functions for the MUT and sample holder are calculated using the fitted permittivities from Section III. These transfer functions are then multiplied with the spectrum of the template wavelet $W_{\mathrm{reflector}}(\omega)$. The calculations are limited to the transmission band of the measurement system from 20 GHz to 70 GHz to limit noise. Since the measurement

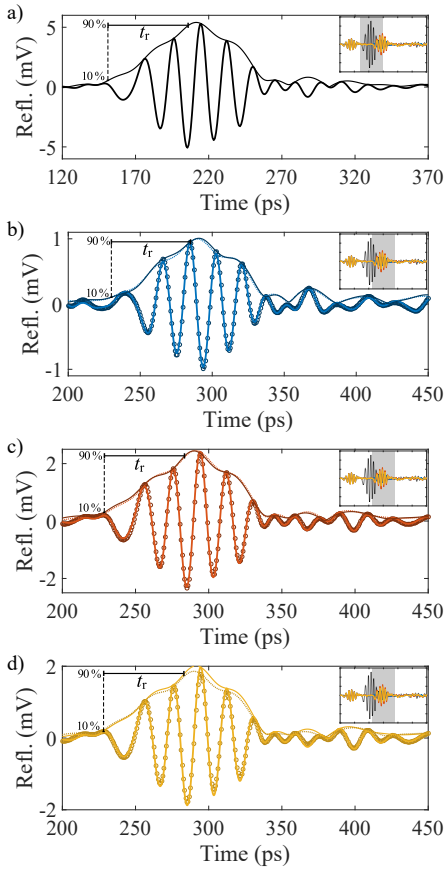

Fig. 7. Wavelet responses for the reflection on (a) a metal reflector, (b) the PMMA-air interface of the sample holder and the interface between PMMA sample holder and MUT, (c) for water and (d) skin as MUT. The metal reflector measurement in (a) is assumed as a perfect reflector and can therefore be used as reference to characterize the system impulse response. The reflection of the PMMA-MUT interface in (b), (c) and (d) compare the measured wavelet responses (dots) with the simulated wavelet responses (solid). Note the different scale on the y-axis of the plots.

of the metal reflector is aligned to the back of the sample holder, the simulated response is shifted compared to the front interface of the sample holder. This is compensated by aligning the reference plane with the front interface of the sample holder by back propagation. The time-domain wavelet responses are finally calculated by using the inverse FFT.

B. Waveform Analysis

The wavelet responses were simulated for the measurements of PMMA, water, and porcine skin as MUT, using the fitted

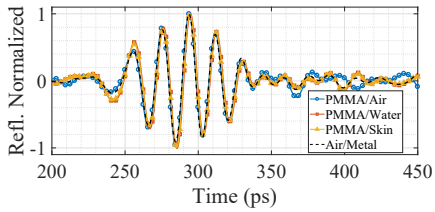

Fig. 8. Normalized wavelets measured from the MUT interface for Air (circle), Water (square) and Skin (triangle). The reflected wavelet on metal (dashed) was aligned to the same position for reference. The non-dispersive reflection on the PMMA-Air interface follows the reference reflection on the metal interface. The reflection on the dispersive material interfaces from water and skin on the other hand differ noticeable in the start-up of the wavelets.

permittivity values from Section III. The template wavelet, measured by reflection on a metal reflector, serves as a reference for the shape of the used wavelet (cf. Fig. 7 (a)). Figures 7 (b)-(d) show the measured and simulated wavelet responses of the empty sample holder, water, and porcine skin at the PMMA-MUT interface, respectively. The simulated wavelets follow the measured wavelets and the waveform is reproduced. For the wavelet reflected on porcine skin, a small difference in amplitude is visible, nevertheless the startup behavior is preserved.

Comparing the shape of the reference wavelet (metal reflection) with the wavelets reflected on a MUT, noticeable changes in amplitude and start-up phase can be observed. The wavelet reflection on the PMMA-air interface has a decreased amplitude compared to the reference wavelet, as expected. Its start-up phase is opposite to the reference wavelet since the reflection occurs on the interface of an electrically less dense medium (cf. (1) gives a negative reflection). The wavelet response on the PMMA-water and PMMA-skin interface shows a difference in amplitude as well as in the start-up behavior. However, any difference in the start-up phase is less obvious.

The reflection of a wavelet on a dispersive MUT leads to a distortion of the wavelet shape. This can be understood by the fact that the reflection transfer function of a dispersive material is decreasing in amplitude and phase towards higher frequencies (cf. Fig. 5). Therefore the dispersive reflection influences the signal amplitude and phase, since spectral components add up differently in time domain. This impacts the flanks of the pulse, analogous to the well known amplitude and group delay transformation in any causal filter. To visualize the change in the flanks, the wavelets were normalized to their maximum. The resulting normalized waveform is shown in Fig. 8. Traditionally the response of filters is characterized by the rise time from 10% to 90% of the step response of a signal [31]. To quantify the pulse distortion of the wavelets, a pulse rise time, t_r, is introduced. It is measured from 10% to 90% in relation to the maximum of the wavelet envelope. The envelope is calculated using the absolute of the analytic signal of the wavelets.

The pulse rise times of the simulated wavelets agree with the rise time of the measured wavelets (cf. Table III). For the

TABLE III
RISE TIMES OF THE WAVELET RESPONSE FOR DIFFERENT MUT

Interface	t_r (Sim.)	t_r (Measure.)
Metal	reference	52.2 ps
PMMA-air	53.0 ps	53 ps
PMMA-water	55.1 ps	55.1 ps
PMMA-skin	55.1 ps	55 ps

PMMA/air interface, the rise time is 0.8 ps longer than the rise time of the reference. The reflection on the dispersive materials (water and skin), on the other hand, causes a lager increase in rise time of about 2.8 ps compared to the reference. This change in rise time can be attributed to the distortion of the wavelets and in particular their envelope when reflected on a dispersive material. The wavelet envelope and the pulse-rise time can therefore be identified as a feature of the shape of the wavelet and be used to recognize a dispersive reflection. Together with other features like amplitude and possible chirping, a direct classification of dispersive materials in time domain should be possible.

V. CONCLUSION

A rigid characterization setup for measuring the reflection of planar materials was developed. Coherent time-domain pulses (wavelets) were emitted using an in-house wavelet generator in combination with a wideband antenna. The reflection of these wavelets on water and porcine skin as dispersive materials under test (MUT) was recorded.

From the obtained measurement data, the reflection transfer function of the MUTs was calculated in frequency domain using reference measurements on a metal reflector and the empty holder structure. A single resonance Debye model was fitted to the reflection transfer function using a brute-force optimization approach. The fitted Debye parameters for porcine skin agree well with the model for human skin reported in [7]. For low frequencies, the transfer function of water agrees well with the model from [23] as well. For high frequencies, however, the measurement deviates from the model due to the influence of a LDPE bag used to contain the water.

Time-domain wavelet responses were simulated and compared to measured reflections. The simulated time-domain responses correspond well to the measured wavelet responses and confirm the permittivity values obtained by frequency-domain fitting. However, a minor discrepancy is observed for the simulated skin response. This is most likely related to the neglected layer structure of the skin, and requires further studies. The pulses are distorted upon reflection depending on the reflection transfer function of the MUT. Changes in pulse amplitude and start-up phase are observed. Material dispersion leads to a change in pulse envelope and in rise time for the measured wavelets and therefore enables the identification of a dispersive reflection.

REFERENCES

[1] R. J. Fontana, "Recent system applications of short-pulse ultra-wideband (UWB) technology," *IEEE Trans. Microw. Theory Tech.*, vol. 52, no. 9, pp. 2087–2104, Sept 2004.

[2] F. Topfer and J. Oberhammer, "Millimeter-wave tissue diagnosis: The most promising fields for medical applications," *IEEE Microw. Mag.*, vol. 16, no. 4, pp. 97–113, May 2015.

[3] E. C. Fear, X. Li, S. C. Hagness, and M. A. Stuchly, "Confocal microwave imaging for breast cancer detection: localization of tumors in three dimensions," *IEEE Trans. Biomed. Eng.*, vol. 49, no. 8, pp. 812–822, Aug 2002.

[4] W. M. Brown and L. J. Porcello, "An introduction to synthetic-aperture radar," *IEEE Spectr.*, vol. 6, no. 9, pp. 52–62, Sept 1969.

[5] M. Zhadobov, N. Chahat, R. Sauleau, C. Le Quement, and Y. Le Drean, "Millimeter-wave interactions with the human body: state of knowledge and recent advances," *Int. J. Microw. Wireless Technolog.*, vol. 3, pp. 237–247, 4 2011.

[6] R. M. Woodward *et al.*, "Terahertz pulse imaging of ex vivo basal cell carcinoma," *J. Invest. Dermatol.*, vol. 120, no. 1, pp. 72 – 78, 2003.

[7] S. Alekseev and M. Ziskin, "Human skin permittivity determined by millimeter wave reflection measurements," *Bioelectromagnetics*, vol. 28, no. 5, pp. 331–339, 2007.

[8] H. F. Cook, "The dielectric behaviour of some types of human tissues at microwave frequencies," *Br. J. Appl. Phys.*, vol. 2, no. 10, p. 295, 1951.

[9] A. Martellosio *et al.*, "Dielectric properties characterization from 0.5 to 50 GHz of breast cancer tissues," *IEEE Trans. Microw. Theory Tech.*, vol. 65, no. 3, pp. 998–1011, March 2017.

[10] A. Nicolson and G. Ross, "Measurement of the intrinsic properties of materials by time-domain techniques," *IEEE Trans. Instrum. Meas.*, vol. 19, no. 4, pp. 377–382, Nov 1970.

[11] J. Baker-Jarvis, E. J. Vanzura, and W. A. Kissick, "Improved technique for determining complex permittivity with the transmission/reflection method," *IEEE Trans. Microw. Theory Tech.*, vol. 38, no. 8, pp. 1096–1103, Aug 1990.

[12] M. Afsar, J. Birch, R. Clarke, and G. Chantry, "The measurement of the properties of materials," *Proc. IEEE*, vol. 74, no. 1, pp. 183–199, Jan 1986.

[13] P. R. Barnes and F. M. Tesche, "On the direct calculation of a transient plane wave reflected from a finitely conducting half space," *IEEE Trans. Electromagn. Compat.*, vol. 33, no. 2, pp. 90–96, May 1991.

[14] E. J. Rothwell, "Plane-wave impulse response of a debye half space," *Electromagnetics*, vol. 27, no. 4, pp. 195–206, 2007.

[15] S. Antonijevic and D. Poljak, "A novel time-domain reflection coefficient function: TM case," *IEEE Trans. Electromagn. Compat.*, vol. 55, no. 6, pp. 1147–1153, Dec 2013.

[16] G. Narimani, P. A. Martin, and D. P. Taylor, "Analysis of ultrawideband pulse distortion due to lossy dielectric walls and indoor channel models," *IEEE Trans. Antennas Propag.*, vol. 64, no. 10, pp. 4423–4433, Oct 2016.

[17] L. Ohlsson, P. Fay, and L.-E. Wernersson, "Picosecond dynamics in a millimetre-wave RTD-MOSFET wavelet generator," *Electron. Lett.*, vol. 51, no. 21, pp. 1671–1673, 2015.

[18] I. Vakili, L. Ohlsson, L.-E. Wernersson, and M. Gustafsson, "Time-domain system for millimeter-wave material characterization," *IEEE Trans. Microw. Theory Techn.*, vol. 63, no. 9, pp. 2915–2922, 2015.

[19] I. Vakili, L. Ohlsson, M. Gustafsson, and L.-E. Wernersson, "Wideband and non-dispersive wavelet transmission using leaky lens antenna," *Electron. Lett.*, vol. 49, no. 5, pp. 321–322, February 2013.

[20] D. Pozar, *Microwave Engineering*, third edition ed. Wiley, 1997.

[21] S. J. Orfanidis, *Electromagnetic waves and antennas*. Rutgers University New Brunswick, NJ, 2002.

[22] W. Culshaw and M. Anderson, "Measurement of permittivity and dielectric loss with a millimetre-wave fabry-perot interferometer," *Proc. Inst. Elect. Eng. B - Electron. Commun. Eng*, vol. 109, no. 23, pp. 820–826, 1962.

[23] U. Kaatze, "The dielectric spectrum of water in the microwave and near-millimetre wavelength region," *Chem. Phys. Lett.*, vol. 132, no. 3, pp. 291 – 293, 1986.

[24] I. Vakili, L. Ohlsson, M. Gustafsson, and L. E. Wernersson, "Time domain material characterizations using leaky lens antennas," in *31st URSI General Assembly and Sci. Symp.*, Aug 2014, pp. 1–2.

[25] E. H. Grant, T. J. Buchanan, and H. F. Cook, "Dielectric behavior of water at microwave frequencies," *J. Chem. Phys.*, vol. 26, no. 1, pp. 156–161, 1957.

[26] M. P. Cadeddu and D. D. Turner, "Evaluation of water permittivity models from ground-based observations of cold clouds at frequencies between 23 and 170 GHz," *IEEE Trans. Geosci. Remote Sens.*, vol. 49, no. 8, pp. 2999–3008, Aug 2011.
[27] T. Meissner and F. Wentz, "The complex dielectric constant of pure and sea water from microwave satellite observations," *IEEE Trans. Geosci. Remote Sens.*, vol. 42, no. 9, pp. 1836–1849, Sept 2004.
[28] H. Liebe, G. Hufford, and T. Manabe, "A model for the complex permittivity of water at frequencies below 1 THz," *Int. J. Infrared Milli. Waves*, vol. 12, no. 7, pp. 659–675, 1991.
[29] S. Gabriel, R. W. Lau, and C. Gabriel, "The dielectric properties of biological tissues: III. parametric models for the dielectric spectrum of tissues," *Phys. Med. Biol.*, vol. 41, no. 11, p. 2271, 1996.
[30] J.-H. Jung, J.-H. Cho, and S.-Y. Kim, "Accuracy enhancement of wide-band complex permittivity measured by an open-ended coaxial probe," *Meas. Sci. Technol.*, vol. 27, no. 1, p. 015011, 2016.
[31] W. C. Elmore, "The transient response of damped linear networks with particular regard to wideband amplifiers," *J. Appl. Phys.*, vol. 19, no. 1, pp. 55–63, 1948.

Sebastian Heunisch received his M.Sc. degree in electrical engineering from the Karlsruhe Institute of Technology, Karlsruhe, Germany, in 2014. He is currently with the Department for Electrical and Information Technology at Lund university, Lund, Sweden, to obtain the Ph.D. degree. He is involved in the development, fabrication and characterization of pulse-based millimeter-wave circuits and systems. His research is aimed towards novel applications of mm-wave radar sensors. Further research interest include wideband millimeter-wave circuits, electromagnetic propagation and scattering, and radar imaging.

Lars Ohlsson received the M.Sc. degree in engineering nanoscience and the Ph.D. degree in electrical engineering from Lund University, Lund, Sweden, in 2010 and 2015, respectively, where he is currently a postdoctoral fellow with the Department of Electrical and Information Technology. He studies millimeter-wave pulse generator circuits and develops technology for wideband integrated transceiver circuits. He further explores pulse-based communication, time-domain characterization, and radar imaging. His research interests include integrated antennas, pulse generator circuits, device characterization, antenna co-design, and millimeter-wave pulse-based radio systems.

Lars-Erik Wernersson received the M.S degree the Ph.D. degree in Solid State Physics at Lund University in 1993 and 1998, respectively. Since 2005 he is Professor in Nanoelectronics at Lund University, following a position at University of Notre Dame 2002/2003. His main research topics include nanowire- and tunneling- based nanoelectronic devices and circuits for low-power electronics and wireless communication. He has authored/co-authored more than 200 scientific papers. He has been awarded two individual career grants and he served as Editor for IEEE Transaction on Nanotechnology. He is coordinator for the H2020 project INSIGHT.

Paper IV

Paper IV

Published version, reproduced from:

Sebastian Heunisch, Lars Ohlsson Fhager, and Lars-Erik Wernersson, "Pulse-Distortion Analysis for Millimeter-Wave Time-Domain Material Identification," *48th European Microwave Conference (EuMC)*, Madrid, 2018, pp. 572-575..

Pulse-Distortion Analysis for Millimeter-Wave Time-Domain Material Identification

Sebastian Heunisch, Lars Ohlsson, and Lars-Erik Wernersson
Department of Electrical and Information Technology, Lund University
PO Box 118, SE-22100, Lund, Sweden
Sebastian.Heunisch@eit.lth.se

***Abstract* — The dielectric properties of biological tissues in the millimeter-wave range is mainly determined by their water content. It also has been shown, that cancer cells have a lower water content than healthy skin cells and therefore show dielectric contrast. Analyzing the frequency dependent dielectric properties might be used to identify and distinguish materials in biomedical instruments. We propose to use the distortion caused by the frequency dependent reflection coefficient at the interface of a material as a feature for identification. We present an experimental demonstration of the pulse distortion observed in measurements on water and porcine skin. We simulate the pulse distortion introduced by filters with different frequency dispersion and relate transient features to the dispersive properties of materials under test. The presented method can be used to directly identify dispersive materials in the time domain.**

***Keywords* — Biomedical Measurement, Dielectric Characterization, Electromagnetic Reflection, Pulse Measurements, Time-domain analysis, Wavelet Generator**

I. Introduction

Many technical applications use spectroscopy to distinguish and identify materials. The dielectric properties of materials are dependent on the examined spectral range. Optically transparent materials might be opaque at other frequency ranges and show strong resonant absorption of electromagnetic waves. This leads to a variety of interesting applications of microwave and millimeter-wave (mm-wave) radiation, ranging from security scanners at airports, to industrial testing.

Biological tissues show interesting properties in the microwave and mm-wave region that might open up several applications in biomedical diagnosis and imaging. Microwave tomography, for instance, has been proposed to replace mammography as standard diagnosis method for breast cancer [1]. The key feature of interest, leading to a dielectric contrast in the mm-wave range, is the water content of the tissue. It has been shown, that it is possible to distinguish cancer cells from healthy tissue due to the difference in water content [2]. For biomedical applications it is therefore important to measure the water content and distinguish tissue from materials containing less or no water.

The permittivity of water in the mm-wave range is usually modeled using a single resonance Debye model [3]. Also many organic tissues can be represented using this model [4]. Due to the high absorption of water and organic tissues at mm-wave frequencies, only the interaction of waves with the top layers of organic tissue, or even just the surface reflection can be measured. However, when measuring over a wide bandwidth, this surface reflection shows frequency dependence as well. The dispersion affects the impulse response of the reflection at the interface [5] and reflected pulses get distorted.

In this paper, we investigate the distortion of pulses reflected on dispersive materials. We present the measured reflections of short mm-wave wavelets from water and ex-vivo porcine skin and investigate the pulse distortion caused by the reflection. In particular, we simulate transfer functions with different frequency dependence and relate the transient startup of the wavelets to the frequency dispersion of the material. We propose to use the pulse startup as an identification feature of dispersive materials. The ultimate goal is to develop a method to determine the water content of tissues directly in the time domain.

II. Material Measurements

Measurements of short mm-wave wavelets reflected at the surface of porcine skin and water were recorded as described in [6]. Here, we give a brief overview of the measurements and phenomenologically show the pulse distortion caused by the dispersive reflection as a basis for the modeling of the pulse distortion, not previously described.

A. Measurement Setup

Measurements were recorded in a mm-wave reflectometry setup (cf. Fig. 1 and [6], [7]). Coherent mm-wave pulses, so called wavelets, were generated using an in-house, wavelet generator. This circuit consists of a resonant-tunneling diode (RTD) oscillator switched with an InGaAs metal-oxide-semiconductor field-effect Transistor (MOSFET) [8]. The control signal for the circuit, a 80-ps-long baseband pulse, defining the length of the mm-wave wavelet, is provided by an Agilent N4906B BERT. The oscillation frequency of the circuit, set by a parallel inductance in the circuit, was designed to be 55 GHz. Generated wavelets are transmitted and received with a pair of wideband leaky lens antennas. Those antennas show a gain of 16 dBi and very low frequency dispersion, enabling a nearly undistorted transmission of the pulse [9]. The antennas are mounted side by side, tilted 5° towards each other, focused on a 20-mm-thick PMMA sheet at a distance of 250 mm. The PMMA sheet is

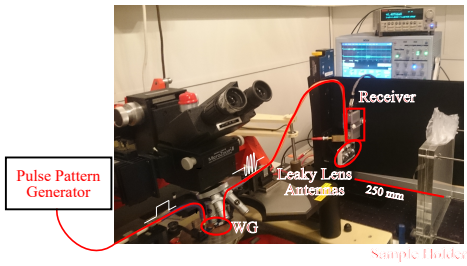

Fig. 1. Photograph of the Measurement setup. The square wave signal from a pulse pattern generator is feed to a wavelet generator circuit. The generated mm-wave signal at 55 GHz is transmitted by a leaky lens antenna and reflected at a MUT mounted in a PMMA sample holder. The reflected signal is received with a second leaky lens antenna connected to a sampling oscilloscope.

used as sample holder for a material under test (MUT). A second PMMA sheet of the same dimensions can be attached to the first PMMA sheet with screws, to clamp a MUT to the sample holder. For liquid MUTs a low-density polyethylene (LDPE) bag is used to contain the liquid. The reflection from the MUTs are recorded by a LeCroy WaveExpert 100H 70 GHz sampling oscilloscope as receiver.

B. Measurements

Measurements with different MUTs were performed. One sample of biological tissue, a fresh piece of porcine skin from the bacon rind of a pig was cut in a 20-mm-thick slice. The sample was removed from a refrigerator 30 min prior to the measurement to let the surface heat up to room temperature. The sample was clamped in between the two PMMA sheets of the sample holder and the reflection was recorded. As second material under test, deionized water was filled in a LDPE bag and also clamped in between the PMMA sheets of the sample holder. The separation of the PMMA sheets was kept at 4.8 mm using spacers. Further measurements were taken from the reflection of a single PMMA sheet, providing a measurement of the interface reflection between PMMA and air. As a reference measurement, the reflection of a flat metal reflector without the PMMA sheet was recorded.

The measured time-domain reflections from the different MUTs are shown in Fig. 2. The reflection at the front interface of the PMMA holder can be separated in time domain from the reflection at the interface of the PMMA to the MUT. While the reflection at the front interface of the PMMA holder is constant for all measurements, the reflection at the back interface changes for different MUTs. The most obvious difference between the measured reflections is the amplitude of the reflected pulse at the interface. However, looking at the reflection in frequency domain reveals that the full frequency dependent permittivity information over the measurement range can be determined. Figure 3 shows the reflection coefficients of water and skin at their interface. A clear frequency dispersion is visible over the measurement range. The measured data can be fitted to a

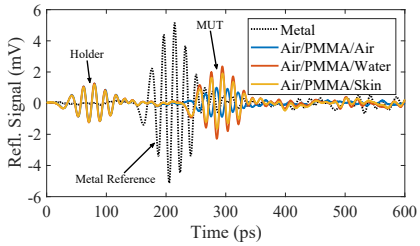

Fig. 2. Measured time-domain signal from water and porcine skin as MUT. Further, also reference measurements on an empty PMMA holder as well as a metal reflector are shown.

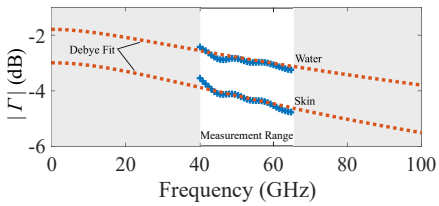

Fig. 3. Reflection coefficient for Water and Skin calculated from the measured pulse reflection. The reflection coefficient is frequency dependent, and a Debye model can be fitted to the measured data [6].

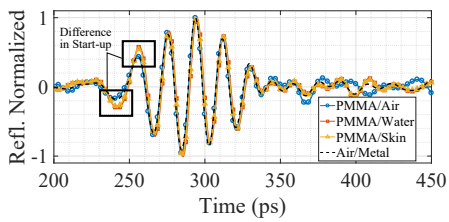

Fig. 4. Visualization of the pulse distortion caused by the reflection on an dispersive interface. A clear difference in startup is visible when comparing the dispersive reflection on water and porcine skin to the non-dispersive reflection on PMMA and Metal.

Debye model [6]. This difference between the reflections can also be visualized directly in time domain. By normalizing the pulses to their maximum, differences in the startup of the pulses can be observed (cf. Fig. 7). The dispersive reflection at the PMMA-water and PMMA-skin interface causes a stronger signal in earlier parts of the pulse, compared to the non-dispersive reflections on a PMMA-air or metal interface.

III. Simulations

The origin of the measured pulse distortions are now evaluated in more detail by simulating pulses reflected on materials with different dielectric properties.

A. Dispersive Reflection Model

Many dispersive materials, for instance water and biological tissues, can be modeled with a Debye permittivity model in the microwave and mm-wave range [3], [4]. Mathematically the dielectric permittivity of a Debye model material can be expressed by

$$\varepsilon(\omega) = \varepsilon_\infty + \frac{\varepsilon_s - \varepsilon_\infty}{1 + j\omega\tau}, \tag{1}$$

where ε_∞ and ε_s is the permittivity in the high frequency and low frequency limit, respectively, τ is the relaxation time, and $\omega = 2\pi f$ the angular frequency.

The reflection of a wave at the interface between two materials with the dielectric permittivities ε_1 and ε_2 is given by

$$\Gamma(\omega) = \frac{\sqrt{\varepsilon_1(\omega)} - \sqrt{\varepsilon_2(\omega)}}{\sqrt{\varepsilon_1(\omega)} + \sqrt{\varepsilon_2(\omega)}}. \tag{2}$$

The reflection at the interface of dispersive materials can therefore simply be obtained, by inserting the frequency dependent dielectric permittivity in (2).

Figure 5 shows the frequency dependent reflection coefficient on the particular case of an air-water-interface. ($\varepsilon_{inf} = 4.73$, $\varepsilon_s = 76.68$, $\tau = 7.28$ ps, [3]). The absolute value of the reflection coefficient decreases with increasing frequency. At 60 GHz the slope of the decay is approximately 0.019 dB/GHz. For a Debye model material, the reflection coefficient is a nonlinear function due to the square-roots in (2). However, in virtually any technical application the measurement bandwidth is limited, which justifies a simplification of the reflection coefficient. We therefore propose to approximate the dispersive reflection coefficient by a simple low pass filter transfer function

$$\Gamma(\omega) = \frac{K}{(1 + j\omega\tau)^n} \tag{3}$$

having a similar slope and amplitude in the frequency range of interest. Note, that the approximation using this simple filter function comes at the cost of a different group delay behavior (cf. Fig 5b). The simple low pass filter model overestimates the group delay difference and can therefore not be used in cases where the exact delay of the pulse response should be evaluated.

B. Pulse Simulation

To characterize the distortion of the pulses, the dispersive reflection coefficient (cf. Fig. 5) is approximated by simple low pass filters according to (3). Parameters for the transfer function of the filters were chosen to have different slopes (order n of the filters). The filter transfer functions were multiplied by a constant factor K, to keep the transfer function equal to unity for the pulse center frequency. The examined filters are shown in Fig. 6.

To simulate pulses resembling the pulses reflected on a dispersive interface, the system transfer function $T_{\text{sys}}(\omega)$ and the incident pulse shape $W_{\text{inc}}(\omega)$ needs to be known. The

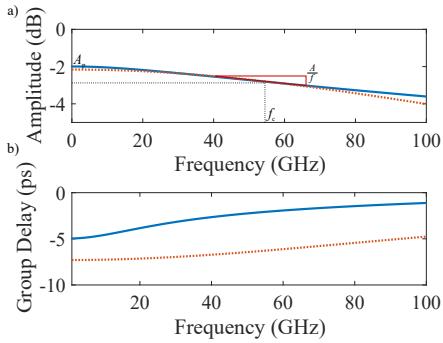

Fig. 5. The (a) Amplitude and (b) Group Delay of the reflection coefficient of a Debye material interface (Water $\varepsilon_{inf} = 4.73$, $\varepsilon_s = 76.68$, $\tau = 7.28$ ps, [3]). The approximation with a first order low pass filter approximates the amplitude behavior of the reflection coefficient. The group delay, however is overestimated.

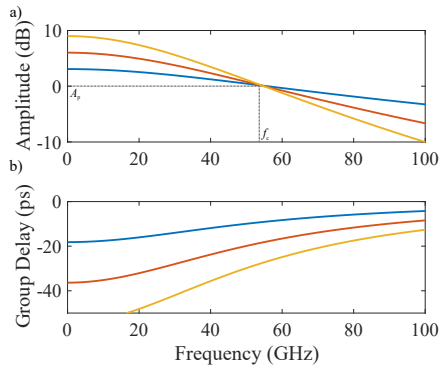

Fig. 6. Simple filters to simulate a frequency dependent reflection coefficient. For the simulation the relaxation time τ is kept at $1/55GHz$ while the order of the filter and therefore the frequency dependent slope is varied between 1 and 3. The factor K is varied to achieve a constant amplitude for the pulse center frequency. The filters therefore enhance the lower order side lobes of a pulse.

reflection at the material interface in frequency domain is given by

$$R(\omega) = W_{\text{inc}}(\omega) \cdot T_{\text{sys}}(\omega) \cdot \Gamma_{\text{MUT}}(\omega). \tag{4}$$

Therefore, for a MUT with known reflection coefficient $\Gamma_{\text{MUT}}(\omega)$, the system transfer and pulse shape $T_{\text{sys}}(\omega)$ and $W_{\text{inc}}(\omega)$ can be obtained from a reference measurement. For our simulations, we used the Fourier transform of the pulse reflection from a flat metal surface with $\Gamma_{\text{MUT}}(\omega) = -1$ assuming a perfect conducting material. For the linear system, the response for any material under test, can then be calculated by simply multiplying the reflection coefficient with $W_{\text{inc}}(\omega) \cdot T_{\text{sys}}(\omega)$ obtained from the reference measurement. The simulated pulse reflection $R(\omega)$ can be then be obtained

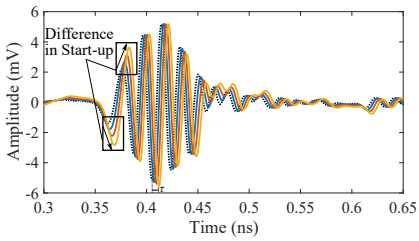

Fig. 7. Pulse Distortion for the simulated filers. The pulse startup is influenced by the slope of the filters and early parts of the pulse are enhanced for steeper frequency dependence.

by transforming to a pulse response in time domain using a Fourier transform.

The pulse responses for simulated filters are shown in Fig. 7. The delay between the pulses due to different group delays is overestimated in the simplified model, as discussed earlier. In the measured data no significant delay is observed, so the delay in the simulation should be disregarded. For the amplitude behavior of the simulations, however, it can be seen that the startup of the pulse is dependent on the slope of the filter functions. The steeper the slope of the reflection coefficient in the frequency domain, the faster the pulses start, and the stronger the first peaks in the pulse. This behavior is corresponding to the distortion observed for the reflection on the dispersive materials water and porcine skin (cf. Fig. 4). Due to the slope of the frequency dependent reflection, the startup of the pulse is enhanced in the same way in the experimental data.

IV. Conclusion

Pulse distortion for the reflection from dispersive materials is related to the frequency dependent reflection coefficient. We measured this pulse distortion experimentally for measurements at the interface between PMMA and water, as well as PMMA and porcine skin, respectively. The distortion is mainly manifested in a difference in the startup of the pulse. Our simulations show, that a steeper frequency dispersion causes a steeper transient startup of the received wavelets. The results will be useful for identifying dispersive materials and distinguishing them from non-dispersive materials directly in time domain.

Acknowledgment

This work was supported in part by the Swedish Foundation for Strategic Research (SSF), in part by the Swedish Research Council (VR), and in part by the Knut and Alice Wallenberg Foundation.

References

[1] E. C. Fear, X. Li, S. C. Hagness, and M. A. Stuchly, "Confocal microwave imaging for breast cancer detection: localization of tumors in three dimensions," *IEEE Trans. Biomed. Eng.*, vol. 49, no. 8, pp. 812–822, Aug 2002.

[2] R. M. Woodward, V. P. Wallace, R. J. Pye, B. E. Cole, D. D. Arnone, E. H. Linfield, and M. Pepper, "Terahertz pulse imaging of ex vivo basal cell carcinoma," *J. Invest. Dermatol.*, vol. 120, no. 1, pp. 72 – 78, 2003.

[3] U. Kaatze, "The dielectric spectrum of water in the microwave and near-millimetre wavelength region," *Chem. Phys. Lett.*, vol. 132, no. 3, pp. 291 – 293, 1986.

[4] S. Gabriel, R. W. Lau, and C. Gabriel, "The dielectric properties of biological tissues: III. parametric models for the dielectric spectrum of tissues," *Phys. Med. Biol.*, vol. 41, no. 11, p. 2271, 1996.

[5] E. J. Rothwell, "Plane-wave impulse response of a debye half space," *Electromagnetics*, vol. 27, no. 4, pp. 195–206, 2007.

[6] S. Heunisch, L. Ohlsson, and L.-E. Wernersson, "Reflection of coherent millimeter-wave wavelets on dispersive materials: A study on porcine skin," *IEEE Trans. Microw. Theory Techn.*, accepted, 2018.

[7] I. Vakili, L. Ohlsson, L.-E. Wernersson, and M. Gustafsson, "Time-domain system for millimeter-wave material characterization," *IEEE Trans. Microw. Theory Techn.*, vol. 63, no. 9, pp. 2915–2922, 2015.

[8] L. Ohlsson, P. Fay, and L.-E. Wernersson, "Picosecond dynamics in a millimetre-wave RTD-MOSFET wavelet generator," *Electron. Lett.*, vol. 51, no. 21, pp. 1671–1673, 2015.

[9] I. Vakili, L. Ohlsson, M. Gustafsson, and L.-E. Wernersson, "Wideband and non-dispersive wavelet transmission using leaky lens antenna," *Electron. Lett.*, vol. 49, no. 5, pp. 321–322, February 2013.

Paper V

Paper V

Peer-reviewed version, reproduced from:

Sebastian Heunisch, Lars Ohlsson Fhager, and Lars-Erik Wernersson, "Millimeter-Wave Pulse Radar Scattering Measurements on the Human Hand," *IEEE Antennas and Wireless Propagation Letters*, vol. 18, no. 7, pp. 1377-1380, 2019..

Millimeter-Wave Pulse Radar Scattering Measurements on the Human Hand

S. Heunisch, L. Ohlsson Fhager and L.-E. Wernersson

***Abstract*—We investigate the backscattering of low-power millimeter-wave pulses (wavelets) on the human hand in order to determine the detection limit of scattering features. Using an in-house wavelet radar setup with a nominal spatial resolution of 2.29 cm, we measure a hand in three different postures, a flat hand, a fist and a hand with raised index finger. For the later, we are able to resolve backscattering from at least two different scattering centers, attributed to the heel of the hand and the finger. The effective radar cross-section (RCS) in the measurements was in the range from -29.5 to -35.1 dBsm. We demonstrate that detecting scattering features from the hand with an equivalent isotropically radiated power spectral density of -68.5 dBm/MHz is possible. This shows that, compared to most conventional radar systems operating close to the regulatory emission limits (13 dBm/MHz), the energy of the transmitted waveform can be significantly reduced. The result shows that low-power radar systems for gesture recognition are feasible using pulsed systems with ultra-short pulses and low duty cycles. This is key for integration in battery powered devices.**

***Index Terms*—Gesture Recognition, Millimeter-waves, Millimeter-wave Radar, Radar Applications, Radar Cross-Section Measurement, Pulsed Radar, Time-Domain Analysis**

I. Introduction

Advances in high-frequency integrated circuit technology make radar systems available for consumer applications beyond conventional motion sensors. Integration to a small form factor is important and therefore frequency bands at mm-wave frequencies, in particular the band around 60 GHz with a large available bandwidth [1], are of particular interest. Today, even battery-powered radar systems for short ranges are feasible. This opens up a variety of novel applications, for instance gesture control in handheld and wearable devices.

Recently, several radar systems for gesture recognition have been proposed. Some approaches rely only on the Doppler profile of hand gestures [2], [3]. Other approaches additionally resolve gestures spatially [4]–[8], providing additional information for gesture recognition. Most systems use frequency modulated continuous wave (FMCW) radar, due to simplified transceiver design and high output power. For designing energy efficient radars for battery-powered applications, duty cycling the system is key. Time-domain pulse generation techniques [9], [10], offer a direct way to realize those duty cycles in integrated implementations. Ideally, continuously running oscillators at the mm-wave frequency can be avoided by this approach. In a pulsed system, the signal-to-noise ratio (SNR) is limited by the pulse energy, proportional to the amplitude and length of the transmitted pulses, and the wide bandwidth of the receiver. For low-power operation, the energy of the transmitted signal should be minimal, while still assuring that individual scattering centers on the hand can be detected. This can be solved by modulating the pulse in amplitude, frequency or phase, to increase the time-bandwidth product of the waveform.

In this paper, we use an in-house fabricated pulse generator [11] to investigate the scattering of mm-wave pulses (wavelets) on the human hand. We present measurements of the reflection from the human hand in three different postures, a flat hand (Posture A), a fist (Posture B), and a hand with raised index finger (Posture C). We show that a signal can be acquired with pulsed waveforms much weaker than the allowed emission limits in the 60 GHz band [1], which is commonly used as signal level for conventional radar systems. To the best of the authors' knowledge, this is the first measurement of ultra-short mm-wave pulses scattered on a human hand. High spatial resolution in our measurements enables the identification of features of the postures that are separated in down-range. To quantify the backscattered signal form these features, we calculate their frequency averaged radar cross-section (RCS). Our results show that compared to previously presented gesture recognition systems, the transmitted energy can be reduced, while scattering feature detection is still possible. From that, we conclude that the design of battery-powered radar systems for the recognition of dynamic hand-gestures is possible.

II. Measurement System

The reflection of static hand gestures was measured with a time-domain wavelet radar setup. A block-level schematic of the measurement setup is shown in Fig. 1. Coherent mm-wave pulses (wavelets) in the 60 GHz band were generated with an in-house RTD-MOSFET wavelet generator. The pulse pattern of the generated wavelets is controllable by a digital input sequence, achieving a pulse length down to 25 ps [11]. In our measurements, a 10 Gbps input sequence was provided by an Agilent N4906B BERT, resulting in a pulse length of 100 ps. The used wavelet generator had an oscillation

Manuscript received XXX, 201X; accepted XXX XX, 201X. Date of publication XX XX, 201X; date of current version XXX XX, 20XX. This work was supported in part by the Swedish Foundation for Strategic Research (SSF), in part by the Swedish Research Council (VR), and in part by the Knut and Alice Wallenberg Foundation.

The authors are with the Department of Electrical and Information Technology, Lund University, 221 00 Lund, Sweden (e-mail: sebastian.heunisch@eit.lth.se; lars.ohlsson_fhager@eit.lth.se; lars-erik.wernersson@eit.lth.se).

Color versions of one or more of the figures in this letter are available online at http://ieeexplore.ieee.org.

Digital Object Identifier 10.1109/LAWP.20XX.XXXXXXXX

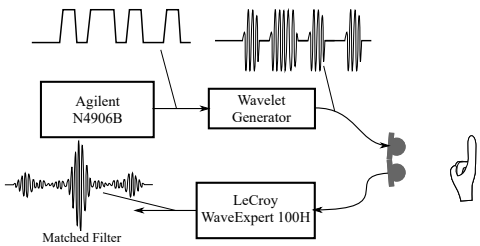

Fig. 1. Schematic of the measurement setup. A square wave signal from an Agilent N4906B BERT is fed to an in-house wavelet generator to generate a staggered pulse sequence. The received signal is recorded using a LeCroy WaveExpert 100H equivalent-time sampling oscilloscope and the matched filter response is calculated by the correlation of the received signal with a template.

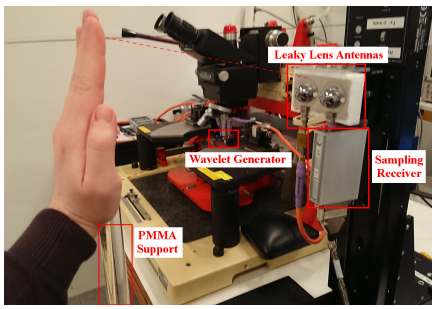

Fig. 2. Photograph of the measurement setup. The signal is generated by an in-house wavelet generator. The pair of wideband leaky-lens antennas are for transmitting and receiving. Reflection form hand postures at 250 mm distance from the antennas are recorded. The PMMA rod, located outside the main lobe of the antennas, is used to support the hand during gesture measurements.

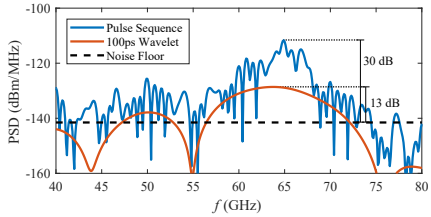

Fig. 3. Power spectral density (PSD) of waveforms backscattered on a metal reflector at 250 mm distance. The waveforms were acquired by averaging over 1000 measurements ($A = 1000$). The staggered pulse sequence (blue) gives a 17 dB higher PSD compared to a 100 ps wavelet (red). The noise floor for the acquisition settings used for the hand measurements ($A = 10$) is shown dashed.

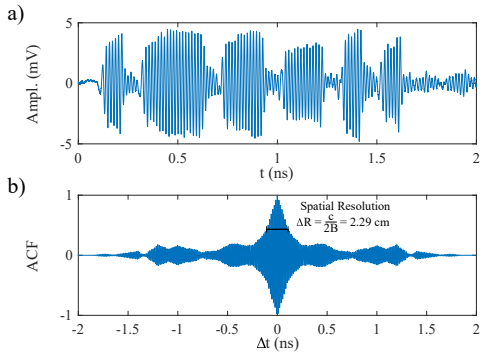

Fig. 4. a) Staggered pulse sequence and b) its autocorrelation function (ACF) showing the matched filter response of the transmitted sequence.

frequency of 65 GHz. A pair of non-dispersive wideband leaky lens antennas with approximately 16 dBi [12] was used for transmitting and receiving wavelets. The received signal was acquired directly using a LeCroy WaveExpert 100H sampling oscilloscope with a nominal bandwidth of 70 GHz. Hand postures were measured at 250 mm distance from the antennas. An acrylic glass (PMMA) rod was used as support for the hand to avoid unintentional movement as far as possible (cf. photograph of the setup in Fig. 2). Data of three hand postures (flat hand, fist, and the hand with raised index finger) was acquired in 1000 consecutive measurements. As reference, the reflection of a 300x300 mm^2 metal plate was recorded. Additional details about the setup, also used for material characterization, are available in [13].

III. Signal Acquisition

Decreasing the energy of the transmitted waveform, is one way to reduce the power consumption of a radar system. However, the received energy needs to be sufficient to distinguish the signal from the receiver noise. Limited peak power in pulsed radar systems requires the longer waveforms to carry sufficient energy. To realize high-resolution waveforms, the signal is typically modulated in amplitude, frequency or phase. Controlling the length of the waveform allows to adapt the transmitted energy to the application specific needs. In this section we investigate the detection limit for reflections from the human hand and the requirements for the measurement system.

To evaluate the link budget of our measurements, we analyze the power spectral density (PSD) backscattered on the reference metal plate. Measurements of the PSD for a signal reflected on a metal reflector in 250 mm distance are shown in Fig. 3. For a 100 ps wavelet the PSD is less than -128.6 dBm/MHz. Naturally, a longer wavelet would result in a signal with higher PSD but lower bandwidth, and therefore lower spatial resolution. For our measurements we used a pulse sequence [14] to increase the transmitted energy without significant loss of resolution. The used sequence and its autocorrelation function (ACF) are shown in Fig. 4a) and b), respectively. The nominal resolution for the waveform is $\Delta R = 2.29$ cm. The measured maximum PSD for the pulse sequence is -111.7 dBm/MHz. In our setup, this corresponds

to an equivalent isotropically radiated PSD (EIRP SD) of -68.5 dBm/MHz. The used PSD is much lower than in most other mm-wave radar systems. Typically, radar sensors are operated close to the allowed transmission limits. In the draft of the European regulations [1], the maximum PSD is 13 dBm/MHz in the 60 GHz band and -20 dBm/MHz for the out-of-band emissions. In the following, we will show, that identifying scattering features of the human hand is possible with a signal with low PSD, as used in our system.

The level of the backscattered signal is dependent on the RCS of the object under test. The RCS, σ_{Hand}, of the human hand has been reported to be in the range of -45 dBsm$< \sigma_{\mathrm{Hand}} < -20$ dBsm [15]. To estimate the expected backscattered power from the posture we compare σ_{Hand} to the RCS of our metal reflector, σ_{Ref}. Since the metal plate used is large compared to the wavelength and the illuminated area, we approximate the reflector as perfect mirror. Its RCS at distance $R = 250$ mm is given by $\sigma_{\mathrm{Ref}} = \pi R^2 \approx -7$ dBsm. The expected power level from the hand postures is therefore -13 to -38 dB lower than the reflection of the reference reflector.

For measurements with the sampling oscilloscope, fast acquisition and low noise floor need to be traded off. Waveforms are obtained by multiple sampling in different periods of the signal at interleaved sampling steps. Incoherence due to movement during the acquisition interval distorts the signal and prevents detection. The noise floor also depends on the acquisition speed. Our sampling oscilloscope has an input impedance of 50 Ω and a noise level of approximately $V_{RMS} = 3$ mV. This translates to a noise PSD of

$$S_{xx} = \frac{\Delta t}{A} \cdot \frac{V_{RMS}^2}{50\,\Omega}, \tag{1}$$

where Δt is the sampling step and A is the number of averages taken during acquisition. Empirically we achieved good results with an effective sampling step $\Delta t = 0.39$ ps and $A = 10$. This results in a noise floor of -141.5 dBm/MHz. For the used waveforms this gives us about 30 dB dynamic range (cf. Fig. 3). This shows, that features 30 dB weaker than the reference can be detected, i.e. features down to a RCS of -37 dBsm. The effective acquisition rate in these measurements, limited by the processing speed of the sampling oscilloscope was approximately 10 Hz. Our calculations show, that low energy pulsed waveforms with low duty cycles can be used to detect scattering from the human hand. This is a key factor for the development of battery powered gesture recognition systems.

IV. Measurement Results and Discussion

The measured hand postures (flat hand, posture A, fist, posture B, and hand with raised index finger, posture C), and the corresponding backscattered signals are shown in Fig. 5. Spatially resolved features for the postures are determined from the measurements.

Posture A shows one feature at the position of the hand. The distorted shape of the matched filter response (compare to the ACF in Fig. 4b) might indicate reflections from multiple scattering centers, which can't be resolved by the used waveform. Similarly, the reflection from posture B shows only one single feature. Posture C, by contrast, shows two clear features separated by approximately 25 mm. We attribute these two features to the reflections of the long side of the finger and the heel of the hand facing the antenna, respectively.

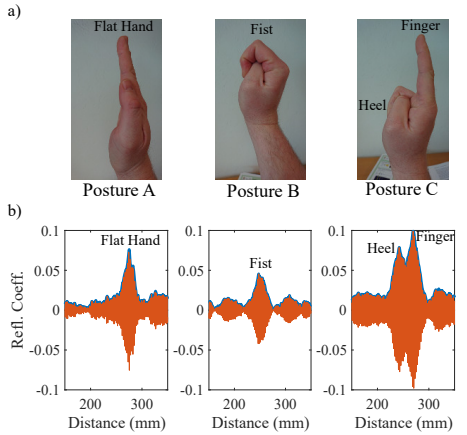

Fig. 5. a) Radar reflection of different static hand postures: flat hand (Posture A), fist (Posture B) and hand with raised index finger (Posture C). b) Range dependent reflection coefficient for the measured postures. In posture C reflections from the heel and the index finger can be resolved.

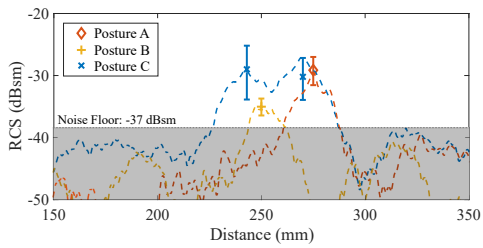

Fig. 6. RCS of the hand in the measured postures. Mean values and confidence interval for 1000 measurements are shown. The flat hand (Posture A) has a mean RCS of -29.8 dBsm. The fist's (Posture B) mean RCS is -35.1 dBsm. For Posture C the heel of the hand has a mean RCS of -29.5 dBsm and the index finger -30.6 dBsm.

To quantify the amplitude of the measured reflection, we estimate the frequency averaged RCS [16] of the postures in the measured position. The RCS is estimated in reference to the reflection obtained by the measurement of the metal plate ($\sigma_{\mathrm{Ref}} = -7$ dBsm). The RCS for the three postures in the measured position, including mean and confidence interval for all 1000 measurements, are shown in Fig. 6. In general, we expect the RCS of the postures to be strongly dependent on the exact positioning and incidence angle. For our measurements we determine a mean RCS of -29.8 dBsm for posture A.

Posture B shows the lowest RCS with -35.1 dBsm. For posture C, the variance of the peak RCS is highest, indicating a strong influence of the positioning of the hand. In this posture we determine the RCS of the heel as -29.5 dBsm and the RCS of the finger as -30.6 dBsm. The values are in the range of previously reported hand RCS values in E-Band (60-90 GHz) [15].

V. Conclusion

We have measured the scattering of mm-wave radar pulses on the human hand using an in-house mm-wave radar system. Three different hand postures, the flat hand, the fist and the hand with raised index finger were investigated. We show detection of scattering features with an EIRP spectral density of -68.5 dBm/MHz. This is much lower than the regulatory emission limits, at which most conventional radar systems operate. We conclude that the power consumption of radar-based gesture recognition systems can be reduced by using ultra-short pulsed signals with low duty cycles. Further, the high spatial resolution of our pulsed waveform enables identifying characteristic features in the acquired matched filter response of the postures, for instance the time-delay between the finger and the heel of the hand. The RCS of the features, found in the measured postures, was in the range of -29.5 to -35.1 dBsm. Our result demonstrates the feasibility of the detection of the human hand using a pulsed mm-wave radar systems and is relevant for the design of a low-power gesture recognition system. In future work, we plan to use a real-time receiver in our system. By applying pulse-Doppler processing we will be able to acquire down-range and velocity information simultaneously. This will enable gesture recognition and classification.

References

[1] "Short range devices (SRD) - Radio equipment to be used in the 40 GHz to 246 GHz frequency range," European Telecommunications Standards Institute (ETSI), Harmonised European Standard EN 305 550, Oct. 2017, Draft.

[2] Y. Kim and B. Toomajian, "Hand gesture recognition using micro-doppler signatures with convolutional neural network," *IEEE Access*, vol. 4, pp. 7125–7130, 2016.

[3] T. Sakamoto, X. Gao, E. Yavari, A. Rahman, O. Boric-Lubecke, and V. M. Lubecke, "Hand gesture recognition using a radar echo IQ plot and a convolutional neural network," *IEEE Sensors Lett.*, vol. 2, no. 3, pp. 1–4, Sept 2018.

[4] J. Lien, N. Gillian, M. E. Karagozler, P. Amihood, C. Schwesig, E. Olson, H. Raja, and I. Poupyrev, "Soli: Ubiquitous gesture sensing with millimeter wave radar," *ACM Trans. Graph.*, vol. 35, no. 4, pp. 142:1–142:19, Jul. 2016.

[5] Z. Zhang, Z. Tian, and M. Zhou, "Latern: Dynamic continuous hand gesture recognition using FMCW radar sensor," *IEEE Sensors Journal*, vol. 18, no. 8, pp. 3278–3289, April 2018.

[6] S. Ryu, J. Suh, S. Baek, S. Hong, and J. Kim, "Feature-based hand gesture recognition using an FMCW radar and its temporal feature analysis," *IEEE Sensors Journal*, vol. 18, no. 18, pp. 7593–7602, Sept 2018.

[7] Y. Sun, T. Fei, F. Schliep, and N. Pohl, "Gesture classification with handcrafted micro-doppler features using a FMCW radar," in *2018 IEEE MTT-S Int. Conf. on Microw. for Intelligent Mobility (ICMIM)*, April 2018, pp. 1–4.

[8] F. Khan, S. K. Leem, and S. H. Cho, "Hand-based gesture recognition for vehicular applications using IR-UWB radar." *Sensors*, vol. 17, Apr 2017.

[9] N. Deparis, A. Siligaris, P. Vincent, and N. Rolland, "A 2 pj/bit pulsed ILO UWB transmitter at 60 GHz in 65-nm CMOS-SOI," in *IEEE Int. Conf. on Ultra-Wideband (ICUWB) 2009*, Sept 2009, pp. 113–117.

[10] M. Egard, M. Arlelid, L. Ohlsson, B. Borg, E. Lind, and L. E. Wernersson, "$In_{0.53}Ga_{0.47}As$ RTD-MOSFET millimeter-wave wavelet generator," *IEEE Electron Device Lett.*, vol. 33, no. 7, pp. 970–972, July 2012.

[11] L. Ohlsson, P. Fay, and L.-E. Wernersson, "Picosecond dynamics in a millimetre-wave RTD-MOSFET wavelet generator," *Electron. Lett.*, vol. 51, no. 21, pp. 1671–1673, 2015.

[12] I. Vakili, L. Ohlsson, M. Gustafsson, and L.-E. Wernersson, "Wideband and non-dispersive wavelet transmission using leaky lens antenna," *Electron. Lett.*, vol. 49, no. 5, pp. 321–322, February 2013.

[13] S. Heunisch, L. Ohlsson, and L. E. Wernersson, "Reflection of coherent millimeter-wave wavelets on dispersive materials: A study on porcine skin," *IEEE Trans. Microw. Theory and Techn.*, vol. 66, no. 4, pp. 2047–2054, 2018.

[14] C. Kaiteris and W. L. Rubin, "Pulse trains with low residue ambiguity surfaces that minimize overlapping target echo suppression in limiting receivers," *Proc. of the IEEE*, vol. 54, no. 3, pp. 438–439, March 1966.

[15] P. Hügler, M. Geiger, and C. Waldschmidt, "RCS measurements of a human hand for radar-based gesture recognition at E-band," in *2016 German Microw. Conf. (GeMiC)*, March 2016, pp. 259–262.

[16] L. Li, A. E. C. Tan, K. Jhamb, and K. Rambabu, "Characteristics of ultra-wideband pulse scattered from metal planar objects," *IEEE Trans. Antennas Propag.*, vol. 61, no. 6, pp. 3197–3206, June 2013.

Paper VI

Paper VI

Pre-peer-reviewed version, reproduced in printed version only, submitted as:

Lars Ohlsson Fhager, Sebastian Heunisch, Anton Evertsson, Hannes Dahlberg, and Lars-Erik Wernersson, "Pulsed Millimeter Wave Radar for Hand Gesture Sensing and Classification," *IEEE Sensors Letters*, submitted: July 2019.